MASTER

PRINCETON UNIVERSITY

DISCLAIMER

COO-3072-89

Princeton University
Elementary Particles Laboratory
Department of Physics

SEARCH FOR CHARM IN PION AND ANTI-PROTON INTERACTIONS NEAR THRESHOLD

Richard W. Kadel

August 1977

Contract EY-76-C-02-3072

TABLE OF CONTENTS

ABSTRACT

We report here a search for charmed particles produced by antiprotons of momentum 15.0, 12.4, and 8.5 GeV/c and pions of momentum 15.0 and 10.5 GeV/c. Charged particles emerging from a carbon target near 90^0 in the center of mass (18^0 lab) were detected in a double arm spectrometer with a low momentum cutoff of $P_{lab} \gtrsim 1$ GeV/c. Our best upper limit the process $\overline{P}N \to D^0 (\overline{D}^0) + X$, where the D^0 $(\overline{D}^0)$ decays into $K^- - \pi^+$ $(K^+ - \pi^-)$, is:

$$\sigma B = 780 \pm 300 \text{ nb},$$

at a beam momentum of 8.5 GeV/c.

For the 10.5 GeV/c pion running the trigger was restricted by requiring the presence of a slow forward pion in a third spectrometer area, in coincidence with the usual double arm trigger. The acceptance of the third arm was chosen to include pions from the decay of the charmed D^{*-} meson, which has a very small Q value. Our upper limit for the process:

$$\begin{array}{l} \pi^- \; N \to D^{*-} + X \\ \qquad\quad \lfloor\!\to \pi^- + \overline{D}^0 \\ \qquad\qquad\qquad \lfloor\!\to K^+ + \pi^- \end{array}$$

is $\sigma\, B = 16 \pm 16$ nb.

Additionally, we report a measurement of inclusive K* (1421) production in anti-proton interactions at 8.5 GeV/c. The cross-section times branching ratio is:

$$\sigma\,(\overline{P}N \to K^* \,(1421) + X) * B_{K^* \to K\pi} = 4. \pm .8 \times 10^{-29} \text{ cm}^2 \quad .$$

ACKNOWLEDGEMENTS

The research reported here would not have been possible without the extended commitment of several individuals. The group was led by Dr. Val Fitch. There was little in the experiment which was not influenced by his guidance. The intellectual environment he created was a stimulus to his students and co-workers. When answers were not obvious, he knew what questions to ask. Dr. Rossanna Regge had primary responsibility for the design of the beam line and Monte Carlo simulations of the apparatus. Additionally, she was responsible for the construction of the water Cherenkov counter. Dr. Michael Witherell performed a large fraction of the analysis. The insight he provided permitted me to avoid many pitfalls. Responsibility for the coordination of the activities of the shops and support personnel was accepted by Dr. Robert Webb. His unflagging sense of humor helped to deflate many a tense moment. Dr. Morgan May had the difficult task of liasion between the Princeton Group and the AGS personnel. My fellow graduate student, John Whittaker, deserves special mention. His careful attention to detail saved the experiment more than once from disaster.

Throughout the two years during which the data was collected, there were many individuals without whose contribution the experiment could not have progressed. Victor Bearg is to be commended for writing the on-line program as well as the initial draft of the track reconstruction routine. Marius Isaila and Ann David designed and built the timing and readout electronics for the drift chambers. In this

regard Betsy Davis and Mary Bowlby were also of assistance. Carl Bopp designed the computer interface to the experimental equipment.

All of the major pieces of equipment were constructed in the Elementary Particles Laboratory of Princeton University. The technicians who built the apparatus include Howard Edwards, Walt Davidson, John Quinn, Walt Bell, Frank Bozarth, Nick Diaczenko, Sam Morreale, Dick Rabbermann and Ken Wright.

Finally I would like to thank Dr. Pamela Surko, who read (and corrected) this thesis; Bobbie Cruser, who corrected my spelling and typed the manuscript; and John Gomany of the drafting department.

I. INTRODUCTION

Resurrected by Glashow, Iliopoulos and Maiani[1] as a mathematical convenience for the supression of strangeness changing neutral currents, the charmed quark remained a theoretical speculation until the discovery, in November of 1974, of the J/ψ (3095) by Ting[2] et al., at the Alternating Gradient Synchrotron (AGS) at Brookhaven National Laboratory (BNL), and Richter, et al[3]., at SPEAR.

A fourth quark was no new-comer to high energy physics theory. As earily at 1963 Maki[9] had proposed a fourth quark based on arguments about quark-lepton symmetry. Given the four leptons (ν,ν', e,μ) it was theoretically attractive to have four equally fundamental hadrons. What distinguished the work of Glashow, Iliopoulos and Maiani was their proposed scheme for coupling the neutral hadronic current to the neutral leptonic current. Their scheme not only symmetrized the weak and electromagnetic interactions of hadrons and leptons, but did so without violating any of the empirical rules of the weak interaction.

The J/ψ and its radial excitations, ψ' (3700), ψ'' (4100), etc; betray no visible charm - according to the theory they are bound states of a charmed quark and an anti-charmed quark. Confirmation of the theory required the discovery of new particles with naked charm. **Several** experiments, of which the present work is a part, were initiated to search for charmed particles. A number of events with the characteristics of charm production were seen. But totally convincing evidence eventually came from e^+e^- annihilation experiments.[4,5,6]

Apart from these annihilation experiments, the evidence for charm production is unclear. Cazzoli, et al.,[8] have reported a single candidate for a neutrino induced charmed baryon in a bubble chamber experiment at BNL. Knapp, et al.,[7] observe a signal at the same mass (2.26 Gev/c^2) in photon interactions, but in the charge conjugate state. They find no evidence for a baryon state.

The goal of this experiment was to detect the two-body decay of neutral charmed mesons created in hadronic interactions, near the charm threshold.

II. CHARM: THE RATIONALE

To understand the reason for the introduction of a fourth so-called 'charmed' quark, we first consider weak hadronic physics with only the three conventional quarks p, n and λ.

The weak, charged hadronic current can be written in the form:

$$j_H^\alpha = \cos\theta\, \bar{p}\, \gamma^\alpha (1+\gamma_5)\, n + \sin\theta\, \bar{p}\, \gamma^\alpha\, (1+\gamma_5)\, \lambda$$

where p, n and λ represent the fields for the three quarks, and the γ's are the usual Dirac operators. We may compress our notation by writing:

$$j_H^\alpha = \bar{q}\, M_H\, Q^\alpha q$$

where

$$Q^\alpha = \gamma^\alpha (1+\gamma_5) \qquad M_H = \begin{bmatrix} 0 & \cos\theta & \sin\theta \\ 0 & 0 & 0 \\ 0 & 0 & 0 \end{bmatrix} \quad (1)$$

$$q = \begin{pmatrix} p \\ n \\ \lambda \end{pmatrix}$$

We note that the strangeness changing part of the charged current is suppressed relative to the strangeness conserving part by the usual factor of $\tan\theta$, where θ is the Cabbibo angle. Following the paper of Glashow, Iliopoulos and Maiani, we calculate the neutral hadronic current:

$$j_{Ho}^\alpha = \bar{q}\, M_H^o\, Q^\alpha\, q \qquad (2)$$

using

$$[M_H, M_H^{\dagger}] = M_H^o \quad . \tag{3}$$

Substituting M_H and $M_H^{\dagger}$ into equation (3) we find:

$$M_H^o = \begin{bmatrix} 1 & 0 & 0 \\ 0 & -\cos^2\theta & -\cos\theta\sin\theta \\ 0 & -\cos\theta\sin\theta & -\sin^2\theta \end{bmatrix} \tag{4}$$

or, more explicitly:

$$j_{Ho}^{\alpha} = \bar{p}\, Q^{\alpha}\, p - \cos^2\theta\, \bar{n} Q^{\alpha}\, n - \sin^2\theta\, \bar{\lambda}\, Q \quad \lambda$$
$$- \cos\theta\sin\theta\, \bar{\lambda}\, Q^{\alpha}\, n - \cos\theta\sin\theta\, \bar{n}\, Q \quad \lambda$$

We note that the first three terms are strangeness conserving while the last two terms involve transitions between strange and non-strange quarks. The contribution of these terms to the decays $K_2 \rightarrow \mu^+\mu^-$, $K^+ \rightarrow \pi^+\ell^+\ell^-$ and the K-$\bar{K}$ mass splitting are in contradiction with experiment.[10] One reason for the introduction of charm was to suppress these unwanted and unobserved decays.

To see how this suppression occurs, and to better understand the decay of charmed particles, we repeat the above calculation with the addition of a fourth quark. As before, we write:

$$j_H^\alpha = \bar{q} \; M_H \, Q^\alpha q$$

where q is now the column four-tuple ($cpn\lambda$) and M_H is a four by four matrix. As is customary, we assume the fourth quark (c) to be an isosinglet, to have charge + 2/3, with baryon number 1/3 and to possess a new quantum number called charm. (The properties of the four quarks are summarized in Table II-1.)

With this convention, the charged current must be of the form:

$$j^\alpha{}_H = \cos\theta \; \bar{p} \; Q^\alpha n + \sin\theta \; \bar{p} \; Q^\alpha \lambda + A \; \bar{c} \; Q^\alpha n + B \; \bar{c} \; Q^\alpha \lambda \tag{5}$$

where the constants A and B are determined by the requirement that there be no strangeness changing neutral current. M_H then acquires the form:

$$M_H = \begin{bmatrix} 0 & 0 & A & B \\ 0 & 0 & \cos\theta & \sin\theta \\ 0 & 0 & 0 & 0 \\ 0 & 0 & 0 & 0 \end{bmatrix} \tag{6}$$

To calculate the neutral current we proceed as before, computing M_H^o from the commutator of M_H and $M_H^\dagger$. Substituting from equation (6) we obtain:

TABLE II-1. QUARK PROPERTIES

Flavor	Spin	Baryon#	Charge	Isospin	(I_z)	Strangeness	Charm
p	1/2	1/3	+ 2/3	1/2	(1/2)	0	0
n	1/2	1/3	- 1/3	1/2	(-1/2)	0	0
λ	1/2	1/3	- 1/3	0	0	-1	0
c	1/2	1/3	+ 2/3	0	0	0	+1

$$M_H^o = \begin{bmatrix} A^2 + B^2 & 0 & 0 & 0 \\ 0 & 1 & 0 & 0 \\ 0 & 0 & -(A^2 + \cos^2\theta) & -(AB + \sin\theta\cos\theta) \\ 0 & 0 & -(AB + \sin\theta\cos\theta) & -(B^2 + \sin^2\theta) \end{bmatrix}$$

The strangeness changing part of the neutral current is then given by:

$$j_{Ho}^{\alpha}\ (\Delta S \neq 0) = -\ (AB + \sin\theta\cos\theta)\bar{\lambda}\ Q^{\alpha} n$$
$$-\ (AB + \sin\theta\ \cos\theta)\bar{n}\ Q^{\alpha}\lambda$$

To eliminate these terms we need only set

$$A = \pm \sin\theta \qquad B = \mp \cos\theta$$

Following the convention of Glashow, Iliopoulos and Maiani we choose:

$$A = -\ \sin\theta \qquad B = +\ \cos\theta$$

This choice preserves the similarity between the weak, neutral hadronic current and the weak, neutral leptonic current. The matrix we have defined here as M_H^o is, in fact, equal to its leptonic counterpart M_L^o. Finally, the total, neutral, hadronic current is given by:

$$j_{Ho}^{\alpha} = \bar{p}\ Q^{\alpha}\ p + \bar{c}\ Q^{\alpha}\ c\ -\ \bar{n}\ Q^{\alpha}\ n - \bar{\lambda}\ Q^{\alpha}\lambda$$

and the strangeness changing part has disappeared.

Substituting the values of A and B into the expression for the charged current (5) we find:

$$\mathcal{J}_H^\alpha = \cos\theta \, \bar{p} \, Q^\alpha \, n + \sin\theta \, \bar{p} \, Q^\alpha \, \lambda$$
$$+ \cos\theta \, \bar{c} \, Q^\alpha \lambda - \sin\theta \, \bar{c} \, Q^\alpha \, n$$

One major prediction of the theory becomes clear: charmed particles should decay preferentially into strange particles versus non-strange particles by a factor of $\cot^2 \theta \cong 13$.

With the addition of the charmed quark, there should exist new collections of particles differing from conventional particles by the substitution of a charmed quark for one or more of the familiar ones. Tables II-2 and II-3 list the properties of the 0^- and 1^- (J^P) charmed mesons, respectively; and Figure II-1 shows the predominant decay modes for the charmed mesons. The object of the present experiment was to search for the state D^0 ($\bar{D}^0$) by observing its two body decay into $K^- + \pi^+$ ($K^+ + \pi^-$). For this purpose we pursued three experimental programs.

The first was to observe charm production in anti-proton interactions near threshold; eg.,

$$\bar{P} + N \rightarrow D^0 + \bar{D}^0$$

or inclusively:

$$\bar{p}N \rightarrow D^0 + \bar{D}^0 + X \quad .$$

TABLE II-2. CHARMED 0^- MESONS

Label	Quark Content	Isospin	(I_z)	Strangeness
D^+	$c\bar{n}$	1/2	$(+\ 1/2)$	0
D^o	$c\bar{p}$	1/2	$(-\ 1/2)$	0
F^+	$c\bar{\lambda}$	0		+ 1
η	$\sqrt{\frac{1}{6}}\,(p\bar{p} + n\bar{n} - 2\lambda\bar{\lambda})$	0		0
η'	$\frac{1}{2}\,(p\bar{p} + n\bar{n} + \lambda\bar{\lambda} + c\bar{c})$	0		0
η_c	$\frac{1}{12}\,(p\bar{p} + n\bar{n} + \lambda\bar{\lambda} - 3c\bar{c})$	0		0
D^-	$\bar{c}n$	1/2	$(-\ 1/2)$	0
$\bar{D}^o$	$\bar{c}p$	1/2	$(+\ 1/2)$	0
F^-	$\bar{c}\lambda$	0		- 1

TABLE II-3. CHARMED 1^- MESONS

Label	Quark Content	Isospin	(I_z)	Strangeness
D^{*+}	$c\bar{n}$	1/2	(+ 1/2)	0
D^{*0}	$c\bar{p}$	1/2	(- 1/2)	0
F^{*+}	$c\bar{\lambda}$	0		+1
ω	$\frac{1}{\sqrt{2}}(p\bar{p} - n\bar{n})$	0		0
ϕ	$\lambda\bar{\lambda}$	0		0
$\phi_c(J/\psi)$	$c\bar{c}$	0		0
D^{*-}	$\bar{c}n$	1/2	(- 1/2)	0
$\bar{D}^*$	$\bar{c}p$	1/2	(1/2)	0
F^{*-}	$\bar{c}\lambda$	0		-1

Figure II-1: Decay modes of charmed non-strange mesons (after reference 33). Observed decay modes of D^0 and D^+ are shown.

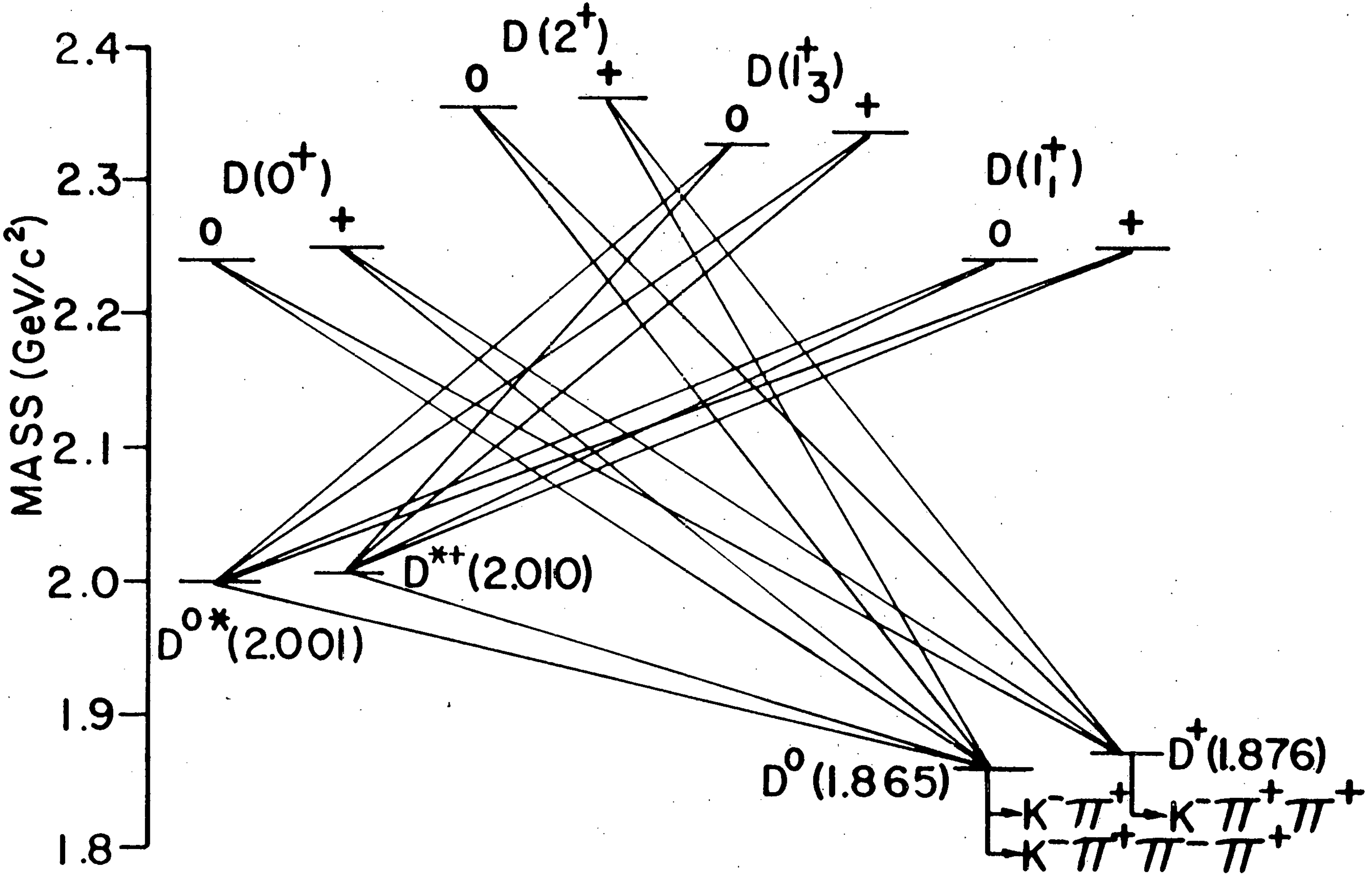

Secondly, because the experiment was conducted in an unseparated beam, we used pions to search for charm in associated production; eg.

$$\pi^- N \to \bar{D}^0 \quad (D^0) \quad + \quad X$$

where X is, for example, a charmed baryon.

Thirdly, once the masses of the charmed mesons became known, we developed a technique for observing charm production via the cascade process:

$$\begin{array}{l} \pi^- N \to D^{*-} + X \\ \qquad\quad \lfloor\!\!\to \pi^- \bar{D}^0 \\ \qquad\qquad\quad \lfloor\!\!\to K^+ \pi^- \end{array}$$

Finally, in an experiment pararastic to the ones listed above, we used the spectrometer tosearch for J/ψ production via:

$$\begin{array}{l} \pi^- N \to J/\psi \quad + \quad X \\ \qquad\quad \lfloor\!\!\to \mu^+ \mu^- \end{array} \quad .$$

In Table II-4 we list all of the energies at which we collected data along with the process we were seeking to observe.

TABLE II-4: SUMMARY OF EXPERIMENTAL PROGRAM

BEAM MOMENTUM	BEAM PARTICLE	PROCESS OF INTEREST
15.0 GeV/c	$\bar{P}$	$\bar{P}N \to D\bar{D} + X$
15.0 GeV/c [b]	π^-	$\pi^- N \to D\ (\bar{D}) + X$
12.4 GeV/c [a]	$\bar{P}$	$\bar{P}N \to D\bar{D}$ or $PN \to D\bar{D} + X$
8.5 Gev/c [b]	$\bar{P}$	$\bar{P}N \to D\bar{D}$
10.5 GeV/c	π^-	$\pi^- N \to D^{*-} + X$
15.0 & 12.4 GeV/c	π^-	$\pi^- N \to J/\psi + X$

---

[a] Process depends on mass of D. For exclusive channel $M_D \simeq 2.3$ GeV/c^2; inclusive channel for less massive D's.

[b] Results depend on mass of charmed baryon. See Chapter V.

III. A LITTLE HISTORY

The J/ψ (3095) is usually described as 1^3S_1 $c\bar{c}$ bound state and its companion, the ψ' (3695), a 2^3S_1 radial excitation[11]. Both particles have lifetimes approximately 10^3 times longer than expected for strongly interacting particles of mass 3 to 4 Gev/c^2. If charmed particles of sufficiently low mass existed, one would expect the J/ψ or its companion, the ψ', to decay strongly via J/$\psi \rightarrow D\bar{D}$, analogous to the decay of the $\phi \rightarrow K^+K^-$. The narrow width of the J/ψ and the ψ' imply that this strong decay is not energetically possible; that is, the J/ψ and the ψ' lie below the threshold for producing $D\bar{D}$ and must therefore decay weakly into non-charmed particles. The enchancement in the e^+e^- annihilation cross section at center of mass energies above 4 Gev was interpreted to be due to the formation of higher mass relatives of the J/ψ which decay strongly into particles with naked charm.[12] Hence the expected mass for the lowest lying charmed state, the D^0, was predicted to be in the range $1.85 \leq M_D \leq 2.3$ Gev/c^2.

Models for production of charm are, in general, sensitive to the anti-quark content of the initial state particles. Most models are of a Drell-Yan type; where, for example, J/ψ production proceeds through quark-anti-quark annihilation (See Figure III-1). Anti-proton or pion interactions should then be good candidates for charm production.

This conclusion seems reasonable when we compare inclusive production cross sections for $p + \bar{p} \rightarrow K_L + K_S$ and $p + p \rightarrow pp + K_0 + \bar{K}_0$ as shown in Figure III-2.

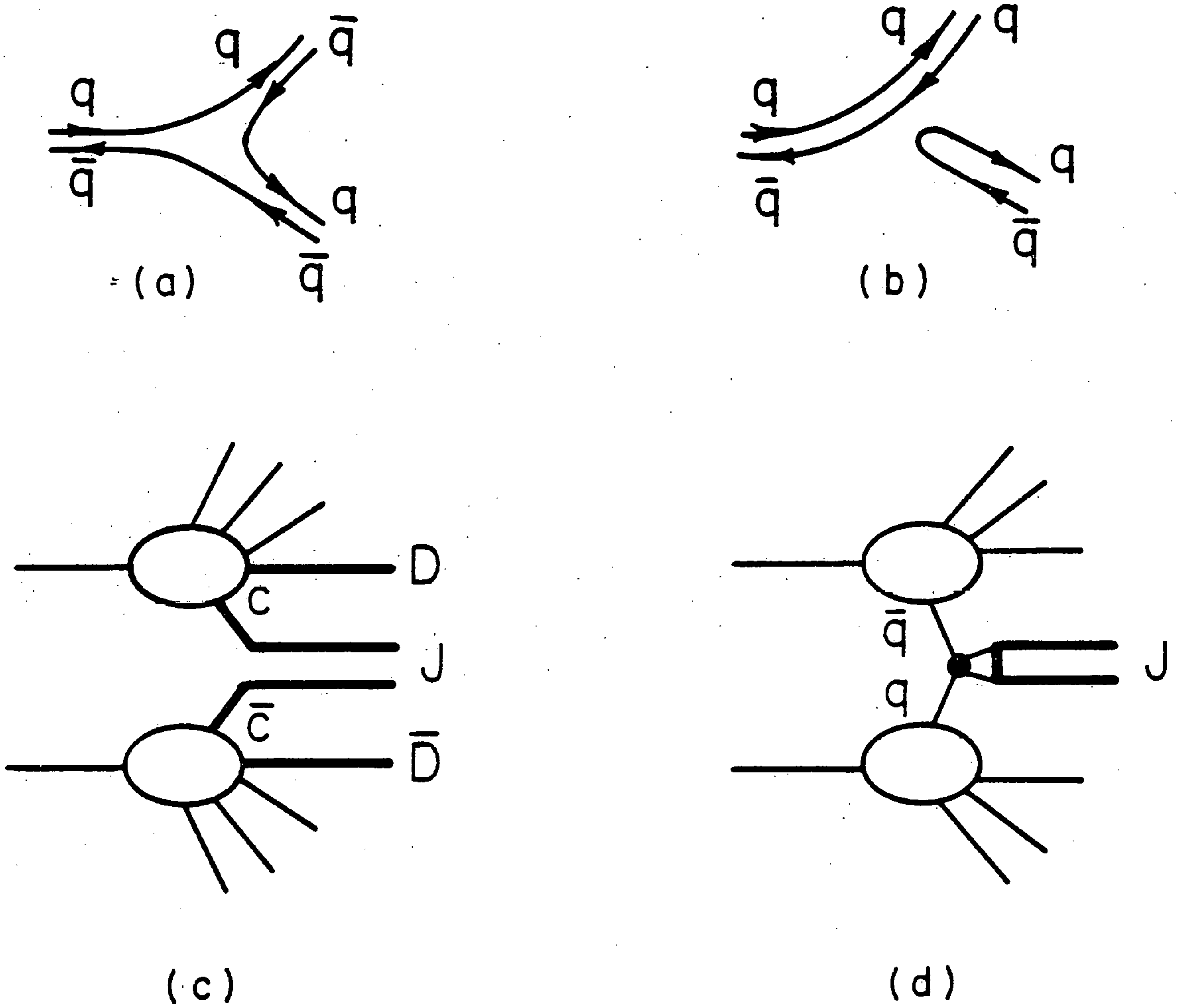

Figure III-1: (a) Zweig allowed process; (b) Zweig forbidden process; (c) Zweig allowed J production; (d) J production via $q\bar{q}$ annihilation.

We note that strangeness is produced about 50 times more copiously in anti-proton interactions near threshold as compared to proton interactions. This, coupled with the relatively high $p\bar{p}$ annihilation cross section of 30 mb at $s \simeq 18$ (equal to about 1/2 the total inelastic cross section), was the reason we choose to look for charm production in π^- and anti-proton interactions. It should be noted here, however, that in the J/ψ production experiments of Branson[13], et al., J/ψ production by pions is only slightly more favorable than by protons.

Guided by the analogy with strangeness, it is possible to make estimates for D production cross sections by assuming (naively) that charm production is suppressed relative to strange particles by a factor which depends solely on the higher mass of the charmed particles.[14] Gaillard, Lee and Rosner[12] assume a factor of the form $f(M) \cong M^{-2}$. The cross section for $\bar{p} + p \rightarrow K^+ + K^-$ is approximately .13 mb at center of mass energies ~ 1 Gev above threshold. For $(M_K/M_D)^2 \sim 1/20$, they predict $\sigma\,(p\bar{p} \rightarrow D\bar{D})$ should be on the order of 10^{-29} cm^2.

Recent theories tend to give estimates lower by at least an order of magnitude, assuming that one can obtain estimates of $\sigma\,(p\bar{p} \rightarrow D\bar{D})$ by multiplying the predictions for proton induced cross section by a factor of ~ 50.

Gaillard and Bourguin[15] have estimated charm production in pN interactions on the basis of inclusive single particle spectra. Their results include a suppression factor for Zweig violating processes (eq. $pp \rightarrow JD\bar{D} + X$ versus $pp \rightarrow J + X$ see Figure III-1) as well as a factor proportional to $\sim M^{-11}$ for the suppression of high

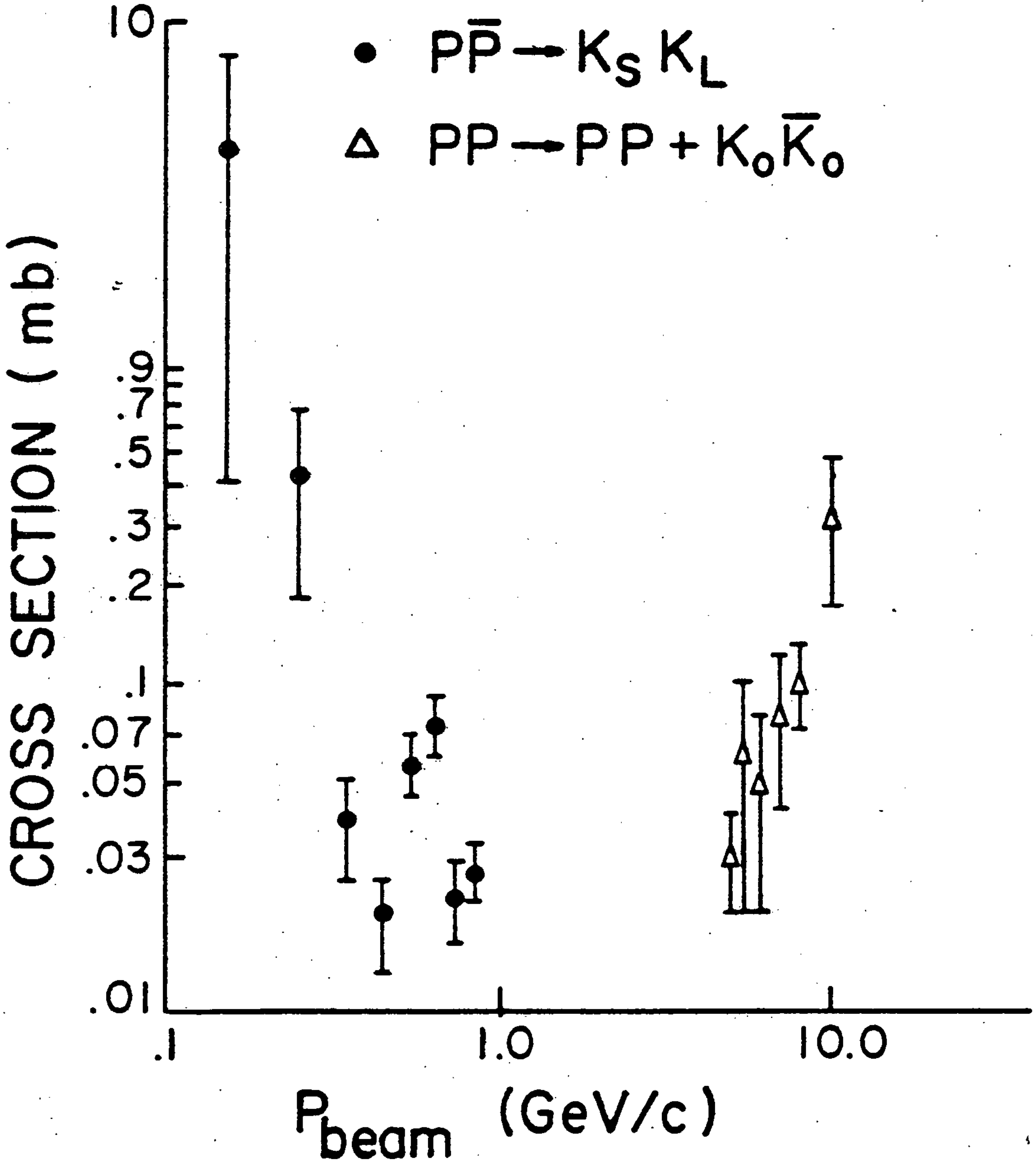

Figure III-2: Comparison of strange particle production in anti-proton and proton interactions.

mass objects. Such factors have been suggested, for example, by Lipkin[16], to explain the suppression of $pp \to \phi + K^+ + K^- + X$ (Zweig allowed) compared to $pp \to \phi + X$ (Zweig violating). The results of Bourguin and Gaillard are shown in Figure III-3. Multiplying by a factor of 50 to reflect incoming anti-protons we estimate:

$$\sigma\ (p\bar{p} \to D\bar{D},\ \sqrt{s} \cong 5\ \text{Gev}\ ) \cong 5 \times 10^{-31}\ \text{cm}^2$$

Sivers[17] has estimated charm production in pp and πp interactions in a Drell-Yan model, adopting the quark distribution functions suggested by constituent counting rules. His predictions are also shown in Figure III-3. Multiplying by the usual factor we obtain:

$$\sigma\ (p\bar{p} \to D\bar{D}) \cong 2 \times 10^{-31}\ \text{cm}^2.$$

In a slightly different model, Landshoff and Donnachie[18] assume that each valence quark is surrounded by its own 'sea' of anti-quarks. Their results, also shown in Figure III-3, imply similar estimates for D production in anti-proton interactions.

Recent data indicate that instead of the M^{-2} dependence assumed by Gaillard, Lee and Rosner, high mass production is suppressed by a factor of $e^{-25M/\sqrt{s}}$ near threshold.[17] Combining this with the previously quoted cross section for $p\bar{p} \to K^+ + K^- + X$, we obtain

$$\sigma\ (p\bar{p} \to D\bar{D}) \cong 10^{-30}\ \text{cm}^{-2}.$$

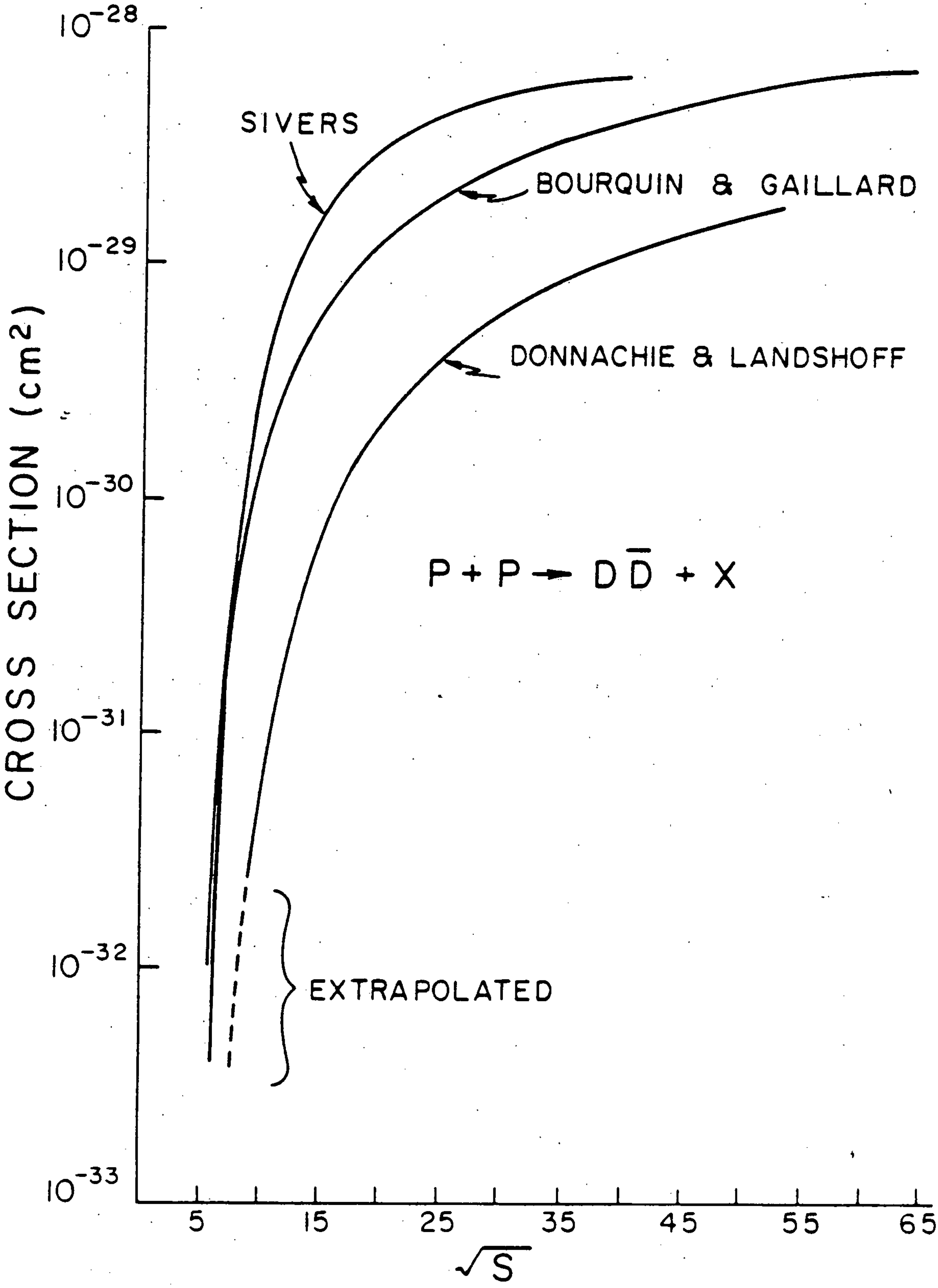

Figure III-3: Theoretical estimates for $D\bar{D}$ production in proton interactions.

Comparing these estimates we would expect to see charm at the level of a few times 10^{-31} cm^2 in $\bar{p}N$ interactions near the charm threshold. Assuming a branching ratio for $D \rightarrow K\pi$ of approximately 2%[19], we require a sensitivity of about 10 nb. All of these production models are extremely soft and largely empirical. It is the task of the experimentalist to confirm or deny their usefullness.

IV. THE BEAM

As described in the previous chapter, we chose to search for D^0 mesons produced in anti-proton interactions by observing their decay into a kaon and a pion. The two-body decay channel makes for a relatively clean experimental environment. Because the K and the π emerge with relatively large and opposite values of $P_\perp$, two spectrometer arms are required. The signature for a two-body charmed decay is the final state kaon. Hence,each arm must be capable of identifying pions, kaons and protons. To achieve the highest possible incident flux of anti-protons, an unseparated beam was used, requiring identification of the incoming beam particles. Finally, the spectrometer had to be compact to provide the greatest possible acceptance.

The transverse dimensions of the beam and the relative fluxes of pions and anti-protons strongly influenced the design of the spectrometer. Before describing the individual elements of the spectrometer, it is first necessary to understand the beam characteristics.

The experiment was conducted in the high-energy- unseparated-beam (HEUB - designated B1 in Figure IV-1) of the AGS. Protons of momentum 28 Gev/c incident on a .1" x 4" x 0.04" tungsten target produced the secondary beam particles. Negatively charged particles produced at an angle of 0° relative to the incident proton direction constituted the B1 beam. The relative fluxes of pions, kaons and anti-protons as a function of the B1 beam momentum are shown in Figure IV-2.

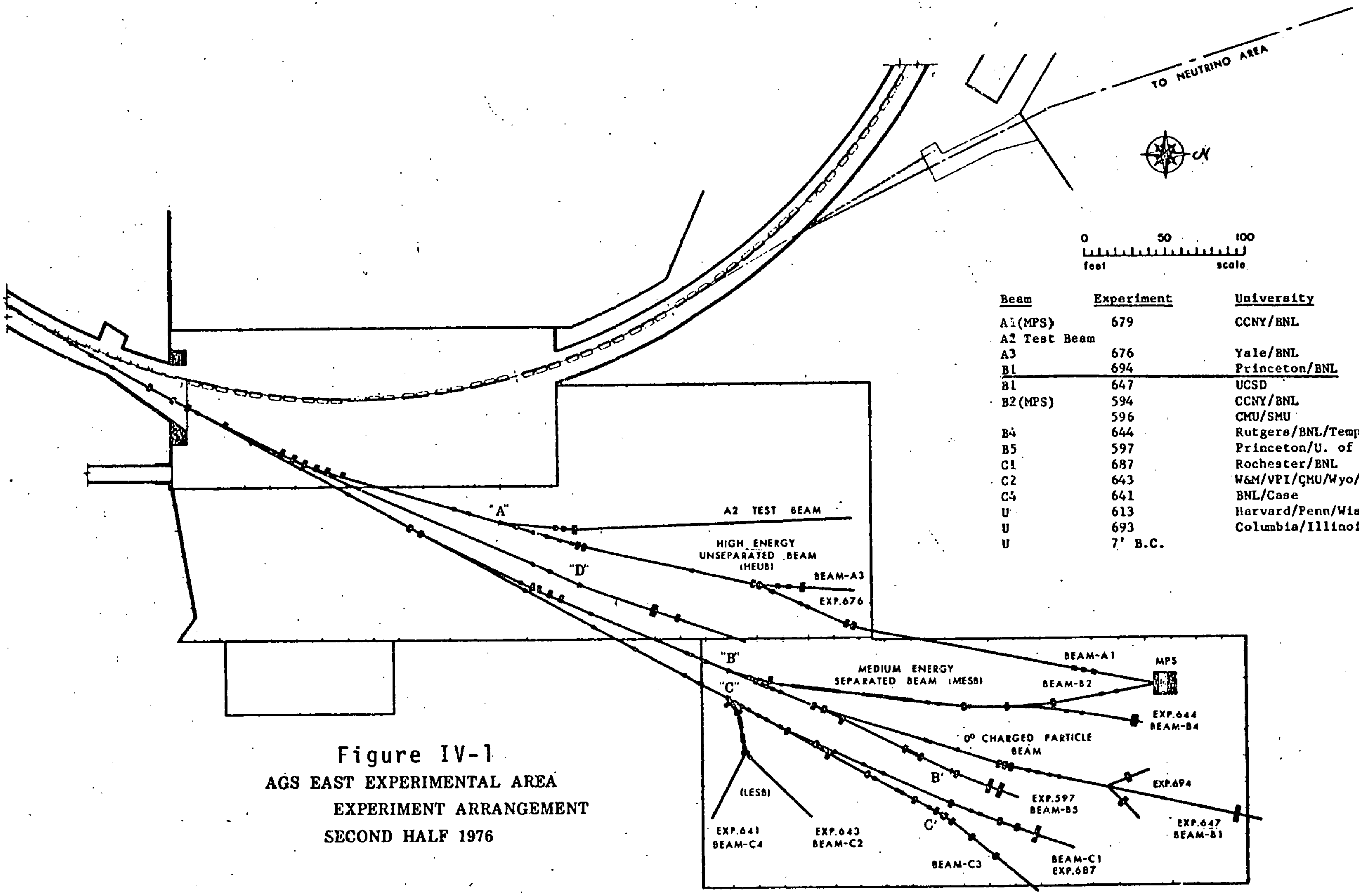

Beam	Experiment	University
A1(MPS)	679	CCNY/BNL
A2 Test Beam		
A3	676	Yale/BNL
B1	694	Princeton/BNL
B1	647	UCSD
B2(MPS)	594	CCNY/BNL
	596	CMU/SMU
B4	644	Rutgers/BNL/Temple
B5	597	Princeton/U. of Mass.
C1	687	Rochester/BNL
C2	643	W&M/VPI/CMU/Wyo/CIT
C4	641	BNL/Case
U	613	Harvard/Penn/Wisc.
U	693	Columbia/Illinois
U	7' B.C.	

Figure IV-1

AGS EAST EXPERIMENTAL AREA
EXPERIMENT ARRANGEMENT
SECOND HALF 1976

Figure IV-2

PARTICLE FLUXES
B1 (HEUB) BEAM

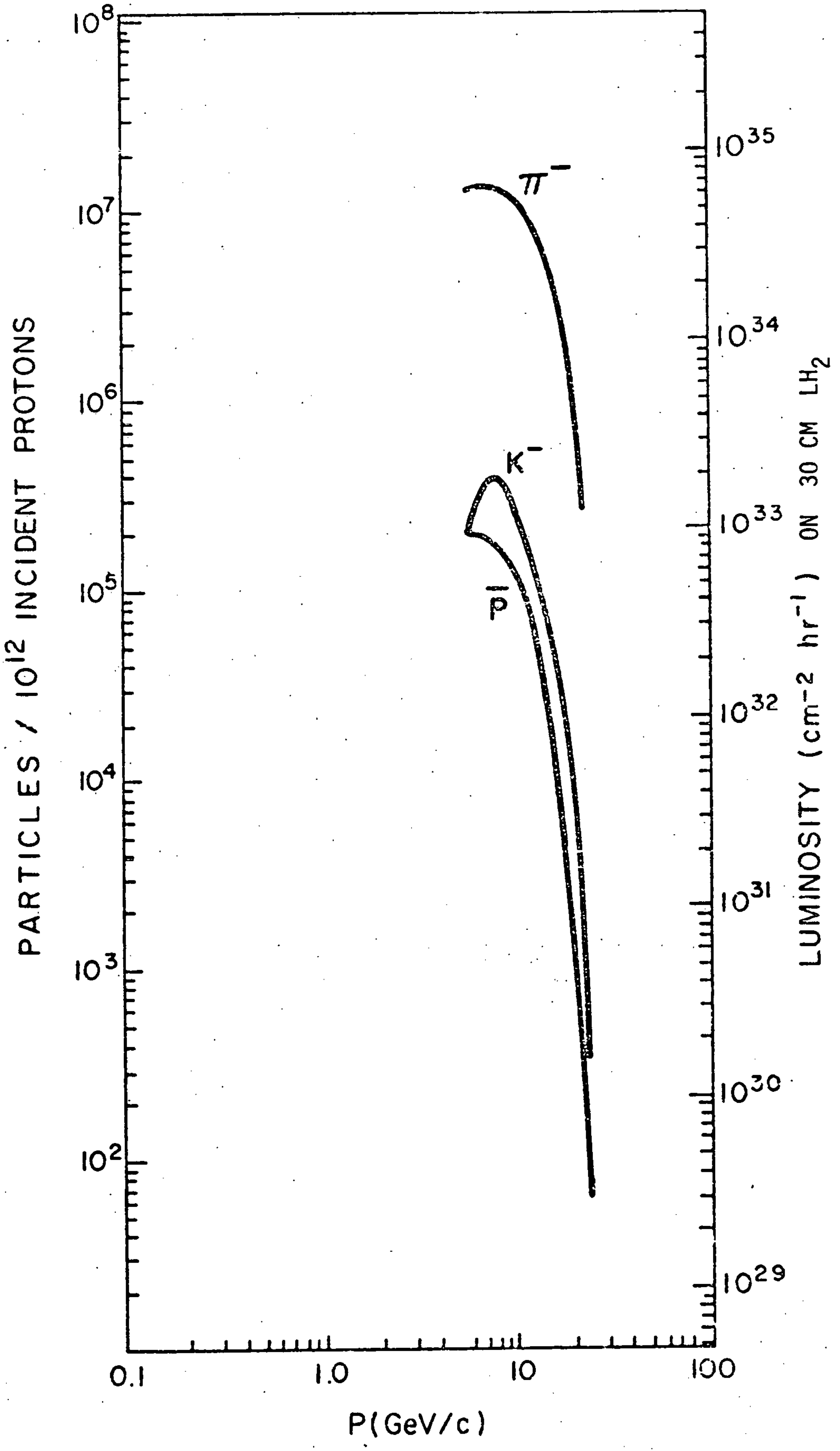

The B1 beam line was designed with two criteria in mind: 1) good momentum resolution and 2) minimal angular divergence. A parallel beam was required to achieve good efficiency in the beam Cherenkov counter. Given the angular divergence of the beam the transverse dimensions of the beam are determined by the emittance of the beam line.

The configuration of collimators, dipole and quadrapole magnets which optimized the beam flux with respect to the above criteria is shown in Figure IV-3. The momentum resolution of the beam (determined by adjustable collimator C2) is calculated to be $\Delta P/P \leq \pm 3\%$. The angular divergence of the beam at the beam Cherenkov counter (BC3) is 5 mrad in the horizontal (x) direction and 2 mrad in the vertical (y) direction. The transverse dimensions of the beam at the secondary target are $(\Delta x) \times (\Delta y) = 1'' \times 2''$.

Beam halo particles were eliminated by absorption in a Heavimet and lead collimator (C3) or by producing signals in one of two 'veto' scintillation counters downstream of the beam Cherenkov. These 'veto' or 'hole' counters were designed such that only off-axis particles would transverse the plastic scintillator. Signals from these two counters were used in anti-coincidence with signals from the beam Cherenkov counter. The relevant dimension of the collimators C1, C2 and C3 and the two veto counters, V1 and V2, are summarized in Table IV-1.

Incoming beam particles were identified by the high-pressure, differential beam Cherenkov counter shown in cross-section in Figure IV-4a. Cherenkov radiation emitted by beam particles passing through the

Figure IV-3

BNL AGS UNSEPARATED BEAM 0° PRODUCTION

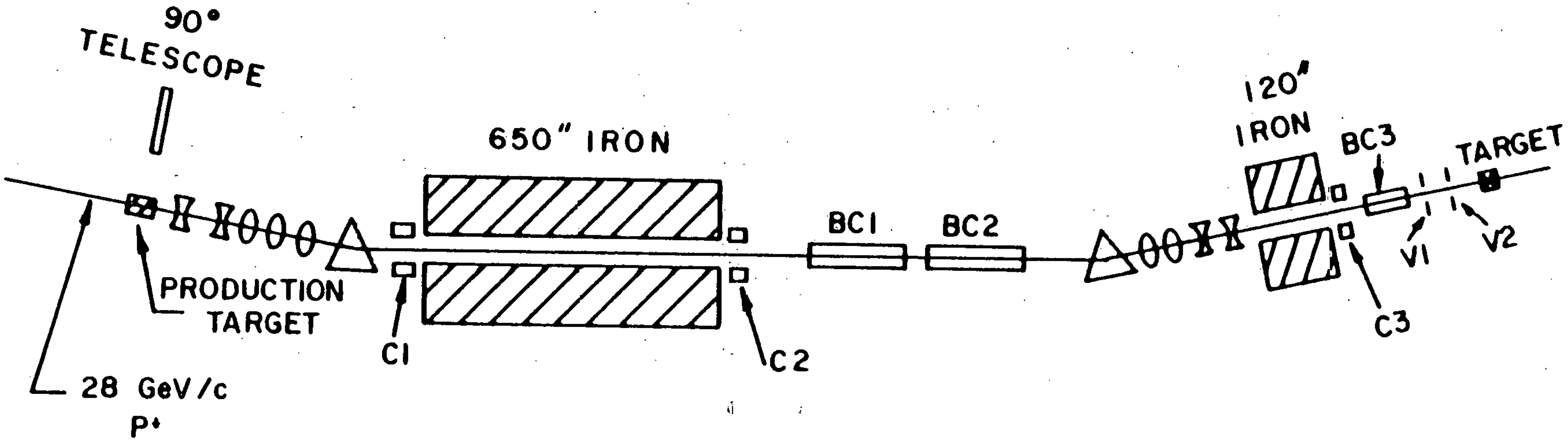

TABLE IV-1: COLLIMATOR AND SCINTILLATOR DIMENSIONS

	DIMENSION					Z (FROM ℄ TARGET)	ΔZ (THICKNESS OR LENGTH)
	A	B	C	D	R		
C1: 4 HOLE COLLIMATOR	~ -	~ -	1/4"	1/2"	N/A	~ -1066"	~ 36"
			1/2"	1"			
			1"	2"			
			4"	5"			
C2: MOMENTUM SLIT	~ -	~ -	ADJ 0 → 3"	ADJ 0 → 3"	N/A	~ -768"	~ 24"
C3:	15"	14"	6"	5"	N/A	~ -96"	16"
TARGET:	N/A	N/A	N/A	N/A	N/A	0	N/A
S1: OVERALL	4"	4"	N/A	N/A	N/A	15"*	1/8"
1 COUNTER	1"	4"					
1 COUNTER	3"	4"					
S2: OVERALL	12"	30"	N/A	N/A	N/A	159"*	1/8"
2 COUNTERS EACH	9"	30"					
S3: OVERALL	16"	54"	N/A	N/A	N/A	199"*	1/4"
3 COUNTERS EACH	16"	18"					
S4: OVERALL	24"	88"	N/A	N/A	N/A	247"*	1/4"
4 COUNTERS EACH	24"	22"					
S5: OVERALL	30"	96"	N/A	N/A	N/A	295"*	-
5 COUNTERS EACH	18"	18"					1/4"
2 COUNTERS EACH	12"	48"					1/2"
V1: VETO COUNTER	12"	6"	3"	2"	N/A	-36"	1/4"
V2: VETO COUNTER	6.2"	6.2"	N/A	N/A	1"	-14"	1/8"

---

* Coordinate measured along spectrometer arm axis

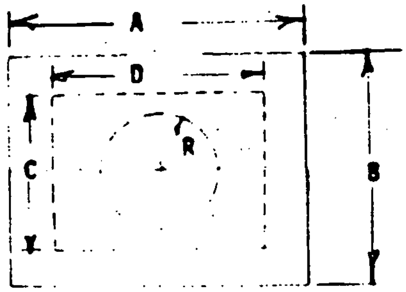

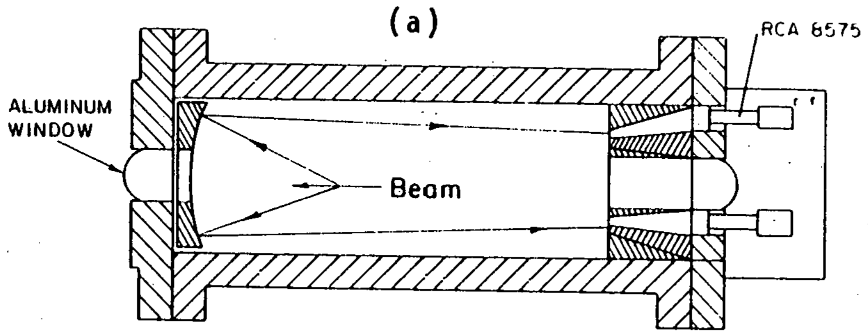

BEAM CHERENKOV COUNTER

Figure IV-4

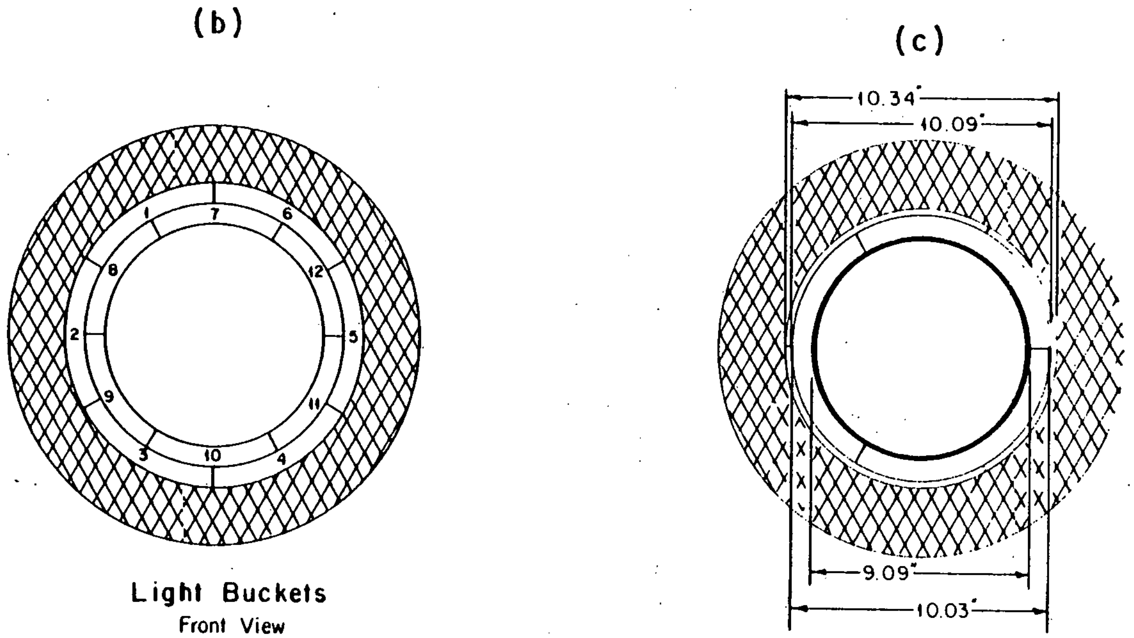

Light Buckets
Front View

Aperture Mask

Cherenkov medium (CO_2 or Freon 13) was focused by a spherical mirror onto a mask (Figure IV-4c) covering twelve photomultiplier tubes (RCA type 8575) arranged in two rings concentric with the beam line. For a given gas pressure, only light produced from particles with the correct velocity will be focused onto the annular slit in the mask. Thus, for a fixed beam momentum, as the gas pressure is increased the Cherenkov counter becomes sensitive to pions, kaons and finally protons. Figure IV-5 is a plot of the number of 3, 4 and 5-fold coincidences among the six phototubes of the inner ring as a function of the pressure of the Cherenkov gas (CO_2). The pion and proton peaks are clearly visible, as well as a kaon 'shoulder' on the pion peak. Figure IV-6 is an enlarged plot of the anti-proton peak. If one assumes there are approximately 200 pions for every anti-proton (see Figure IV-2), the pion rejection ratio in the proton peak is approximately 5×10^{-4} at this energy and incident flux. Corresponding data different energies and gases is summarized in Table IV-2.

As has been mentioned, the efficiency of the beam Cherenkov was sensitive to the alignment of the optical axis with the beam line. To insure that the optical axis of the Cherenkov was coincident with the beam the following procedure was used. First, the efficiencies of the individual phototubes were checked. A well collimated (1/4" x 1/4") beam of pions was passed down the beam line. The Cherenkov gas pressure (CO_2) was adjusted so that the pion Cherenkov light would be focused onto the inner ring of phototubes. The high voltage supplied to each phototube was adjusted so that all six tubes gave signals of the same amplitude (~ 1 volt). With few exceptions, all of the

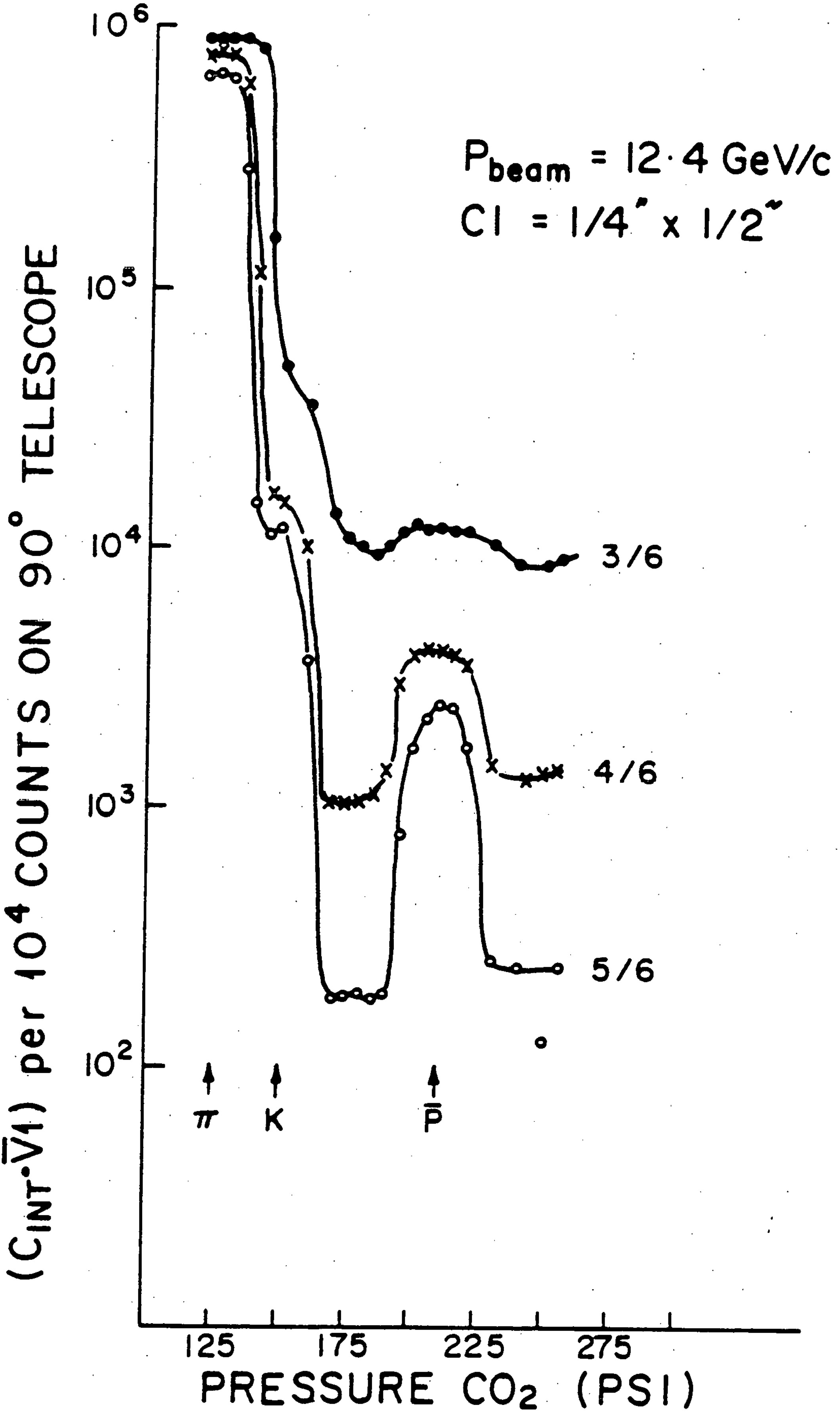

Figure IV-5: Beam Cherenkov counter pressure curve for negative 12.4 Gev/c incoming beam. Cherenkov gas was CO_2.

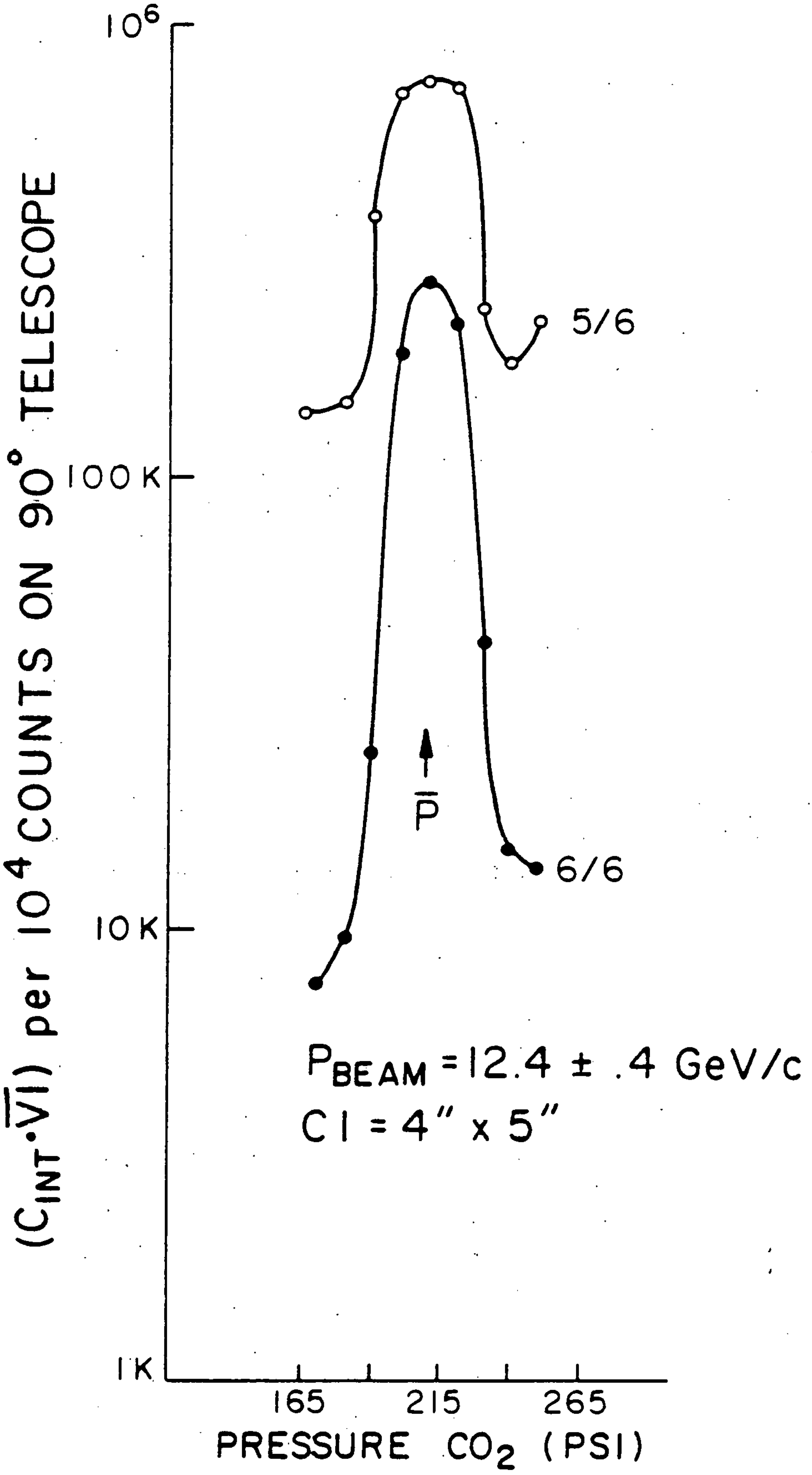

Figure IV-6: Pressure curve for anti-proton peak in beam Cherenkov counter.

TABLE IV-2: BEAM CHERENKOV COUNTER

MOMENTUM (GeV/c)	GAS	PRESSURE AT $\overline{P}$ PEAK (PSI)	$\overline{P}$ SIGNAL TO NOISE ($C_{INT} = 6/6$)
8.5	FREON 13	180	10:1
12.4	CO_2	210	26:1
15.0	CO_2	180	15:1

photomultiplier tubes used in this experiment operated with positive high voltage, the photocathodes at ground. This tended to reduce the dark currents and protected the photocathodes from evaporation. To test the efficiency of an individual phototube, we plotted the ratio of five-fold coincidences versus six-fold coincidences as a function of the high voltage on the sixth tube. Figure IV-7 is typical of an efficiency curve (or 'plateau' curve) produced in this manner. For this phototube the high voltage was set at 2.875 kilovolts. The procedure was repeated for the other five tubes of the inner ring. A similar procedure was followed for the six phototubes of the outer ring. For the data reported here, neither the outer ring of phototubes nor the beam threshold counters BC1 or BC2 was used.

The Cherenkov counter could now be aligned as follows: let $R_{a,a+1,a+2}$ be the rate of three-fold coincidences in consecutive phototubes a, a+1 and a+2 (modulo 6). The horizontal and vertical position of the Cherenkov counter was adjusted so that R was independent of a.

In general, the only parameter of the Cherenkov counter continuously monitored during the course of the experiment (aside from the ratio of primary protons to five-fold coincidences) was the pressure of the Cherenkov gas. The efficiency of the Cherenkov counter is, of course, sensitive to changes of temperature as well as pressure. We calculate the sensitivity of the Cherenkov counter to small changes in temperature, starting with the familiar relation between velocity β (= v/c), the index of refraction (n) and the Cherenkov angle (θ):

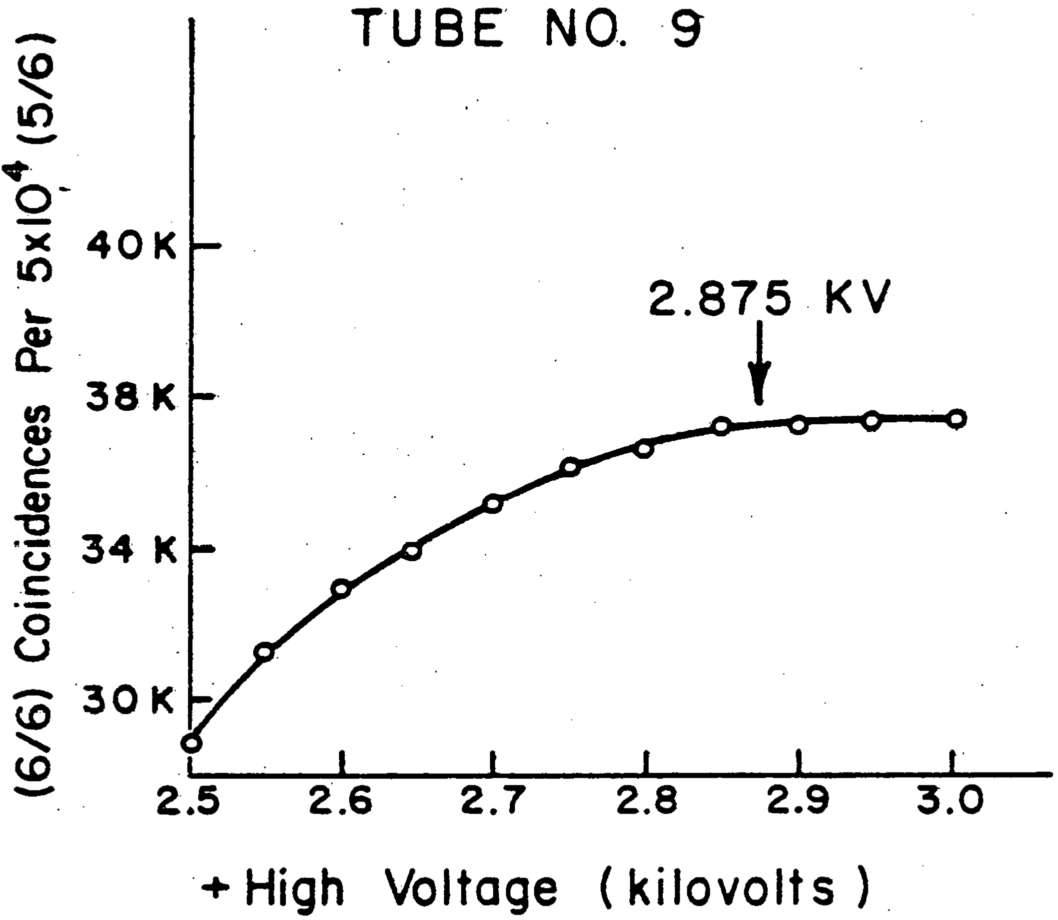

Figure IV-7: Typical efficiency curve for phototube of inner ring in beam Cherenkov counter.

$$\cos\theta = 1/n\beta$$

Let $n = 1 + \varepsilon,\ \varepsilon << 1;\ \beta \cong 1 - 1/2\ m^2/P^2,$

where m is the mass of the beam particle and P its momentum. We have:

$$\frac{1}{(1 + \varepsilon)\ (1 - \frac{1}{2}\frac{m^2}{P^2})} \cong (1 - \varepsilon)\ (1 + \frac{1}{2}\frac{M^2}{P^2}) \cong \cos\theta$$

$$- \varepsilon + \frac{M^2}{P^2} \cong - \frac{\theta^2}{2}$$

$$\varepsilon = \frac{M^2}{2P^2} + \frac{\theta^2}{2}$$

To first order ε is proportional to the density (ρ) of the gas given by: $\varepsilon = k\rho = k\ B/T$, where B is the pressure and T the temperature. A small change in temperature (ΔT) corresponds, at fixed pressure, to a change in the index of refraction of $\Delta\varepsilon = - k\ \frac{B\Delta T}{T^2} = - \frac{\varepsilon\Delta T}{T}$. This, in turn, corresponds to a change in momentum of: $\Delta\varepsilon = \frac{-M^2}{P^3}\ \Delta P$. Substituting typical values for ε (~ 5×10^{-3}), $(M/P)^2$ (~10^{-2}) we compute that:

$$\frac{\Delta T}{T} \cong 2\ \frac{\Delta P}{P}$$

Since $\Delta P/P$ is on the order of ± 3%, this implies that $\Delta T/T$ may vary by as much as ± 6%, or for T ~ 300°K, $\Delta T = \pm 18^{\circ}$K; a condition easily satisfied in the AGS environment.

V. THE SPECTROMETER: AN OVERVIEW

According to the discussion of Chapter III, when this experiment was proposed the theoretical estimate for the cross-section $\sigma(\bar{P}N \rightarrow D\bar{D})$ was on the order of 10^{-30} cm^2. This level of sensitivity can only be achieved when strict attention is paid to the differences between the expected characteristics of the decay and the normal hadronic background.

We adopt the form suggested by Becker[21] to describe the perpendicular momentum distribution of the background:

$$\bar{p}N \rightarrow h^{\pm} + X$$

$$\frac{dN_h}{dP_\perp} = P_\perp \; e^{-5T}$$

where h is a hadron (ie. π, K or P), m its mass and $T = \sqrt{3/2\, P_\perp^2 + m^2} - m$. Near the charm threshold, we expect D production to be primarily s-wave. We further assume that the decay of the D into K - π is isotropic in the D center of mass. Hence, the $\langle P_\perp \rangle$ of a K or π originating from D decay is ~ 1 Gev/c. It is clear then that the signal to noise will be best near 90^o in the center of mass, because the background is relatively suppressed at high $P_\perp$. The spectrometer was therefore designed to search for the decay $D^o \rightarrow K^- + \pi^+$ ($\bar{D}^o \rightarrow K^+ + \pi^-$) where the K ($\pi$) emerges at roughly $\pm 90^o$ ($\mp 90^o$) in the center of mass. Recall that the favored mass of the D at the time of the discovery of the J/ψ was 2.3 Gev/c^2. To produce a $D\bar{D}$ pair of this mass just above threshold requires a center of mass energy ($\sqrt{s}$) of approximately 5 GeV or an anti-proton momentum of 12.4 GeV/c. The opening angle between the two arms of the spectrometer is then 36^o, in laboratory coordinates.

The layout of the spectrometer is shown in Figure V-1. The spectrometer is short so that the maximum solid angle (.015 ster radian) is accepted, partially offsetting the relatively low antiproton intensity. Also, because the spectrometer is compact, the effects of decays of the secondary particles can be largely ignored (see below).

Particle trajectories were measured by fourteen planes of drift chambers (labelled DC1 through DC4) in each arm, arranged in pairs to resolve the usual right-left ambiguity (see Chapter VI). Momenta were determined by measuring the deflection of particles in passing through 18D36 dipole magnet turned on its side ($\vec{B}$ in the horizontal plane). This configuration gives a sharp low-momentum cutoff and decouples the measurement of the opening angle between the K and the π from the measurement of their momenta.

Two Cherenkov counters in each arm aided in particle identification. A threshold Cherenkov counter (see Chapter VII) inside the magnet and filled with Freon 13 at atomspheric pressure was used to identify pions of momentum greater than 3 GeV/c ($\beta \geq .998$). A water Cherenkov counter of new design (Chapter VII) was used to identify pions of momentum below 3 Gev/c, as well as protons and kaons of all momenta. Muons were identified by their ability to penetrate approximately 8 feet of iron, corresponding to a minimum energy of 2.5 GeV.

Any interaction in the target producing signals in scintillation counters S1, S2 and S3 in both arms and in coincidence with a valid anti-proton signal from the beam Cherenkov counter was considered a candidate for the decay of a charmed particle (see Figure V-2 for a diagram of the trigger logic).

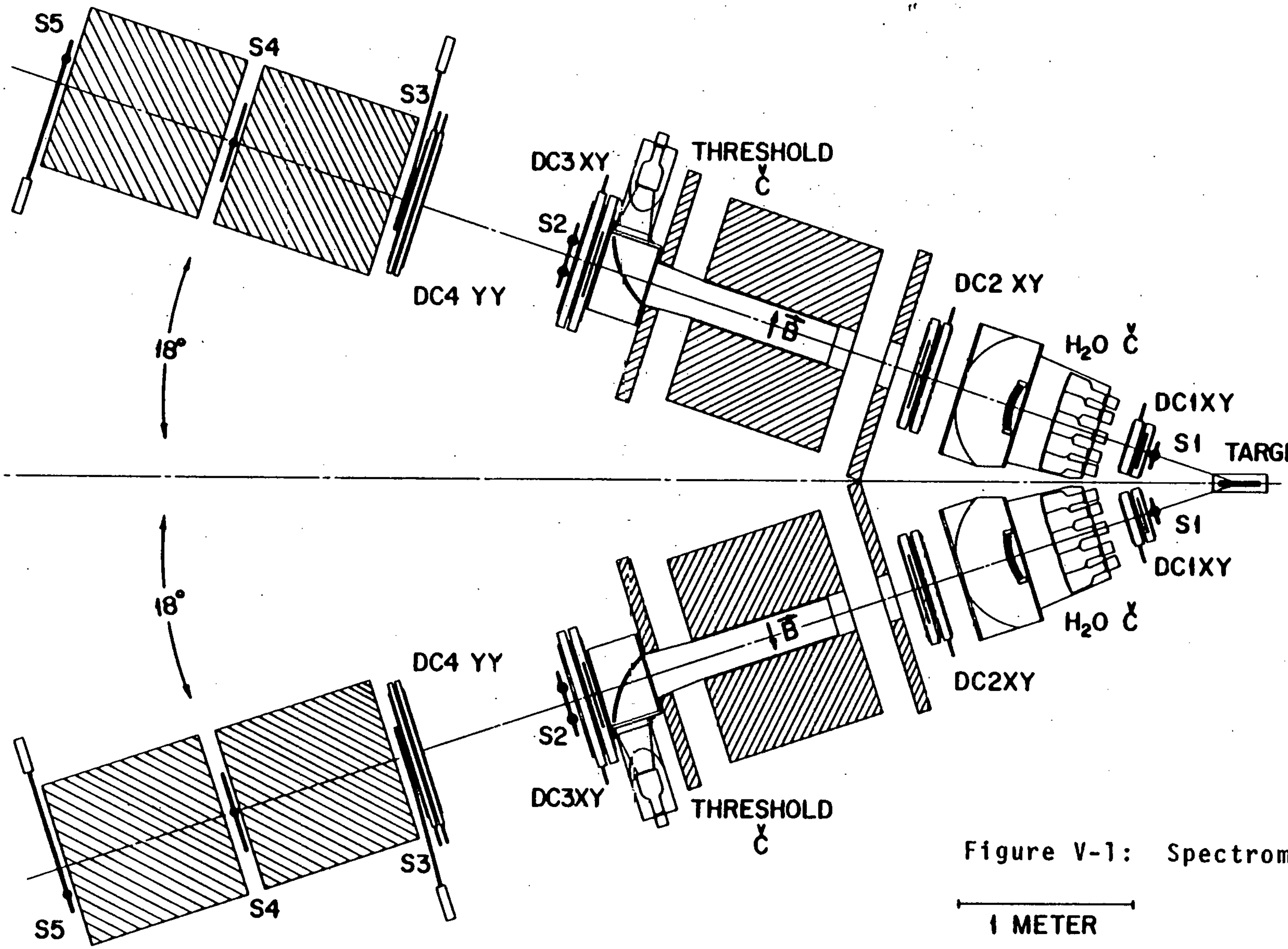

Figure V-1: Spectrometer layout

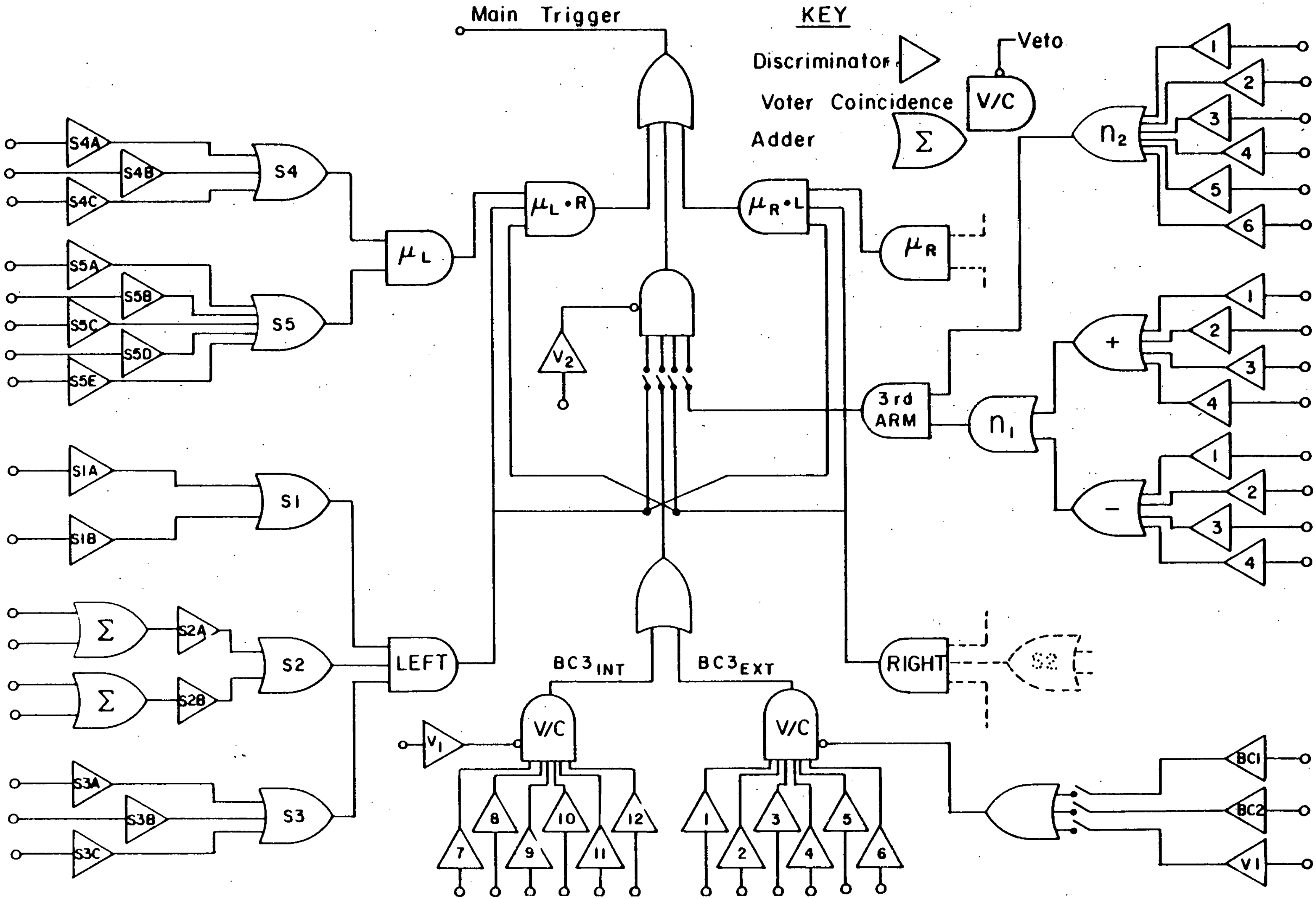

Figure V-2: Trigger Logic

An on-line Hewlett-Packard 2116B computer was used to monitor phototube pulse height information, drift chamber efficiencies and counting rates in the various scintillators. During the beam spill timing information from the drift chambers, all of the phototube information and scaler data for each event were stored in a fast buffer memory (see Figure V-3). At the end of the spill data was transferred from the buffer memory to magnetic tape for off-line track reconstruction and event analysis. The data collection rate was limited by the capacity of the buffer memory to less than about 30 events per beam spill.

The acceptance of the spectrometer was calculated using Monte Carlo techniques which included the effect of target Fermi motion and assumed the production and decay of the D to be isotropic in the center of mass. The acceptance of the spectrometer for $\bar{p}N \to D\bar{D}$ (assuming $M_D = 1.86$ Gev/c^2) is shown in Figure V-4. In general, the acceptance is strongly peaked at a mass equal to about 1/2 the total center of mass energy, assuming two body production, and has a width of approximately ± 200 Mev/c^2. The mass for which the acceptance is maximized is plotted in Figure V-5 for various values of the opening angle of the spectrometer. Also plotted in Figure V-5 is the longitudinal (z) momentum of the accepted D's. We mention also that if the mass of the 1^- charmed mesons is not too much larger than the mass of the D, the acceptance of the spectrometer (when optimized for $\bar{P}N \to D+\bar{D}$) is also large for the exclusive processes:

$$\bar{P}N \to (D\,\bar{D}^* \;;\; D^*\bar{D},\; D^*\bar{D}^*) \qquad (1)$$

Note that while only one D is detected, the acceptance of the spectrometer requires that the system recoiling against the D have roughly the same mass.

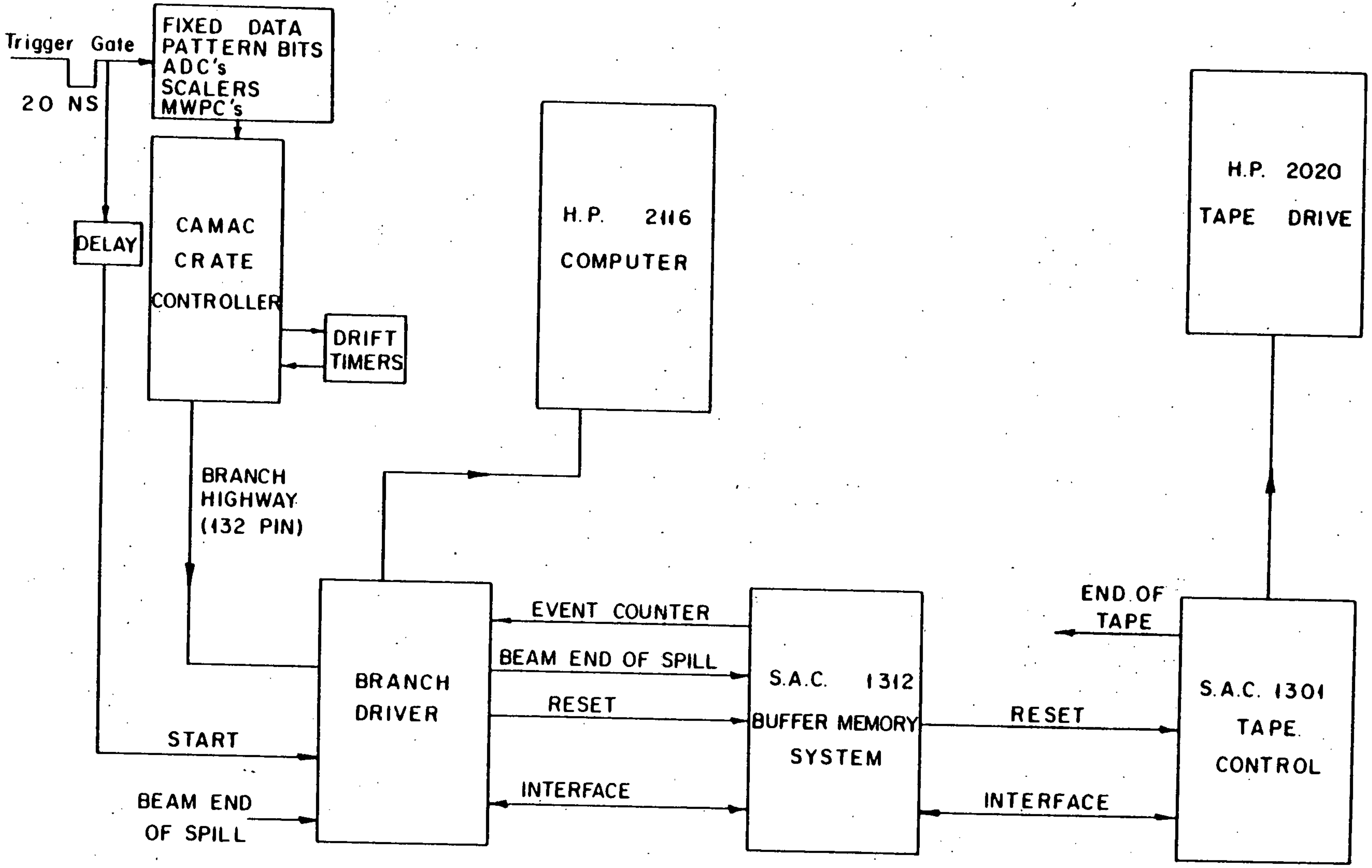

Figure V-3: Data Acquisition system

Furthermore, if the mass of the D is low relative to the beam energy, it is possible to produce the D in an inclusive process, eg:

$$\bar{P}N \rightarrow D\bar{D} + n\pi$$

In Figure V-6 we plot the acceptance of the spectrometer for D's produced inclusively as a function of the beam momentum. We assumed the D was produced with a $P_\perp$ distribution given by:

$$\frac{d\sigma}{dP_\perp} = P_\perp \; e^{-5\sqrt{\frac{3}{2} P_\perp^{2} + M^{2}} \quad -5\,M.}$$

where M is the mass of the D. The production and decay of the D was assumed to be isotropic in the center of mass.

The transverse dimensions of the target were matched to the spotsize of the beam. The target consisted of a 1" x 2" x 9" ($\Delta X \times \Delta Y \times \Delta Z$) carbon block (equivalent to about one absorbtion length) segmented into three pieces of equal length. A shorter target was used with the more intense pion beams.

The Monte Carlo program indicated that the average laboratory momentum of accepted kaons and pions originating from D decays was about 2.8 Gev/c. Exiting the target at 18^{0}, these particles must travel through approximately 1½" of target material. The rms multiple scattering angle of these outgoing particles of 1.5 mrad. The amount of material in the rest of each spectrometer arm is to be compared to the target thickness. We note also, that for a kaon of momentum 3 Gev/c the average decay length is $c\gamma\tau$ = 400" or greater than three times the length of the spectrometer.

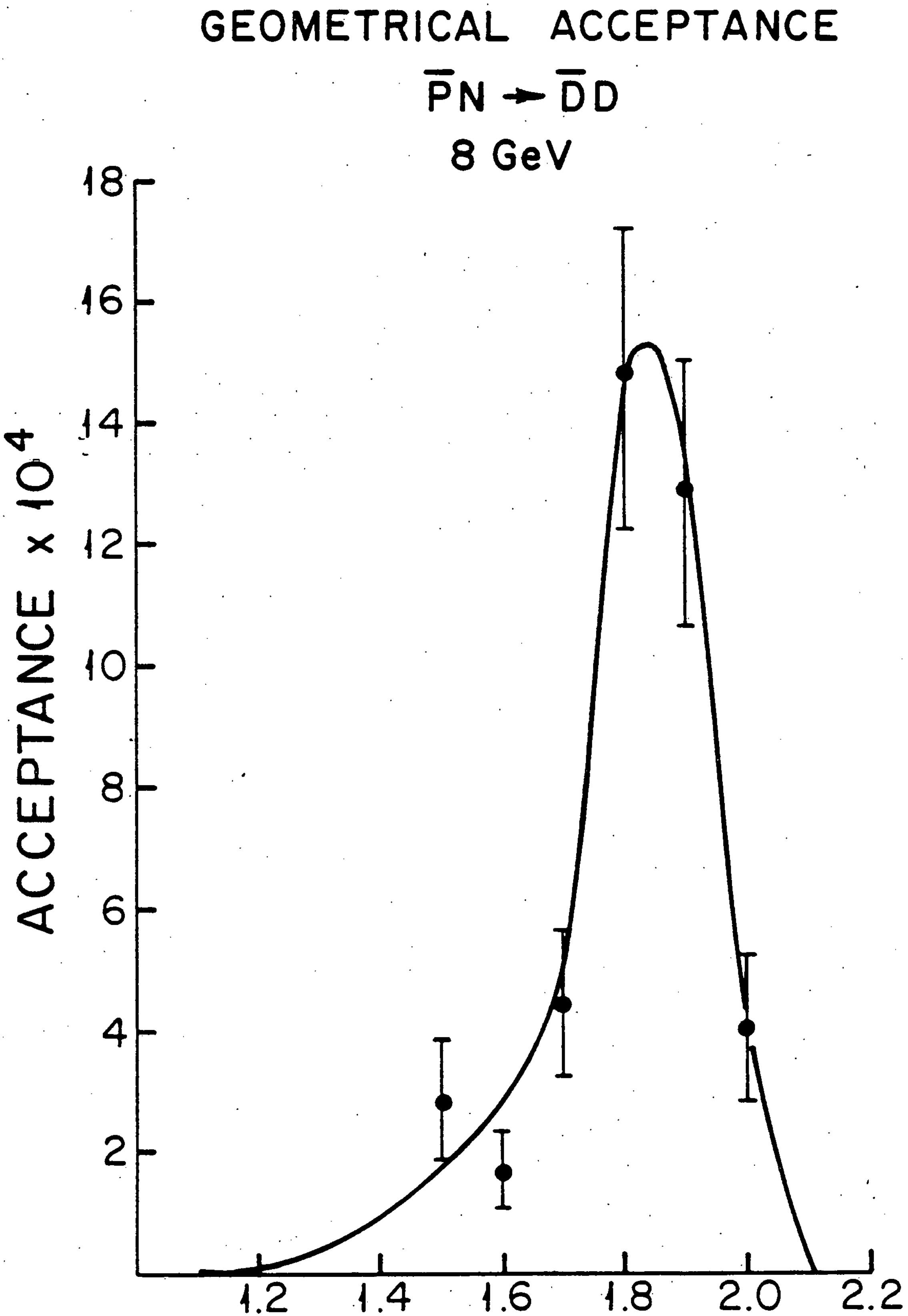

Figure V-4: Results of a Monte Carlo acceptance calculation for the process $\bar{P}N \rightarrow D\bar{D}$, where one of the D's is observed in the spectrometer via the decay $D \rightarrow K\pi$.

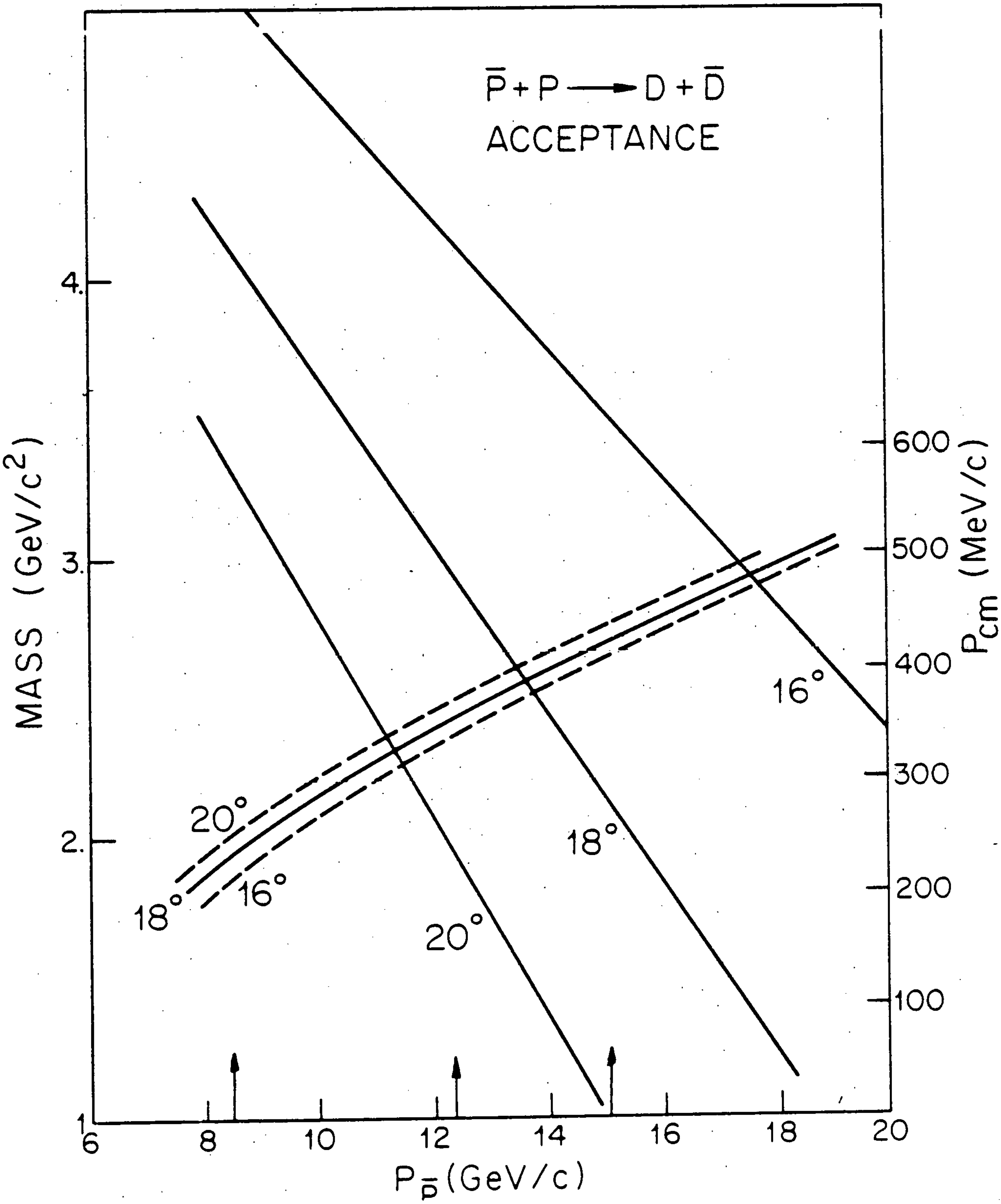

Figure V-5: Curved lines: D mass versus beam momentum for optimum acceptance. Straight lines: Longitudional momentum of accepted D's in the center of mass system.

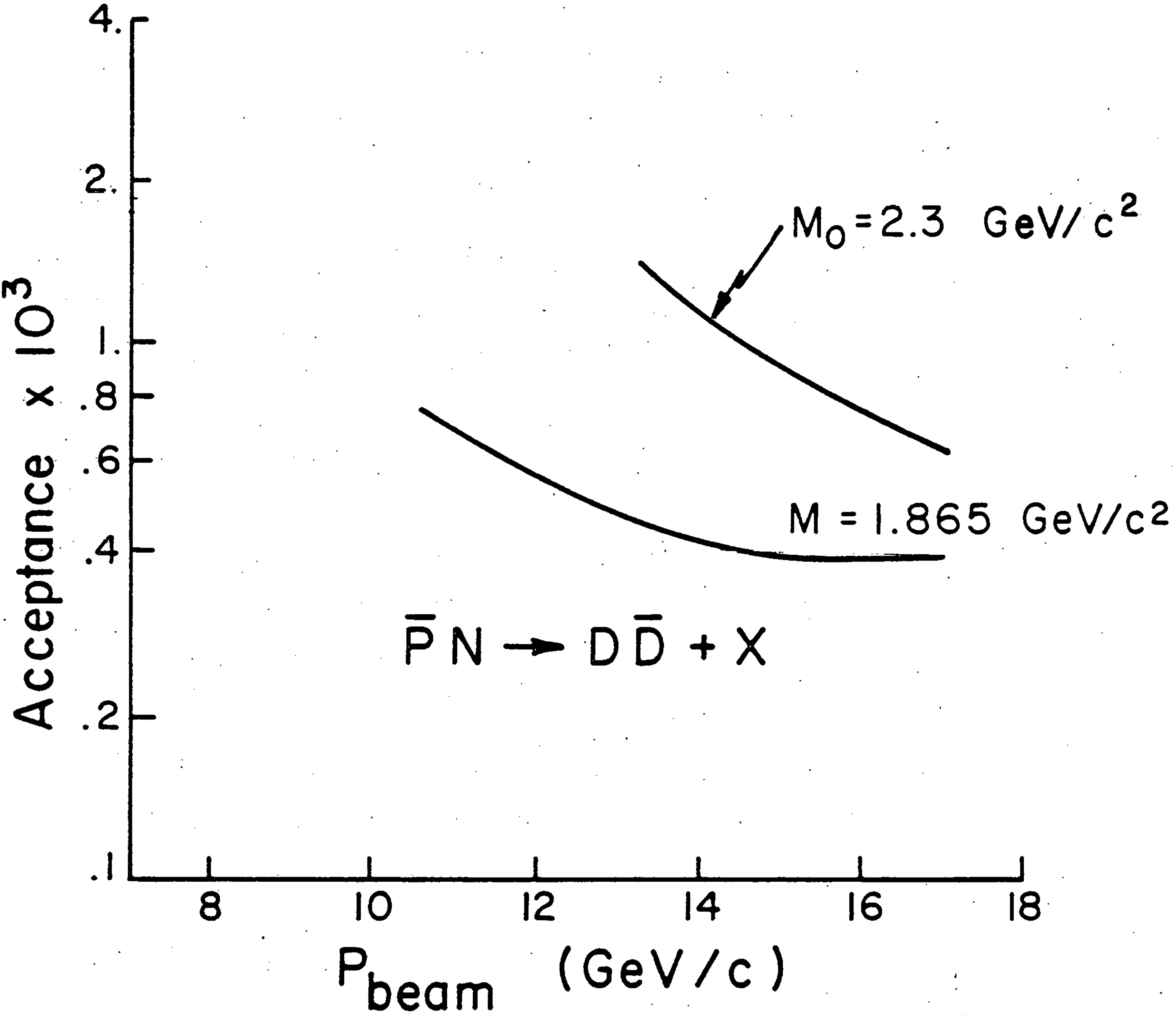

Figure V-6: Results of a Monte Carlo acceptance calculation for $\bar{P}N \rightarrow D\bar{D} + X$, where one of the D's is observed in the spectrometer via the decay $D \rightarrow K\pi$.

In addition to anti-protons, the B1 beam line provided an intense source of negatively charged pions. As mentioned, we hoped to use these pions to observe charm in associated production; eg.:

$$\pi^- N \rightarrow \bar{D}^0 + X$$

where X is a charmed baryon, if charm and baryon numbers are to be conserved. The pion-induced double-arm coincidence rate was, however, 200 to 300 events per 2 x 10^{12} protons incident on the primary target. This rate was far in excess of the capacity of the data acquisition system. We initially solved this problem by reducing the target length from 9 to 3 inches. However, with the discovery of the D^0 and an apparent 1^- excited state at SPEAR,[4] one of us[22] proposed the following scheme for reducing the large double arm trigger rate: Consider the decay:

$$D^{*-} \rightarrow \pi^- \bar{D}^0 \qquad (2)$$

Using the Q value ($Q \equiv \sum$ initial state masses $- \sum$ final state masses) for the observed decay:

$$D^{*0} \rightarrow \pi^0 + D^0$$

$$Q\ (D^{*0} \rightarrow \pi^0\ \bar{D}^0) \cong 2.0 \text{ to } 4.0 \text{ Mev}$$

and the linear relation between the 1^- mesons:

$$M\ (D^{*-}) - M(D^*) = -\ (M(K^*) - M(K^{*-})) = 4.1 \pm .6 \text{ MeV}$$

one can estimate that:

$$Q\ (D^{*-} \rightarrow \pi^- + \bar{D}^0) = 2.5 \text{ to } 4.5 \text{ MeV}$$

A similar value obtains if one assumes that:

$$M\ (D^{*-}) - M\ (D^{*}) = M\ (D^{-}) - M\ (D^{0}) \cong 11\ \text{MeV}$$

For Q sufficiently large, one would expect the radiative decays of the D^{*-} to be suppressed. Furthermore, one can show using isospin arguments that the decay $D^{*-} \rightarrow \pi^{0}\ D^{-}$ is suppressed relative to $D^{*-} \rightarrow \pi^{-}\ \bar{D}^{0}$. Best guess estimates indicate that the D^{*-} should decay according to equation (2) about 50% of the time.

These predictions seemed confirmed by the observation[5] at SPEAR of a peak near M = 2.01 GeV/c^2 in the missing mass spectrum of particles produced with the $D^{\mp}$. We hoped to reduce the large double arm trigger rate by observing the cascade pion from the D^{*-} decay. To this end we modified the spectrometer by the addition of a third arm, as shown in Figure V-7. A similar technique was used at SPEAR[6] where Q was measured to be 5.6 ± .5 MeV.

For small Q the pion and the D^0 laboratory momentum are related by

$$P_{\pi} = \frac{M_{\pi}}{M_{D}}\ P_{D}$$

Furthermore, since the kinematics of the spectrometer require that the momentum of the accepted D's lie along the + z axis, we expect the cascade pion to be moving not only slowly, but in the + z direction. In Figure V-8 we plot the production angle (θ) of the cascade pion versus its momentum for several values of Q. The maximum angle is fixed by an 11.5" hole in the shield plates of the spectrometer

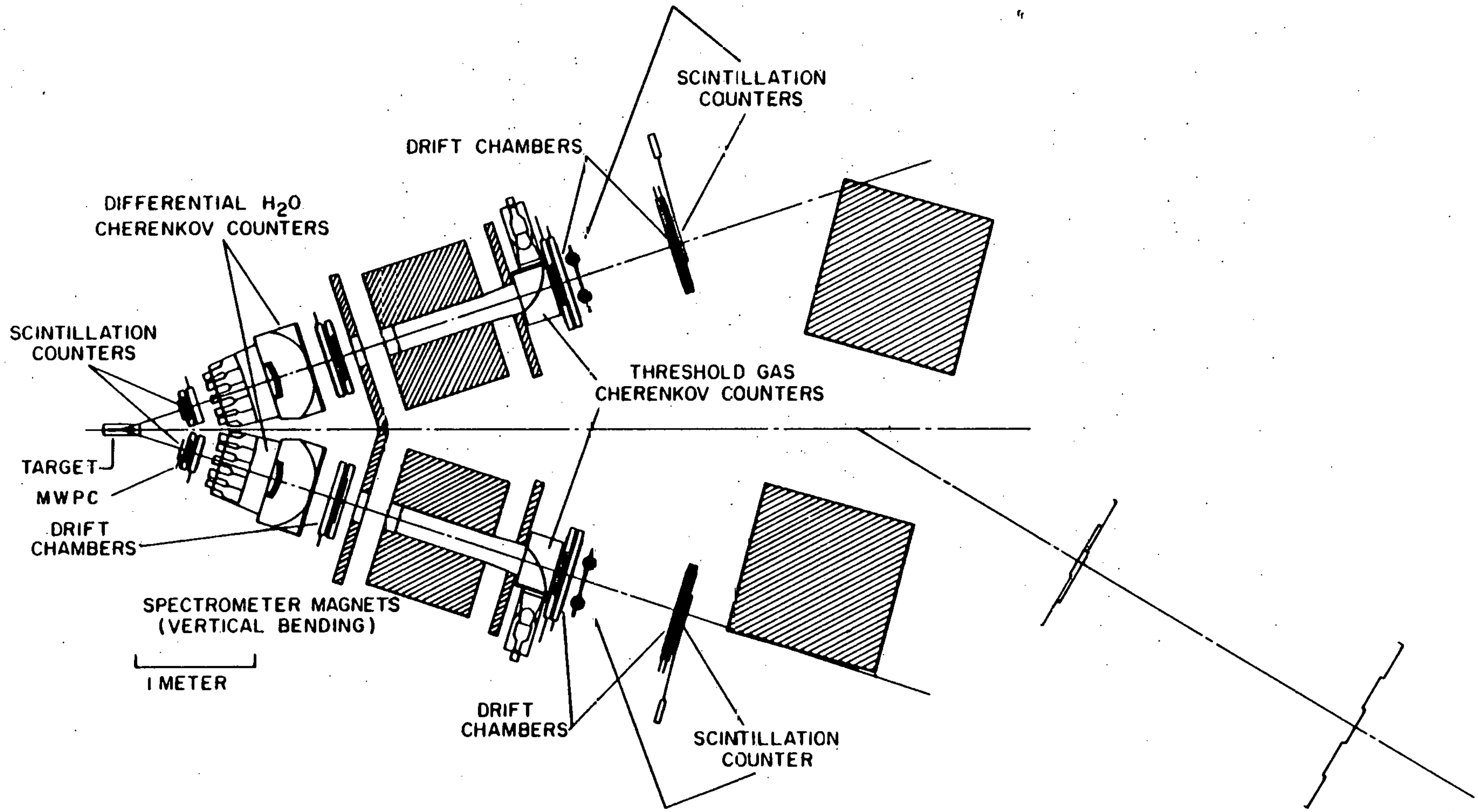

Figure V-7: Modified spectrometer for D^{*-} experiment.

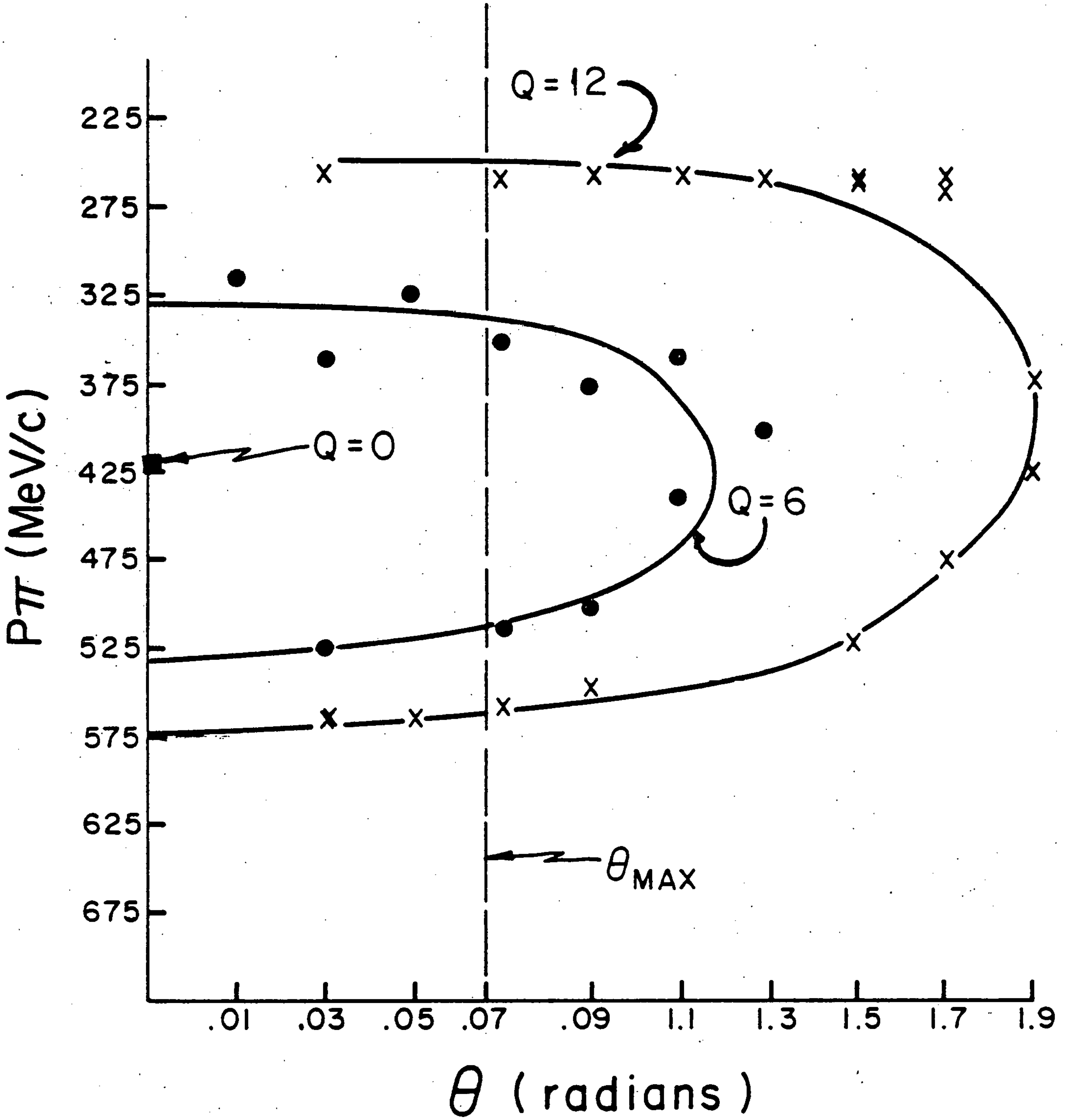

Figure V-8: Polar angle of cascade pion versus its momentum for three values of Q (Monte Carlo calculation). Lines are to guide the eye.

magnets 87" downstream of the target. We placed a 48 D48 dipole magnet with a 32" gap 240" downstream of the target. The field integral, $\int \bar{B} \cdot d\bar{\ell} \cong 272$ MeV/c, was sufficient to bend low momentum particles of interest out of the beam line. Two scintillation counter hodoscopes were used to measure the approximate angle and momentum of the low momentum particle.

The normal double arm trigger rate was suppressed by requiring a signal in both of the two third-arm hodoscopes. The trigger rate suppression achieved in this manner was a factor of 30, permitting operation at an intensity of 1.5×10^7 π^- on a 33 gm/cm^2 carbon target. The double arm data was analyzed in the usual manner, producing a K - π mass spectrum. The mass of the $K\pi\pi$ system was then calculated using the information from the third arm counters, thus determining Q. By demanding that this Q be consistent with the value measured at SPEAR (5.6 ± .5 MeV) the background was reduced by an additional factor of 5.

Essential to the success of this part of the experiment was a knowledge of the mass scale of the charmed baryons. Both of the experiments mentioned in the introduction indicated that the mass of the lowest lying charmed baryon was on the order of 2.3 GeV/c^2. If we then use that M_D is 1.865 GeV/c^2 and $Q \cong 0$, the required momentum of the incident pions is 10.5 Gev/c. Due to the target Fermi momentum, the estimates of the charmed baryon mass need only be accurate to about 300 MeV/c^2. The data accumulated during this phase of the experiment will be presented in Chapter IX.

VI. DRIFT CHAMBERS AND TRACK RECONSTRUCTION.

Twenty eight planes of drift chambers, divided equally between the two arms of the spectrometer, were used to measure particle trajectories. Six planes in each arm measured the trajectories in the horizontal plane. The remaining eight planes of drift chambers, four in front of the magnet and four after the magnet, measured the particle trajectories in the vertical (bending) plane.

Figure VI-1b is a cross-sectional view of a drift chamber of the type used in this experiment. The distance between adjacent sense wires is two inches and the separation between ground planes is one inch. Each sense wire is separated from its neighbor by a pair of drift wires. Two planes of wires, sharing a common ground plane and shifted with respect to each other by half a cell, comprise a complete drift chamber. In this configuration it is possible to determine whether the incoming particle passed to the right or left of a particular sense wire, since if a particle passes through the right half of one cell, it traverses the left half of the cell in the adjacent plane. The physical parameters of the drift chambers are summarized in Table VI-1.

Two points are noteworthy: 1) there are no field shaping wires; and 2) the drift and sense wires are paired rather than single. Cosmic ray tests of a prototype chamber with single (Figure VI-1a) rather than paired wires indicated that a constant drift velocity could be achieved throughout the drift space without the use of field shaping wires. This prototype chamber, however, suffered from poor efficiency near the drift wires. Doubling the drift wires enlarged the physical region near the drift wires for which the drift trajectories terminated on the sense wire. The superior efficiency

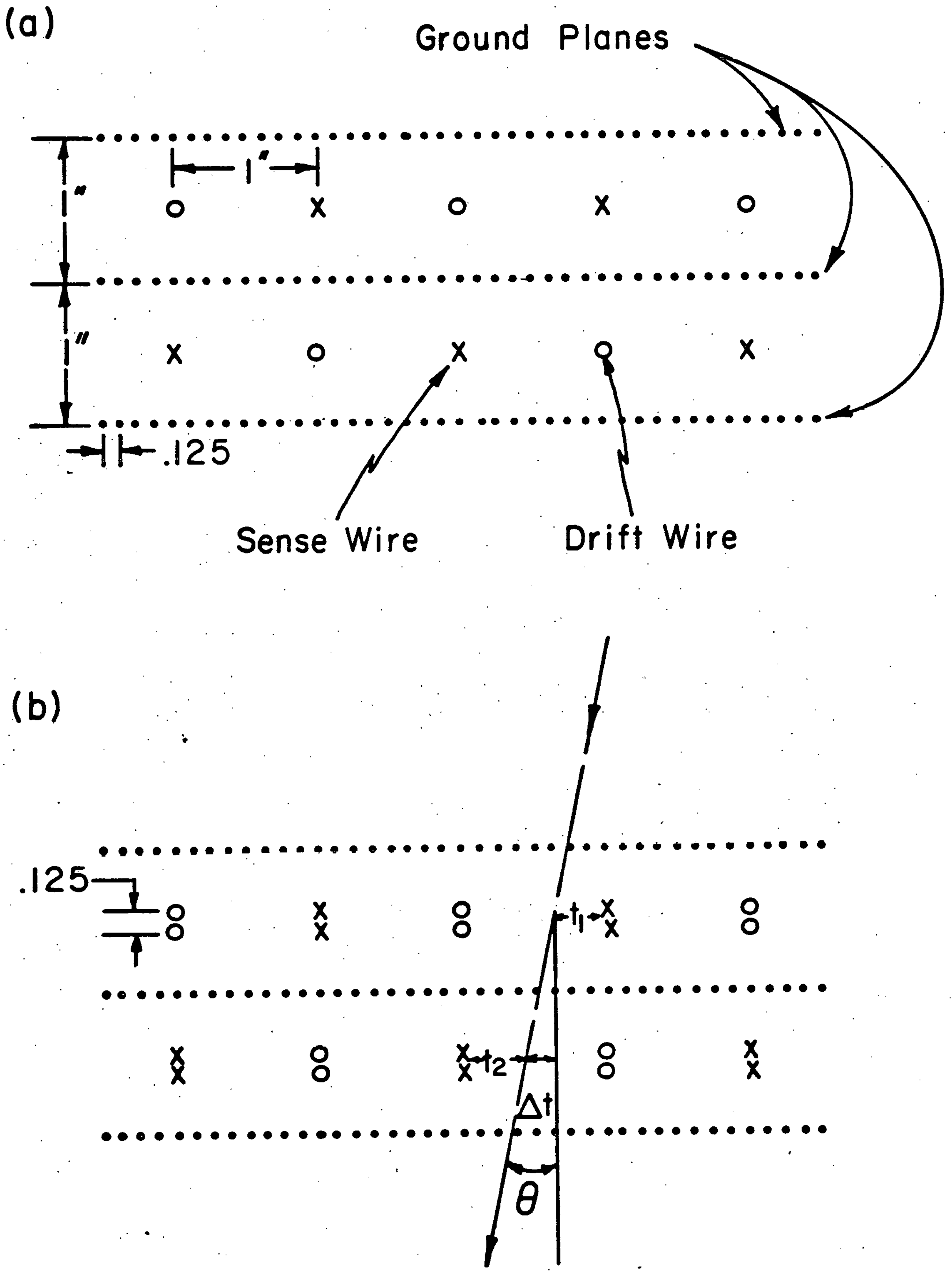

Figure VI-1: Two drift chamber designs. The design shown in (b) was used in the experiment.

TABLE VI-1: DRIFT CHAMBER PARAMETERS

GROUND PLANE WIRES:	.002"	Copper Beryllium
DRIFT WIRES:	.007"	Silver plated Copper Beryllium
SENSE WIRES:	.001"	Gold plated Tungsten

Z POSITION OF CHAMBERS FROM CENTER LINE OF SPECTROMETER MAGNETS (INCHES)

		RIGHT				LEFT			
	ACTIVE AREA	X		Y		X		Y	
		FRONT	BACK	FRONT	BACK	FRONT	BACK	FRONT	BACK
DC1	6"x6"	-87.39	-86.28	-84.37	-83.26	-87.56	-86.41	-84.53	-83.33
MWPC	6"x6"	-80.75		-81.25		-81.25		-81.75	
DC2	7"x14	-37.57	-33.50	-37.63	-35.54	-35.28	-34.20	-37.53	-36.40
DC3	10"x36"	+42.84	+43.83	+46.06	+47.02	+42.74	+43.73	+45.95	+46.96
DC4	16"x54"			+83.69	+86.38			+83.75	+86.37

of the double wire scheme is evident in Figure VI-2, which compares the two designs. These curves were made from data taken with an atmosphere of ethylene in the drift chamber. The drift velocity in ethylene is shown in Figure VI-3a, and is quite linear throughout the drift space.

Ethylene was chosen as the drift chamber gas for four reasons:

1) It had been successfully used by others[23].
2) It has excellent velocity saturation properties. i.e., the drift velocity is remarkably independent of the electric field over a wide range of values.
3) It does not have to be mixed.
4) Ethylene is inexpensive.

We therefore began this experiment with ethylene as the drift chamber gas.

With the sense wires at a potential of +3700 volts an Fe^{55} source produced signals of approximately 10 mV, measured before the amplifier. Since the principal X-ray from the decay of Fe^{55} has an energy of 5.9 kev, we expect that minimum ionizing particles would produce signals of approximately 1 mV, assuming the signals that trigger the amplifier correspond to the energy loss in 1/8" of gas. Each sense wire pair was connected to its own amplifier (Figure VI-4) and timing circuit (Figure VI-5). Raw signals from the drift chambers were amplified 200 times by a μA733 video amplifier used in a single ended mode. Resistors R_1 and R_2 determined the discriminator threshold according to $V_{min} = \frac{R_1}{R_1 + R_2} * V_{BB} \cong 150$ mV. At point A in the circuit a simple modification (not shown) permitted the amplified signals to be routed to one of

Figure VI-2: Efficiency curves for the two prototype chambers of Figure VI-1.

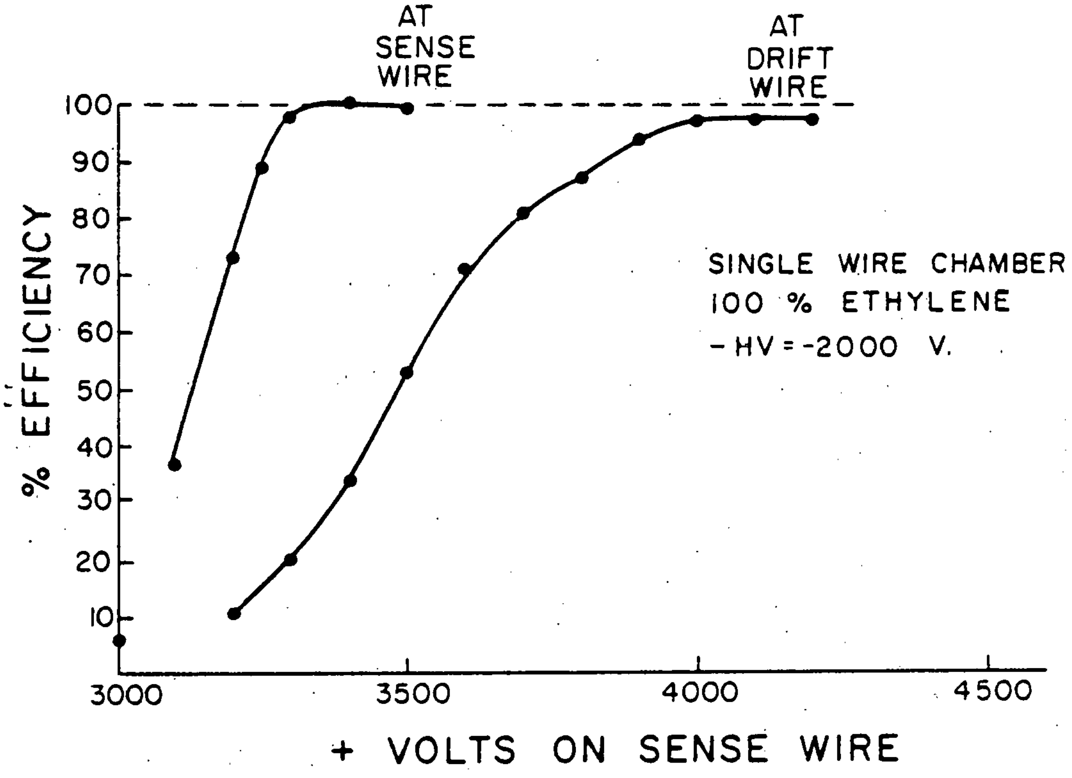

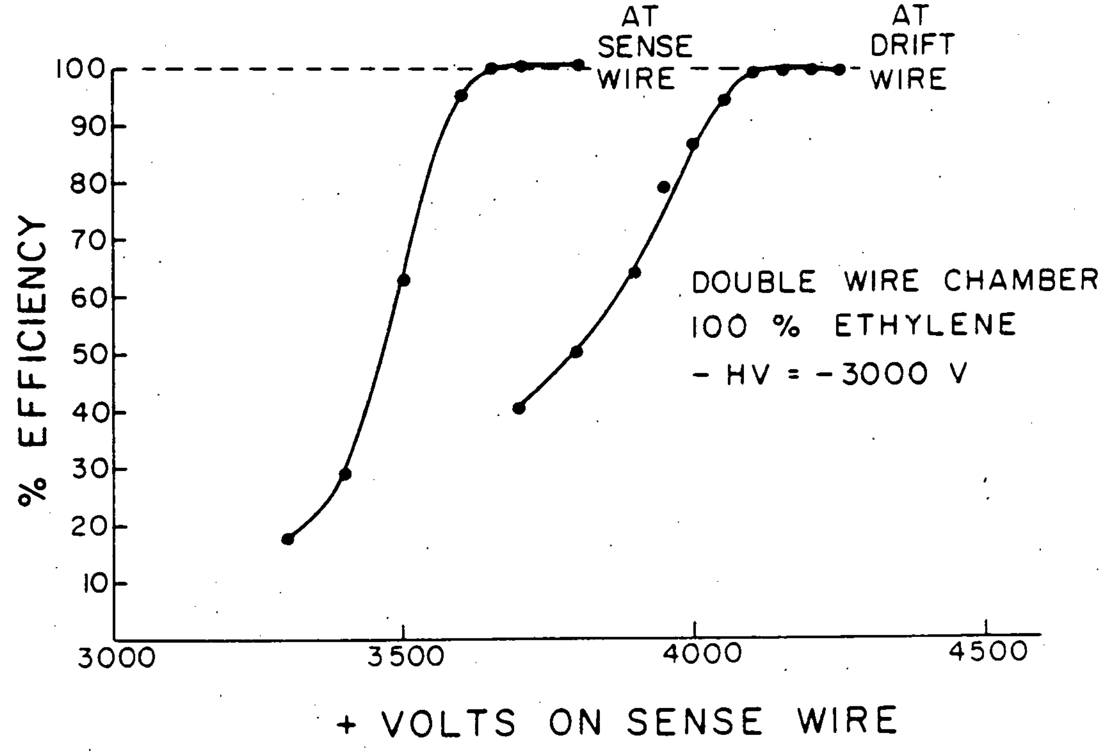

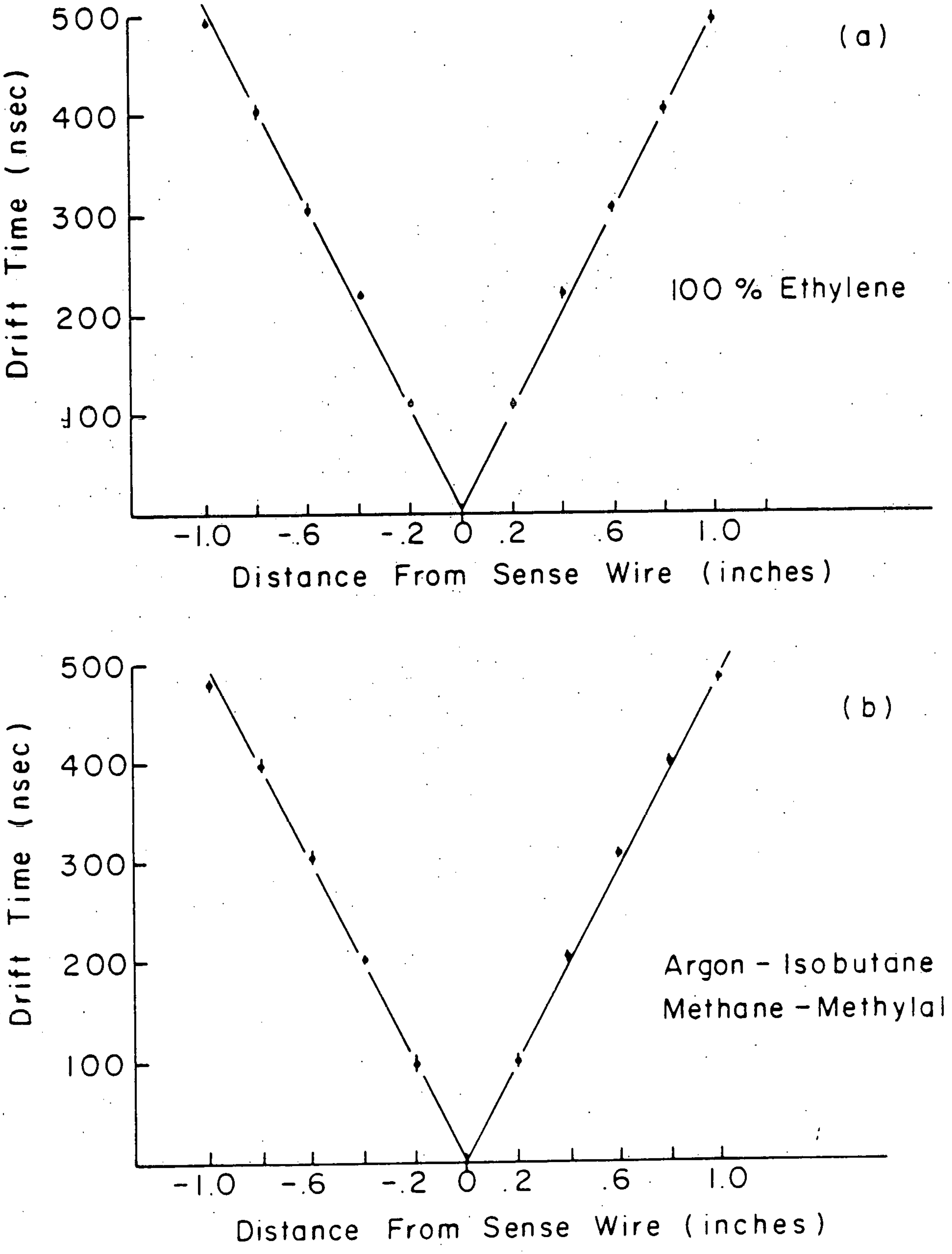

Figure VI-3: Drift time versus distance relationship for two drift chamber gases.

two line drivers (MC10101), each connected to its own time digitizer. This modification was only used in the front chambers where the particle flux was especially high.

A block diagram of the time digitizing circuit is shown in Figure VI-5. A 21 MHz master clock started by a fist NIM signal from the main trigger begins the timing sequence. A signal on a sense wire initiated a separate 24 MHz clock which was beat against the 21 MHz master clock in a vernier scheme (See Figure VI-6). A coincidence between the 21 MHz clock and the 24 MHz clock determines the drift time to a precision of:

$$\frac{24\text{ MHz} - 21\text{ MHz}}{21\text{ MHz} \times 24\text{ MHz}} = 6\text{ nsec or a drift distance of .012''}$$

The address (8 bits) and timing information (7 bits) of those channels containing information were readout by a CAMAC scanning module at a rate of 1.5 μsec per bit (The total dead time to readout all ADC's scalers, pattern bits and drift chambers into the fast buffer memory was approximately 3 msec.).

In Figure VI-1 let t_1 and t_2 be the measured time (corrected for electronics delays) for electrons to drift from the incident particle path to two sense wires on adjacent planes. The angle (θ) of the incoming particle is given by:

$$\sin\theta = (T_0 - t_1 - t_2)\ v/d$$

where T_0 is the maximum drift time, d is the separation between the sense wi planes and v is the drift velocity. The measurement error in θ due to the finite size of the timing bin is ~ 12 mrad.

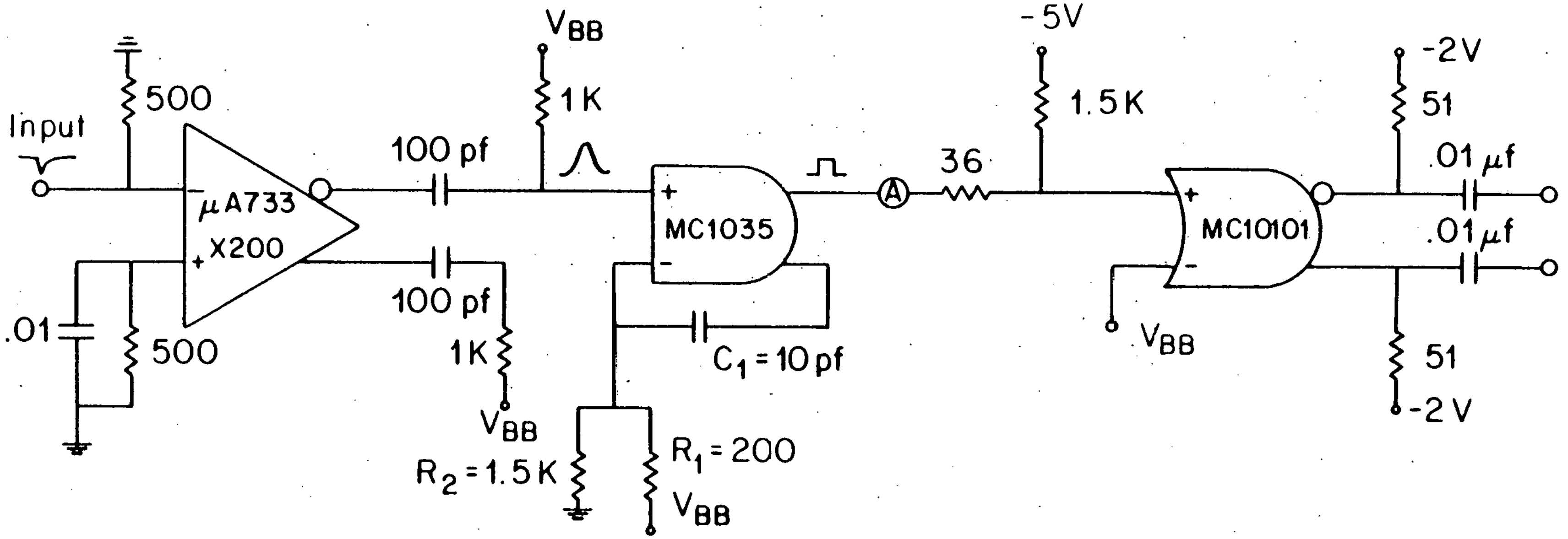

Figure VI-4: Pre-amplifier circuit (attached to chamber).

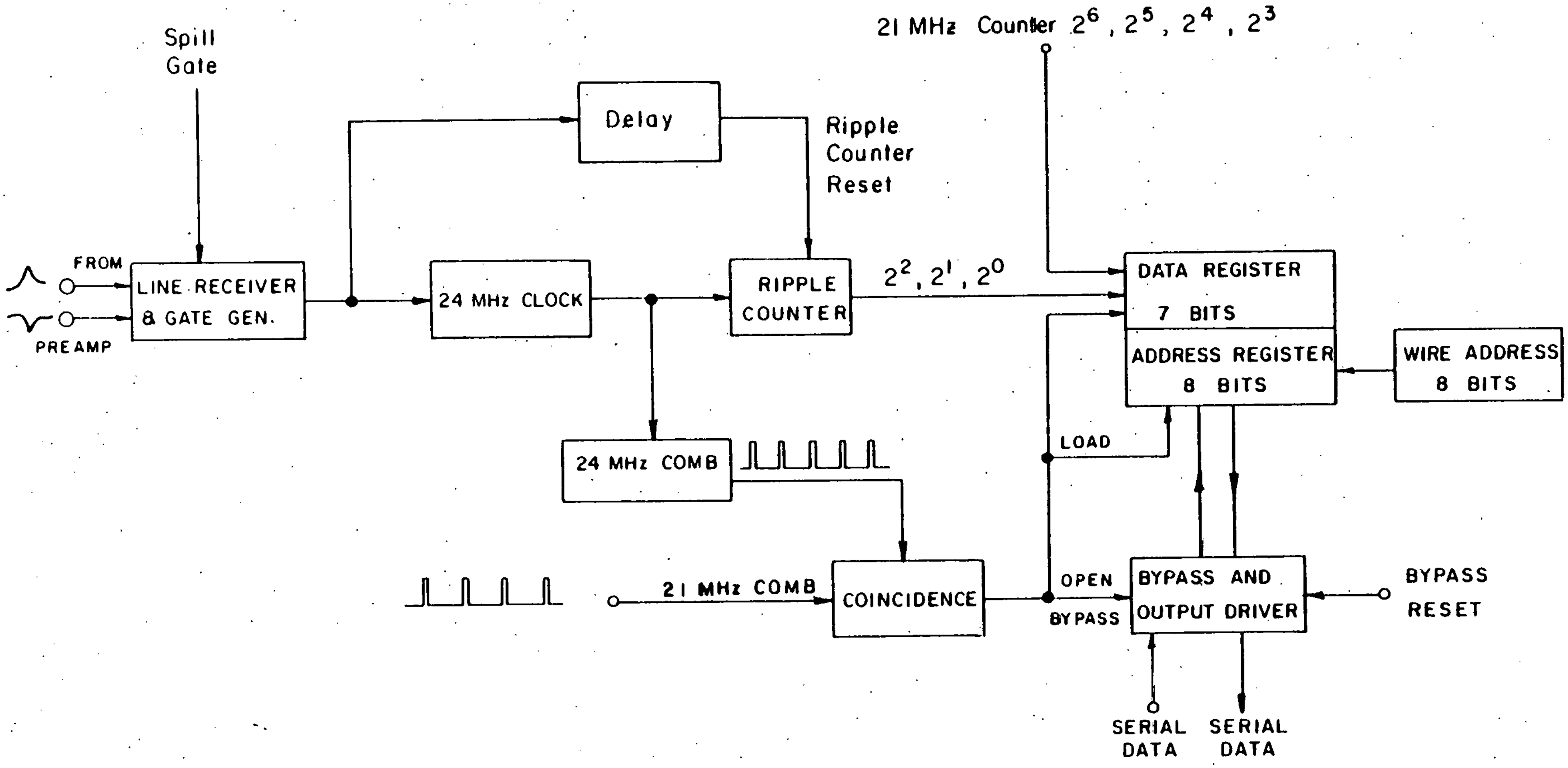

Figure VI-5: Block diagram of time digitizer.

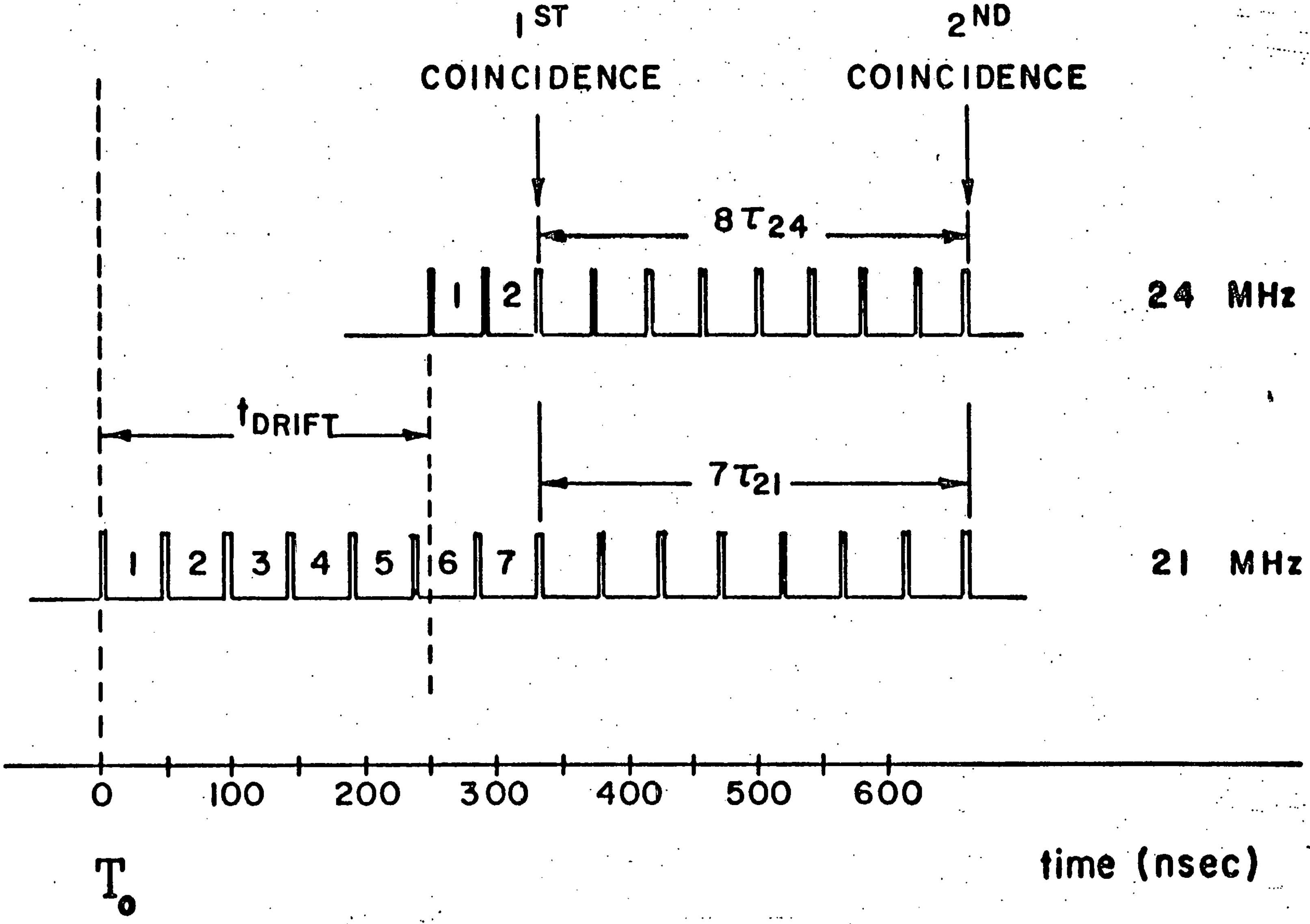

Figure VI-6: Schematic diagram of vernier timing system. Drift time for this example is

$\frac{5}{21\ \mathrm{MHz}}$ + 2*6 nsec = 250 nsec.

After the drift chambers had been installed the surveyed positions were checked with straight-through tracks (spectrometer magnets off). Figure VI-7 is a plot of the deviation of the position measured in one drift chamber from the trajectory calculated on the basis of information from the other chambers. The full width at half maximum is broadened (from the 12 mil intrinsic resolution) by multiple scattering in the water Cherenkov counter and the various scintillators.

Additional checks were made to insure that systematic effects were held to a minimum. In Figure VI-8 we plot the average deviation between the measured and calculated position of the particle trajectories as a function of the wire number for a typical chamber. The distance corresponding to one time bin is also indicated for purposes of comparison. As can be seen, the average deviations are all less than this fundamental distance.

As a further demonstration of the linearity of the drift velocity we plot in Figure VI-9 the average deviation as a function of the time bin summed over all the wires in one drift chamber. The data were produced assuming a constant drift velocity over the entire drift space. Here again, the deviations correspond to a fraction of one time bin.

After approximately 500 hours of use the efficiency of the drift chambers had fallen below acceptable limits. There was no apparent reason for the decrease in the efficiency, although a gradual rise in the chamber dark current had been observed.

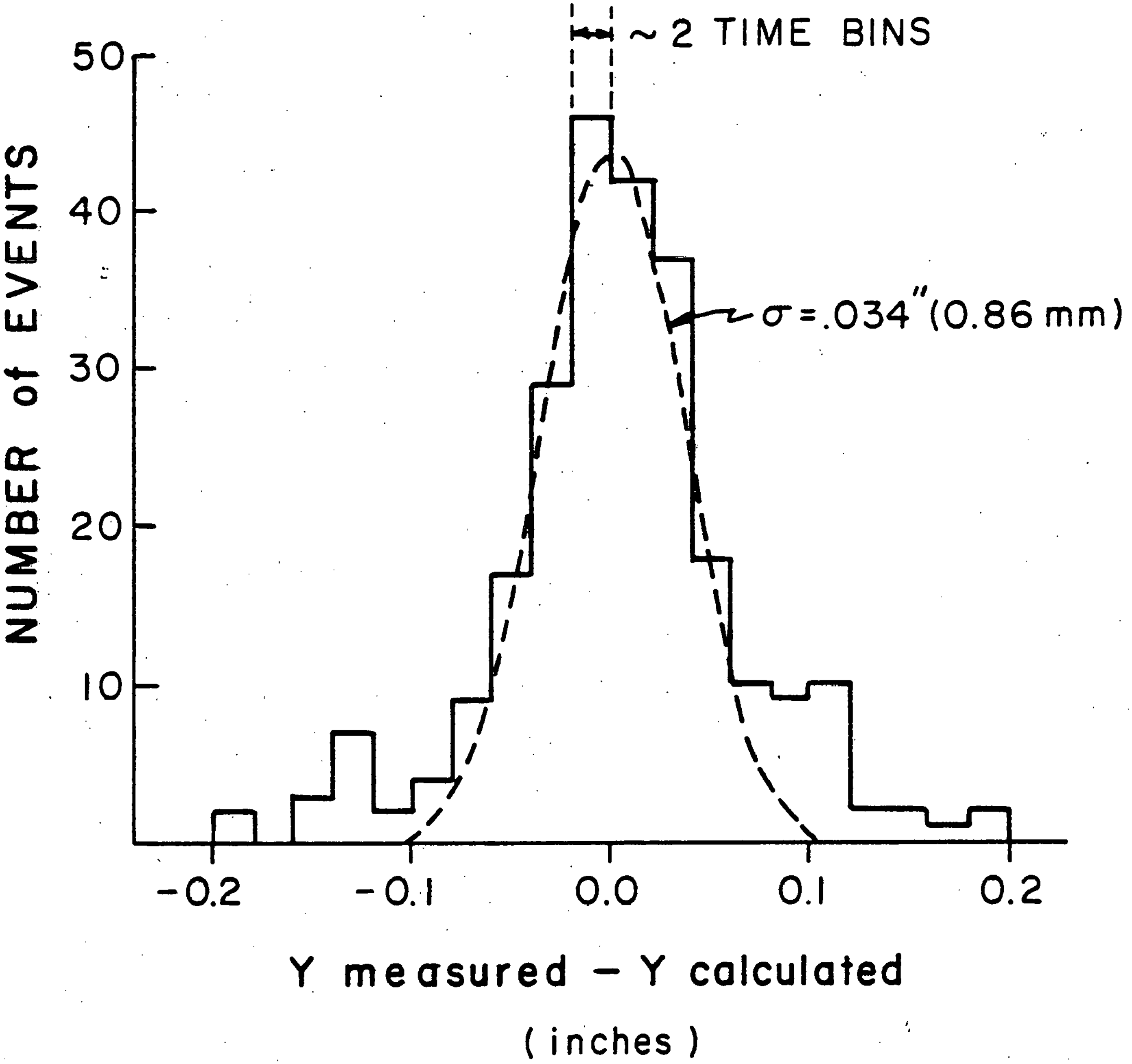

Figure VI-7: Deviation histogram obtained from straight through tracks.

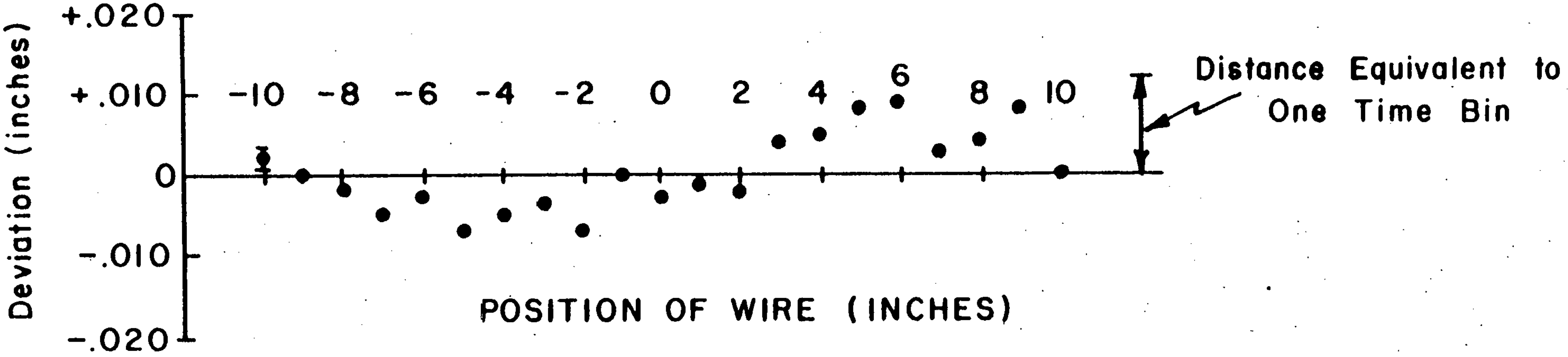

Figure VI-8: Average deviation as a function of wire position.

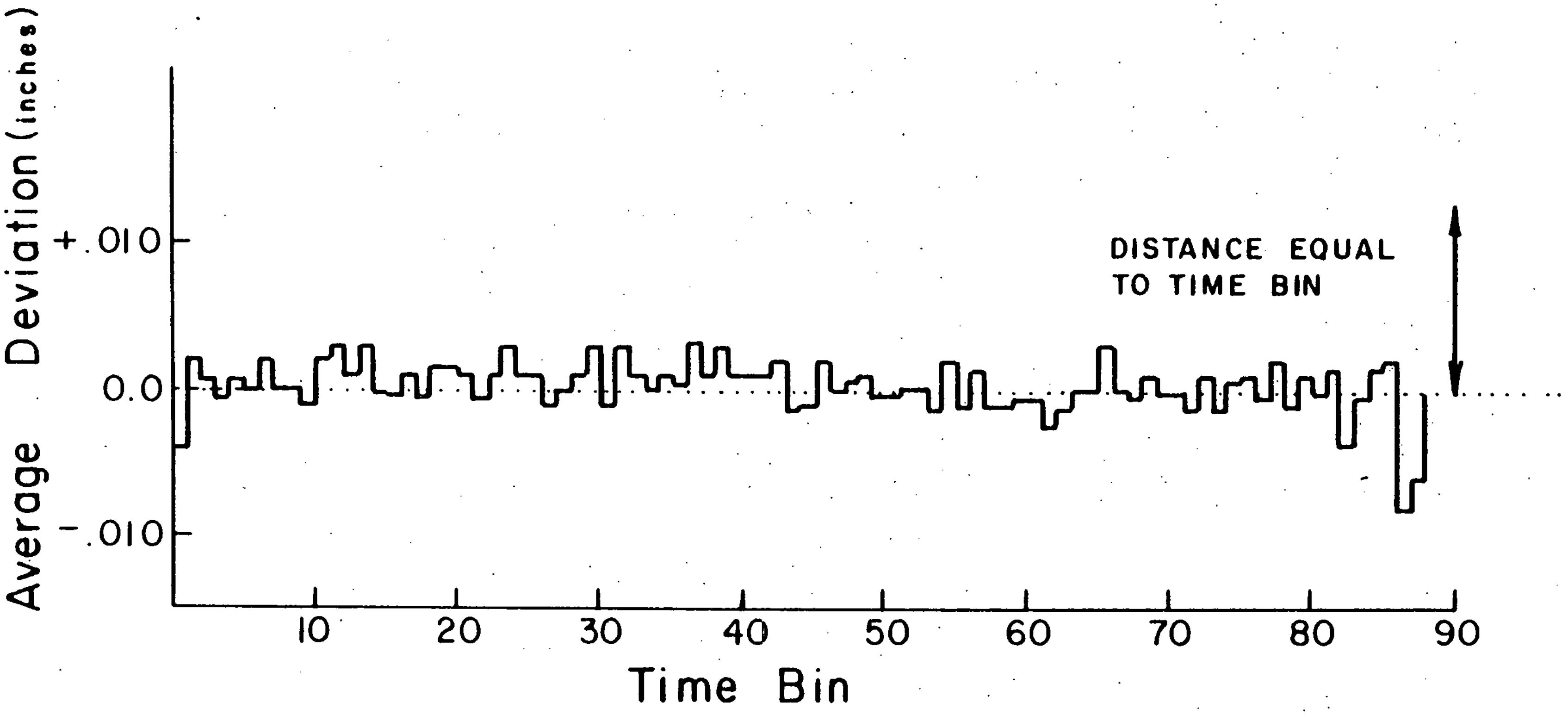

Figure VI-9: Average deviation as a function of time bin.

Microscopic examination of the drift chambers revealed that the ground wires were covered with fine black filaments while small clear crystals had formed on the drift wires. The sense wires were relatively clean. It was supposed that organic radicals formed in the ionization of the ethylene gas migrated to the ground planes and drift wires where polymerization took place. The deposits on the wires then acted as electron sources increasing the noise and dark current in the chambers. A similar observation was made by another group[24] in laboratory tests using a radioactive source. A 15 min exposure to a collimated 2 mcurie Ruthenium source (~ 10^7 ionizing particles/sec/cm^2 on the chamber) was sufficient to reduce the efficiency of the test chamber from 100% to zero. The deposits were removed by washing the chambers once each with amyl acetate, methyl-ethyl-keytone and Freon 112.

The remainder of the experiment was carried out with a drift chamber gas consisting of argon (80%), methane (8%), isobutane (10%) and methylal (2%). This combination of gases had been successfully tested at CERN.[25] The distance versus time relationship for this drift chamber gas is shown in Figure VI-3b and is again linear throughout the drift region.

This new drift chamber gas has, of course, the disadvantage of requiring mixing. An argon methane (90%-10%; so called P-10) gas mixture was bubbled through methylal at $0^{\circ}C$ and then mixed with isobutane. Gas flow was measured with Matheson type 600 flow meters on the basis of calibration curves supplied by the manufacturer. Care was taken to avoid contamination of the methylal by the isobutane (isobutane liquifies at $3^{\circ}C$). After 2000 hours of use with this gas no decrease in efficiency in the chambers has been observed.

The track reconstruction program began by searching the drift chambers behind the magnet for possible tracks in the bending plane. A track* found in chamber 3 was projected onto chamber 4, with the appropriate uncertainty determined by the error in measurement of the angle of incidence times the separation between the chambers. The program then searched within this error window for possible tracks in chamber 4 with the same angle of incidence. Finding such a track the particle trajectory behind the magnet was calculated and projected back to the center line of the magnet. If no track was found, or if the information was ambigious, the event was rejected. Those points in chambers 1 and 2 which lay near a line connecting the center of the target with the point at the center line of the magnet were used to reconstruct the particle trajectories through the front chambers. Track finding in the non-bending plane was completely analogous. Positions behind the magnet were corrected for horizontal focusing due to the logitudinal component of the fringe field.

The track reconstruction efficiency was poor; only about 10% of all real events were reconstructed. There were two reasons for this poor efficiency. First, the naive solution to the right-left ambiguity is incorrect for particles incident at large angles, since they need not pass through overlapping drift spaces. Indeed, at the extreme ends of chamber 4 this solution is usually wrong. Hence for each pair of points in a chamber there are four possible tracks. It frequently happens that two of these tracks are consistent (within

---

*For the purposes of discussion a track in a <u>single</u> chamber is defined by signals on two sense wires in adjacent planes separated by no more than 1".

errors) with the track in chamber 3, making track reconstruction impossible. Similarly, if one of the four signals is missing the event is, in general, unreconstructable.

The second reason for the poor reconstruction efficiency was the high flux of particles through chambers 1 and 2. Because of the comparatively long drift space, any particle which passed through the spectrometer within 500 nsec of the main trigger appeared in the drift chamber information, confusing the data from the particles actually involved in the event. It was often impossible to unambiguously sort out the information in the front chambers.

We partially solved this second problem by replacing the front drift chambers with multiwire proportional chambers (MWPC). These chambers had a much better timing resolution (~ 100 nsec) but slightly worse spatial resolution (The wire spacing was 1/8" corresponding to an intrinsic resolution of 35 mils). The details of the design of these chambers and the associated electronics has been described elsewhere.[25a] We note here, however, that these chambers were operated using the same gas mixture as the drift chambers.

The best solution to the first problem was to install more chambers behind the magnet, which was at the time impossible. As a stop-gap measure we added scintillation counters directly behind the magnet (labelled S2 in Figure V-1) to reduce the accidental trigger rate. With these improvements a factor of about two was gained in the reconstruction efficiency.

VII. CHERENKOV COUNTERS AND THRESHOLD DETECTORS

A. A Broad Band Focusing Cherenkov Counter

The compact size of the spectrometer meant that little space was available for Cherenkov counters. The Cherenkov counters had, therefore, to be compact, as well as efficient over a wide range of phase space. To properly separate kaons from protons the detector had to measure velocities as low as $\beta = .95$, up to the maximum $\beta = 1$. Additionally, the path of particles through the Cherenkov counter could be displaced as much as 4" from the center line of the spectrometer arm or at angles as large as .1 rad. The Cherenkov counter had to be equally efficient for these off-axis particles.

One of us[20] proposed a Cherenkov counter (Figure VII-1) with essentially these characteristics. The Cherenkov medium is water ($n \cong 1.33$) contained in a lucite (Rohm and Haas UVT-II) meniscus one and one-half inches thick. The curved surface of the radiator (radius = 37.125") compensated for off axis particles. A spherical nickel-plated mirror of radius 17.0" focused the Cherenkov light onto the phototube mask shown in Figure VII-1b. We designed the mirror as a compromise between a shape that could be easily fabricated and the desire to reduce the effects of coma.

Behind each of the eight petals in the phototube mask was an aluminized mylar light guide which channeled incident light onto the photocathode of an RCA 8854 photomultiplier tube. Zener diodes in the base circuits prevented deterioration of the signals due to the high rate forward of the spectrometer magnets. Individual pulse height spectra were fitted with Poisson distributions.

Figure VII-1: (a) Cross-sectional view of water Cherenkov counter; (b) Phototube mask.

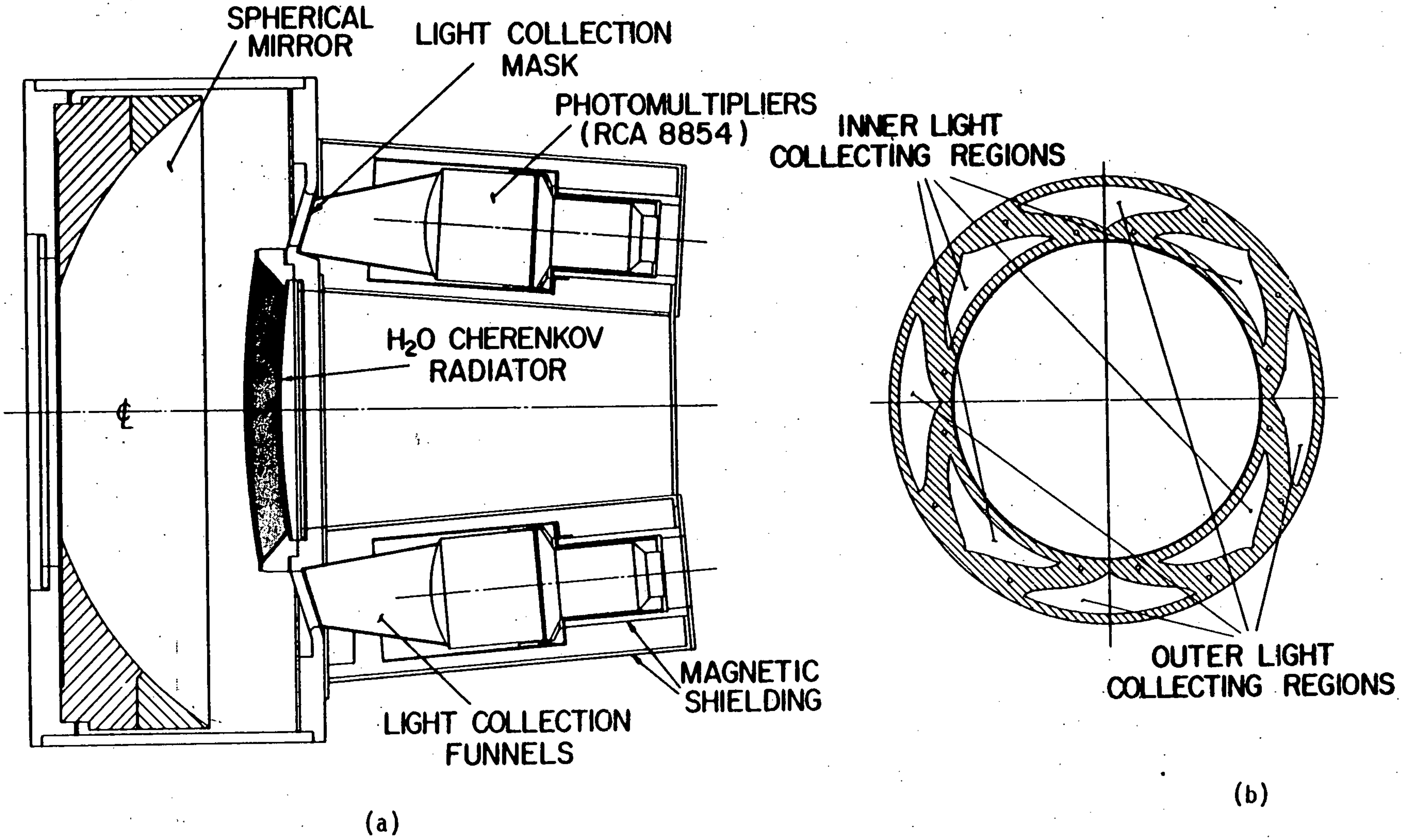

We define a parameter Δ equal to

$$\Delta = \frac{N_o - N_I}{N_o + N_I}$$

where $N_o(N_I)$ is the sum of the number of photoelectrons in the outer (inner) four phototubes. Given the shape of the curve outlining each petal, it is possible to show (Appendix 1) that the radius (r) of the Cherenkov ring at the phototube mask is given by

$$r = C_1 + C_2 \sin^{-1}\Delta$$

where C_1 and C_2 are constants. Monte Carlo studies indicate that $\bar{\Delta}$ is relatively stable for particles travelling parallel to, but displaced from, the center line of the pattern.

Figure VII-2 is an example of the π - p separation attained with this Cherenkov counter. The two histograms show the distribution of Δ for particles with momenta between 3.5 Gev/c and 4.6 Gev/c. Those particles included in Figure VII-2a also produced signals in the threshold counter and are considered pions. The particles corresponding to the data plotted in Figure VIII-2b were not associated with signals in the threshold counter and are mostly protons. The separation between the proton peak and the pion peak is approximately 0.40. Both have a width of approximately σ = .25. There is no obvious kaon signal.

Particles detected by the water Cherenkov counter must have a minimum momentum (P_{min}) given roughly by:

$$P_{min}\ (\text{Gev/c}) = 3 * M\ (\text{Gev/c}^2) \qquad (1)$$

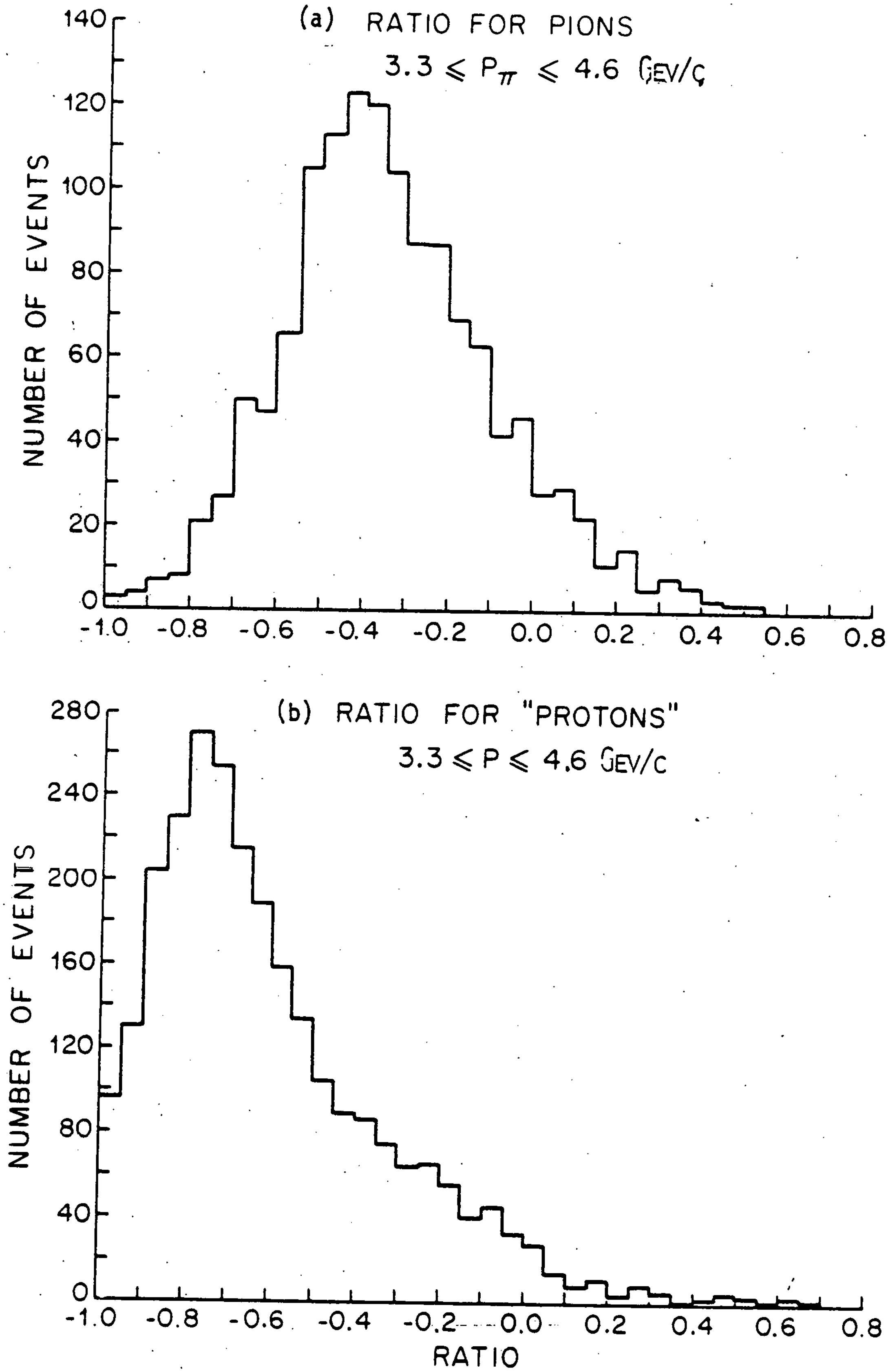

Figure VII-2: Typical π/P separation in H_2O Cherenkov.

where M is the mass of the particle. With the approximation that $\beta = 1 - 1/2*M^2/p^2$ one can demonstrate (Appendix 1) that

$$\Delta \cong \sin\,(K_1 + K_2*M^2/p^2\,) \qquad (2)$$

where K_1 and K_2 are constants independent of the particle type. In Figure VII-3 we trace the value of Δ (obtained from Monte Carlo calculations) as a function of momentum for pions, kaons and protons. Equation (2) is consistent with these curves to ± 5%. We observe that at the onset of the threshold counter that kaons are separated from pions by only one standard deviation. The absence of a clear kaon signal in Figure VII-2 can now be understood. Any kaon signal would be dwarfed by pions which are produced about 100 times more copiously at these angles and energies.

All information from the Cherenkov counter is, of course, lost if there is more than one particle per arm per event. In Figure VII-4 we plot the total number of photoelectrons collected in the inner and outer rings ($N_O + N_I$). The single particle peak is centered near 102 (arbitrary units) and is accompanied by a long tail towards higher sums due to two or more particles. The solid line represents the sum of a constant plus two Gaussian distributions (7 free parameters) fitted to the data. The ratio information was used only when the number of photoelectrons fell within $\pm\,2\sigma$ of the single particle peak. To be unambiguously identified as a kaon, the measured ratio (Δ) had to fall with roughly $\pm\,1\sigma$ of the value predicted by equation (2) (or alternately Figure VII-3). If it also happened that the measured ratio fell within $\pm\,1\sigma$ of the pion (or proton) curves, the particle was also labelled as a possible pion (or proton). Hence, one event might appear in several mass plots.

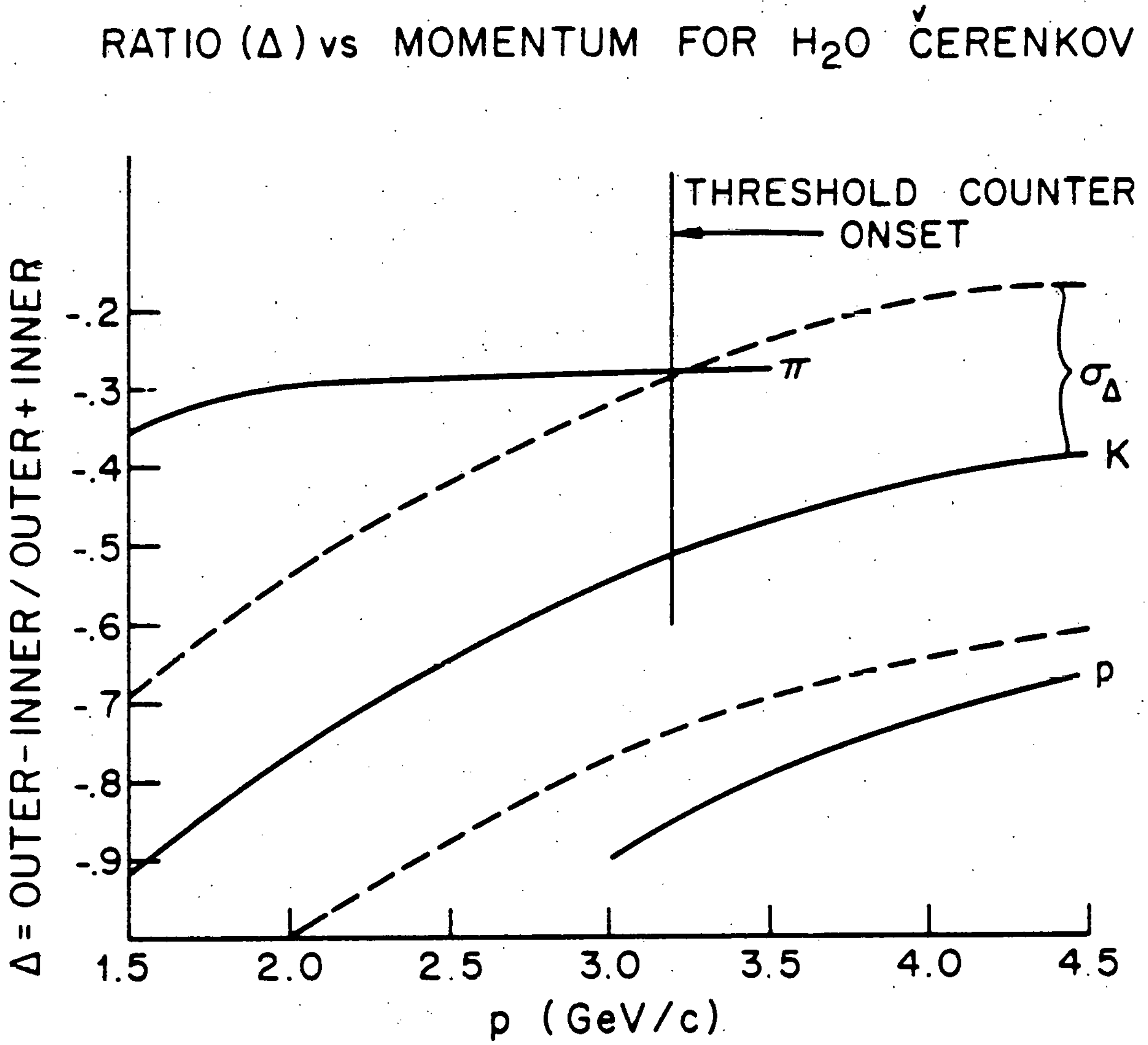

Figure VII-3: Value of Δ for pions, kaons and protons as a function of momentum (Monte Carlo calcualtion). Typical width of ratio distribution is indicated for kaons. Similar results apply to proton and pion curves.

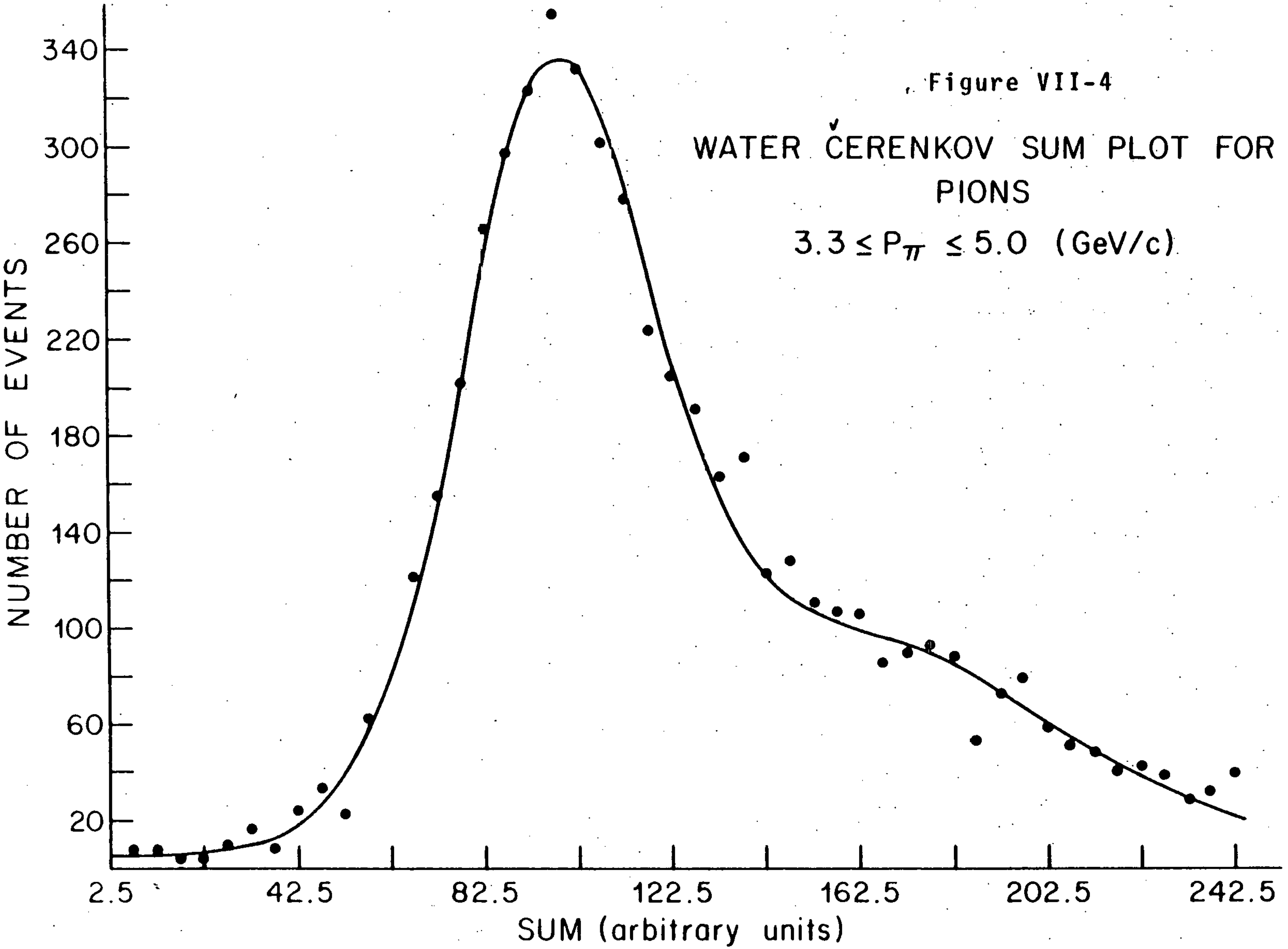
Figure VII-4
WATER ČERENKOV SUM PLOT FOR PIONS
$3.3 \leq P_{\pi} \leq 5.0$ (GeV/c)
NUMBER OF EVENTS
340
300
260
220
180
140
100
60
20
2.5
42.5
82.5
122.5
162.5
202.5
242.5
SUM (arbitrary units)

As described, the threshold velocity for this detector was $\beta = .95$, corresponding to a momentum three times the mass of the incident particle. Since the low momentum cutoff imposed by the geometry of the spectrometer was $p \geq 1.25$ GeV/c (see Figure VIII-1) the water Cherenkov counter could detect essentially all pions and most of the kaons accepted by the spectrometer. On the other hand, low momentum protons ($p \leq 3$ GeV/c) were invisible to the Cherenkov counter. In Figure VII-5 we plot the number of photoelectrons in the outer ring (N_0) for particles with momenta between 2.2 and 2.5 GeV/c. The peak at zero corresponds to protons while the peak centered at ~36 is produced by pions. Kaons occupy the region in between. Any particle of momentum less than 3.1 GeV/c (1.7 GeV/c) which did not produce light in the outer ring (SUMOUT $\leq$ 14) was at least considered a proton (kaon). If the sum and ratio criteria for a kaon or pion were also met, then the particle was also labelled as one of these.

All particle identification cuts were graded as a function of momentum so as not to introduce any discontinuities in the mass spectra. In Figure VII-6 we plot the maximum allowed deviation of the measured ratio from the average value as a function of momentum for kaons, pions and protons. We note that above 3 GeV/c, where the threshold counter is used to identify pions, the ratio cuts on kaons become less restrictive.

B. The Threshold Counters

Because the K-π separation in the water counter was poor above 3 Gev/c a threshold Cherenkov counter was installed in the magnet gap. This counter (Figure VII-7) was filled with Freon 12 at stmospheric pressure and was sensitive to pions with momentum $p \geq$ GeV/c ($\beta \geq .9989$). The entrance and exit windows were constructed of 10 layers of .25 mil aluminized mylar, providing

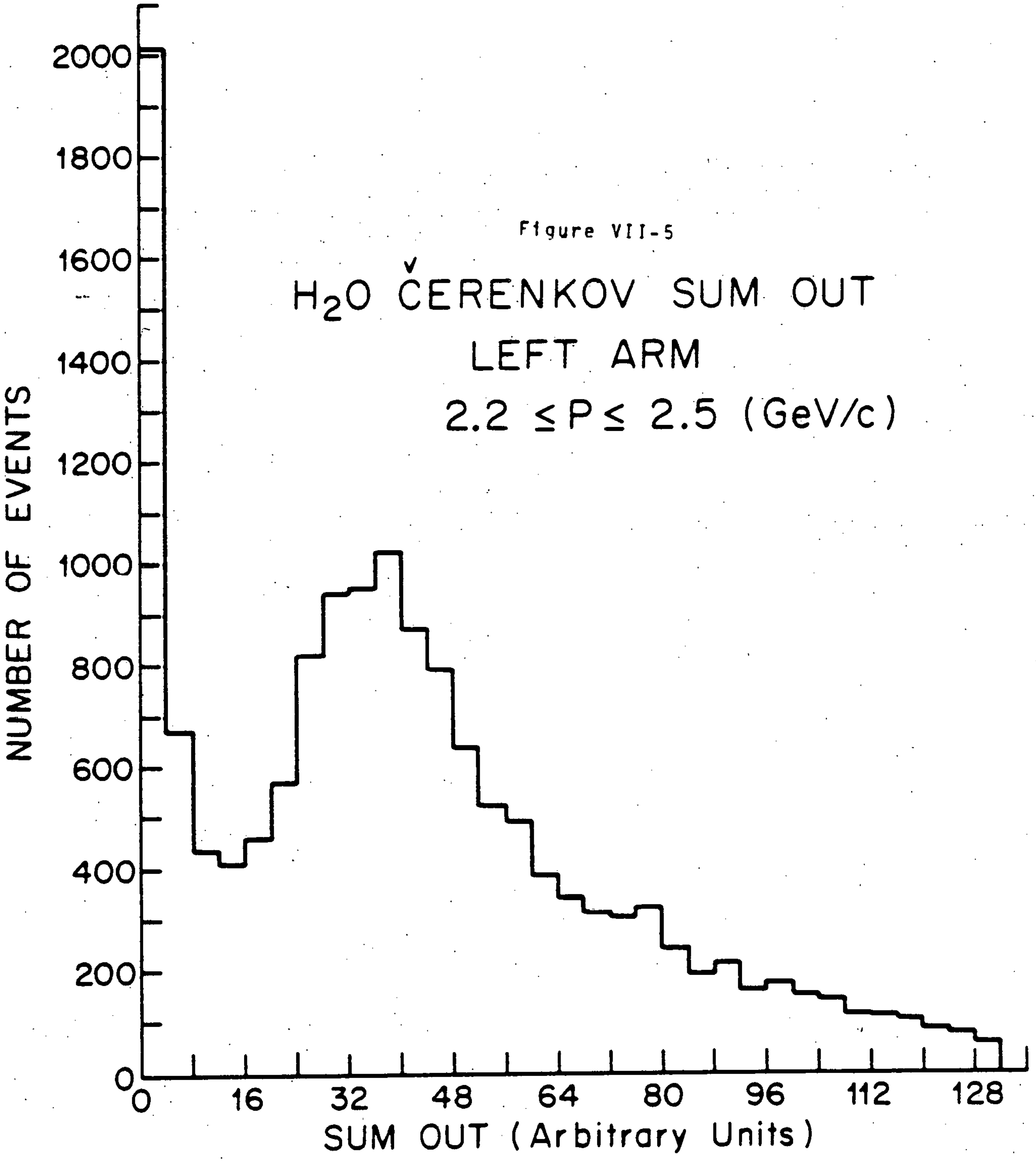

Figure VII-5

H_2O ČERENKOV SUM OUT
LEFT ARM
$2.2 \leq P \leq 2.5$ (GeV/c)

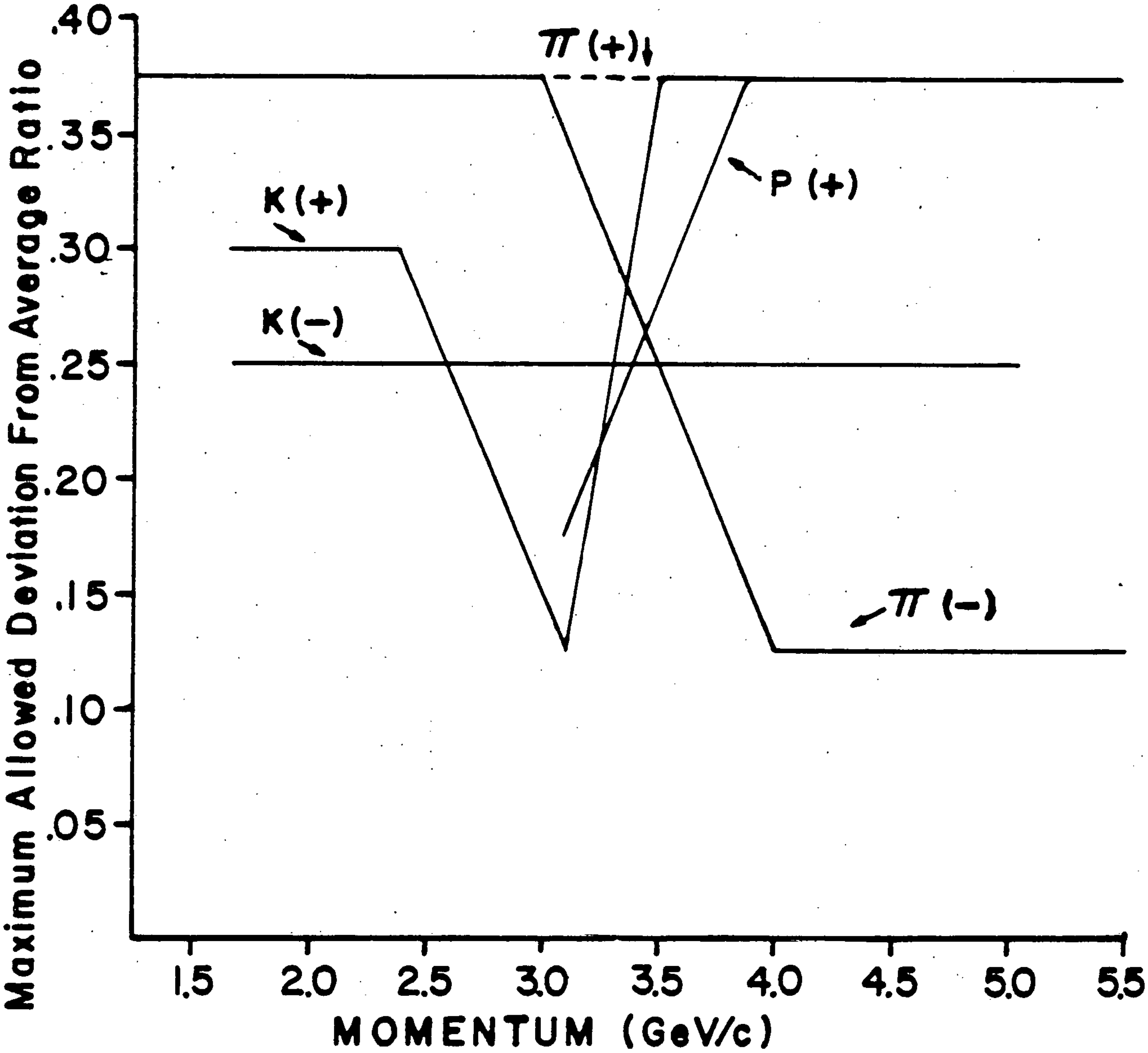

Figure VII-6: Ratio cuts as a function of momentum. '+' sign refers to positive deviation; '-' sign refers to negative deviation. HWHM of pion distribution is σ=0.25. Minimum allowed proton ratio is $\Delta \geq -1.1$ independent of momentum.

a sealed, light-tight environment for the Cherenkov gas. These thin windows also kept multiple scattering to a minimum. Two spherical front-surface mirrors reflected the Cherenkov light onto two RCA 8854 phototubes. The mirrors were made of aluminized 1/8" thick black plexiglass. This material minimized multiple scattering and absorbed any Cherenkov radiation produced in the mirror itself. Two layers of μ-metal shields and a third of cast iron protected the phototubes from stray magnetic fields. We observed no decrease in the phototube efficiency as a function of the magnet current or polarity.

To insure that the counter was efficient throughout the entire volume of the magnet gap we compared the number of identified pions with the total number of charged particles. These numbers (Fig. VII-8) are plotted as a function of the horizontal positions of the particles as they pass through the center of the magnet gap. We note that the pion distribution has the same shape as the total charged particle distribution. We conclude there are no regions where the counter is seriously inefficient. Above 3 GeV/c particles identified as pions had not only to satisfy the water counter criteria, but also had to produce signals in the threshold counter.

C. Muon Identification

Muons were identified by their ability to penetrate 8 feet of iron placed at the end of each spectrometer arm. The minimum muon energy required to penetrate this distance is 2.5 GeV. Trajectories calculated in the drift chambers were projected through the muon hodoscope counters S_4 and S_5 (Figure V-1). A particle identified as a muon had to produce signals in the scintillation counters whose

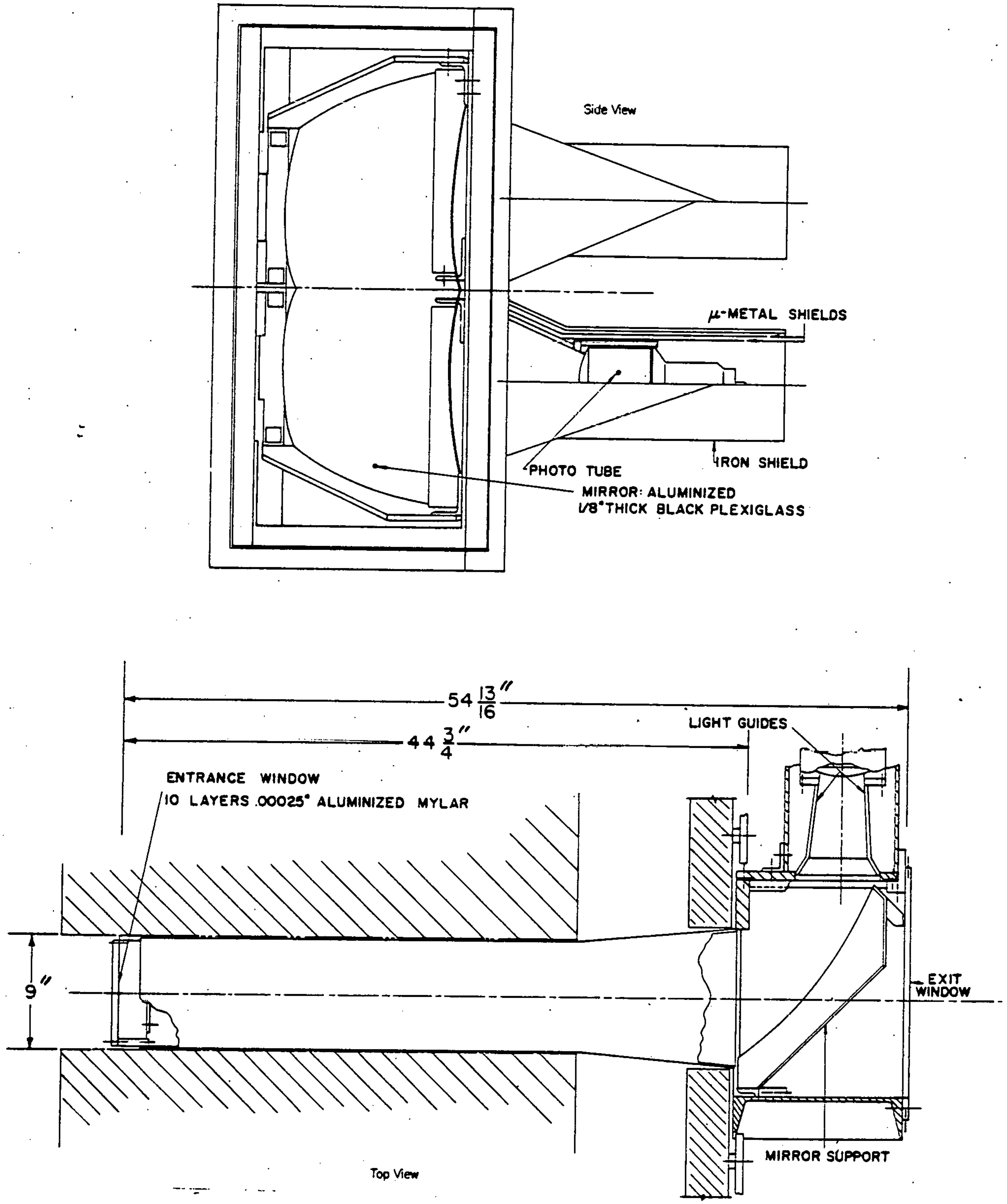

Figure VII-7: THRESHOLD CHERENKOV COUNTER

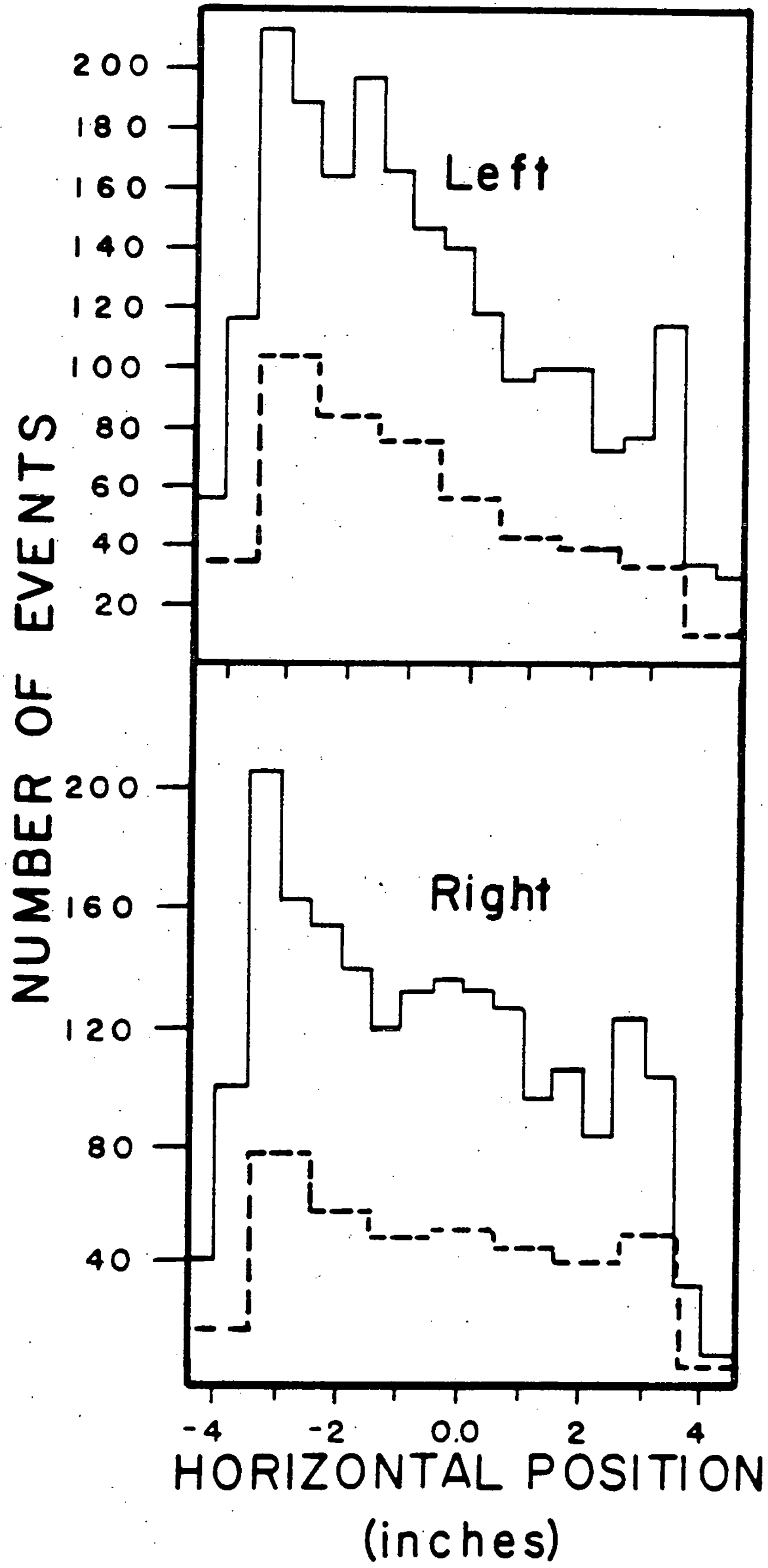

Figure VII-8: Horizontal position of pions (dashed line P > 3.5 GeV/c) detected by threshold Cherenkov counter compared to all charged particles (solid line) of momentum greater than 3.5 GeV/c. Program demanded a larger signal in the threshold counter than normally used in the analysis locations were consistent with the projected particle trajectory. The muon telescope was removed when the third arm was added to the spectrometer.

VIII. MOMENTUM DISTRIBUTIONS AND TWO BODY MASS SPECTRA

Once individual tracks had been reconstructed the momenta of the particles were computed. Small corrections (< 1%) were applied to the momenta to account for the inhomogenity of the magnetic field. These corrections were derived from measurements of the field integral ($\int \vec{B} \cdot \vec{d\ell} \cong 450$ Mev/c) taken along some 200 paths in the magnet gap. The measurements were made using a flip coil of dimensions 2" x 120" connected to an integrating circuit which measured the flux change when the coil was inverted. The individual measurements were reproduceable to ± .01%. The absolute value of the field integral is known to ~ 1.0%.

In Figures VIII-1 (a-g) we present examples of momentum spectra measured in this experiment. Figure VIII-1a is a histogram of the momentum of all positively charged particles in the left arm. The cutoff in the distribution near 1.25 Gev/c is imposed by the field integral of the magnet. The exponential tail reflects the physics of the interactions. The pion momentum spectra (Figure VIII-1b,c) are essentially identical to the charged particle distributions. We note there is a smooth transition near 3.0 Gev/c where the threshold counter becomes the primary means of identifying pions.

The proton momentum spectra (Figure IX-1 f,g) are also consistent with the charged particle specturm. The kaon momentum spectra (Figures IX-d,e) are, however, markedly different from the pion or proton distributions. As the kaon momentum increases above 1.0 Gev/c pions become increasingly misidentified as kaons, obscuring the normally sharp low-momentum cutoff. We note also that near 1.25

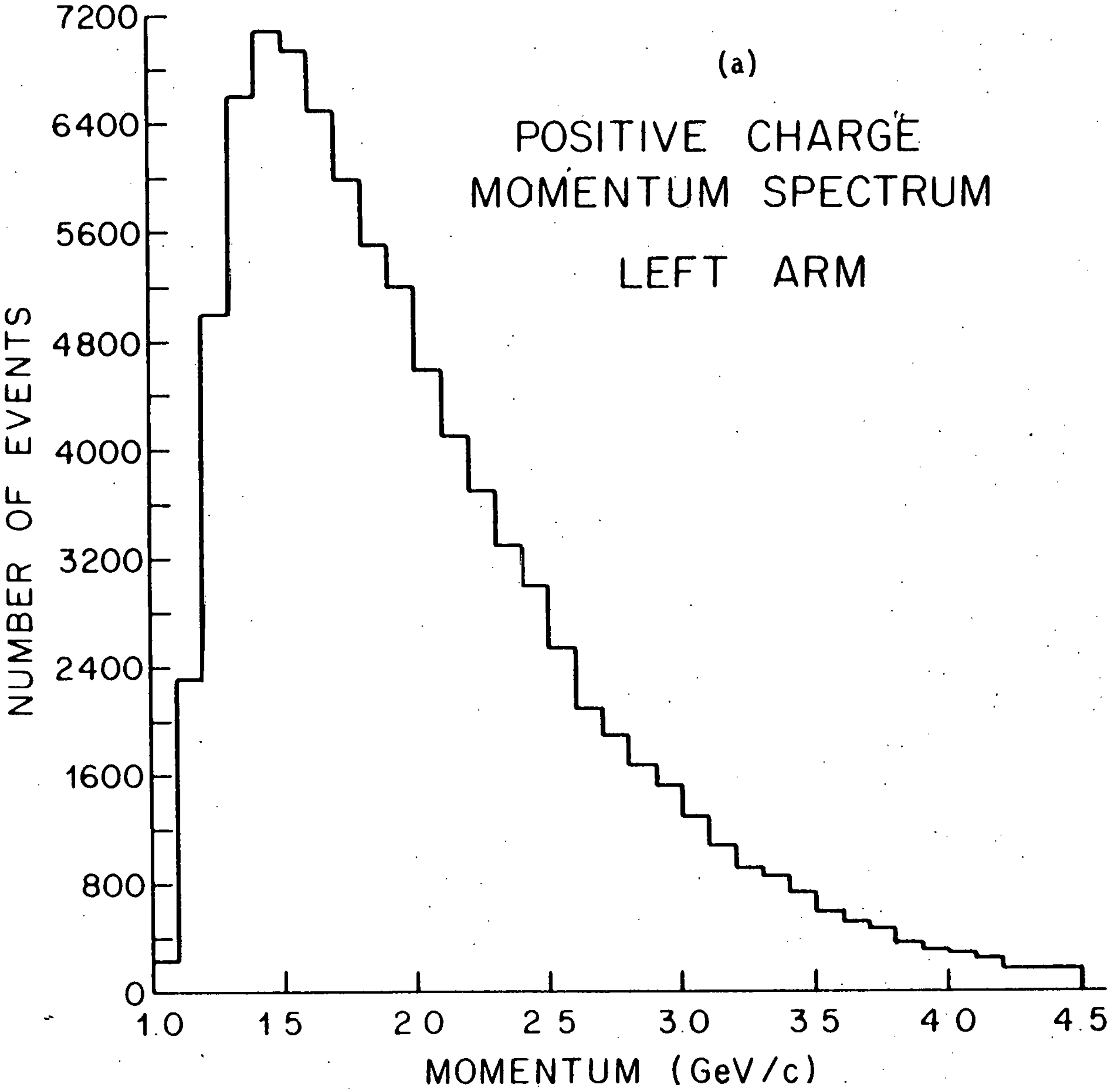

Figure VIII-1: Typical momentum spectra: (a) positively charged particles in left arm; (b) π^+ momentum spectrum (c) π^- momentum spectrum; (d) K^+ momentum spectrum; (e) K^- momentum spectrum; (f) Proton momentum spectrum (g) antiproton momentum spectrum. Data taken with 10.5 GeV/c pions.

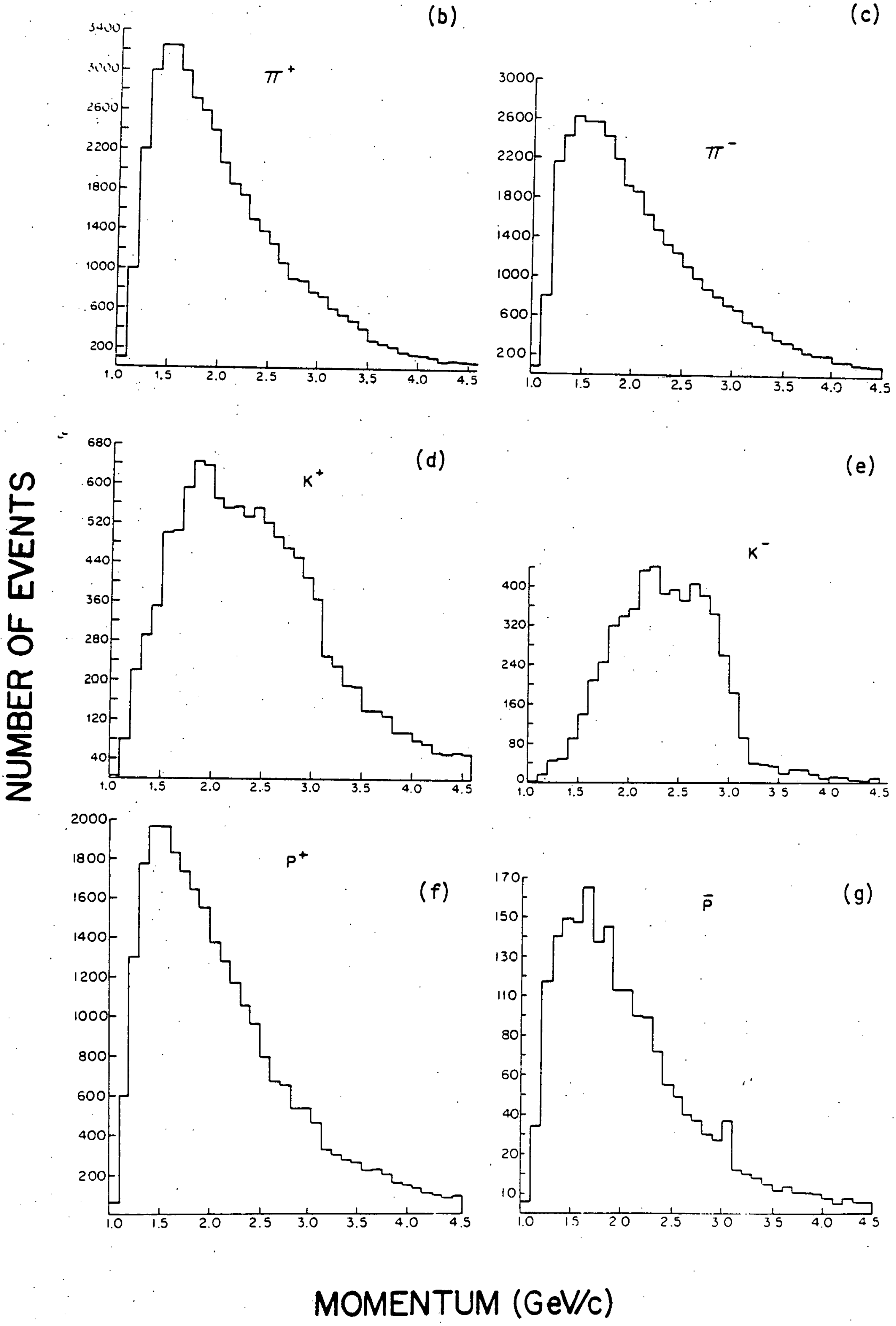

(b)
π⁺
3400
3000
2600
2200
1800
1400
1000
600
200
1.0 1.5 2.0 2.5 3.0 3.5 4.0 4.5
(c)
π⁻
3000
2600
2200
1800
1400
1000
600
200
1.0 1.5 2.0 2.5 3.0 3.5 4.0 4.5
(d)
K⁺
680
600
520
440
360
280
200
120
40
1.0 1.5 2.0 2.5 3.0 3.5 4.0 4.5
(e)
K⁻
400
320
240
160
80
0
1.0 1.5 2.0 2.5 3.0 3.5 4.0 4.5
p⁺
(f)
2000
1800
1600
1400
1200
1000
800
600
400
200
1.0 1.5 2.0 2.5 3.0 3.5 4.0 4.5
p̄
(g)
170
150
130
110
80
60
40
20
10
1.0 1.5 2.0 2.5 3.0 3.5 4.0 4.5
NUMBER OF EVENTS
MOMENTUM (GeV/c)

Gev/c, kaons are only marginally identified by the water Cherenkov counter. Above 3 GeV/c the pion contamination of the kaons is eliminated by the threshold Cherenkov counter, dramatically reducing the number of apparent kaons. The step in the momentum spectra is more pronounced in K^- than K^+ due to the fewer (greater) number of anti-protons (protons) to be misidentified as K^- (K^+). From the discussion of Chapter VII we estimate that approximately 60% of all real kaons are included in these momentum distributions.

Recall that at the time of the discovery of the J/ψ the best estimate for the mass of the D^0 was 2.3 GeV/c^2. To produce a $\bar{D}D$ pair at this mass in anti-proton interactions required a beam momentum of 12.4 GeV/c. Charmed mesons produced in pion interactions near threshold must be accompanied by a charmed baryon, if baryon number and charm are to be conserved. This requires an incident pion momentum of ~15 GeV/c, assuming, as was popular in 1974, that the mass of charmed baryons is of the order of 2.6 GeV/c^2.

In Figures IX-2a-c we display the π-K mass distributions of interest to the charm search. The data was collected using incoming beams of 15 GeV/c pions and anti-protons of momentum 12.4 GeV/c and 15 GeV/c.

It is possible to calculate the approximate mass recoiling against the K-π system and thereby reduce the background by requiring that this mass be equal to the mass of the observed K-π system. However, because the acceptance of the spectrometer is strongly peaked at the mass of the D, this technique would have introduced a false peak at the D mass. We do expect, however, that

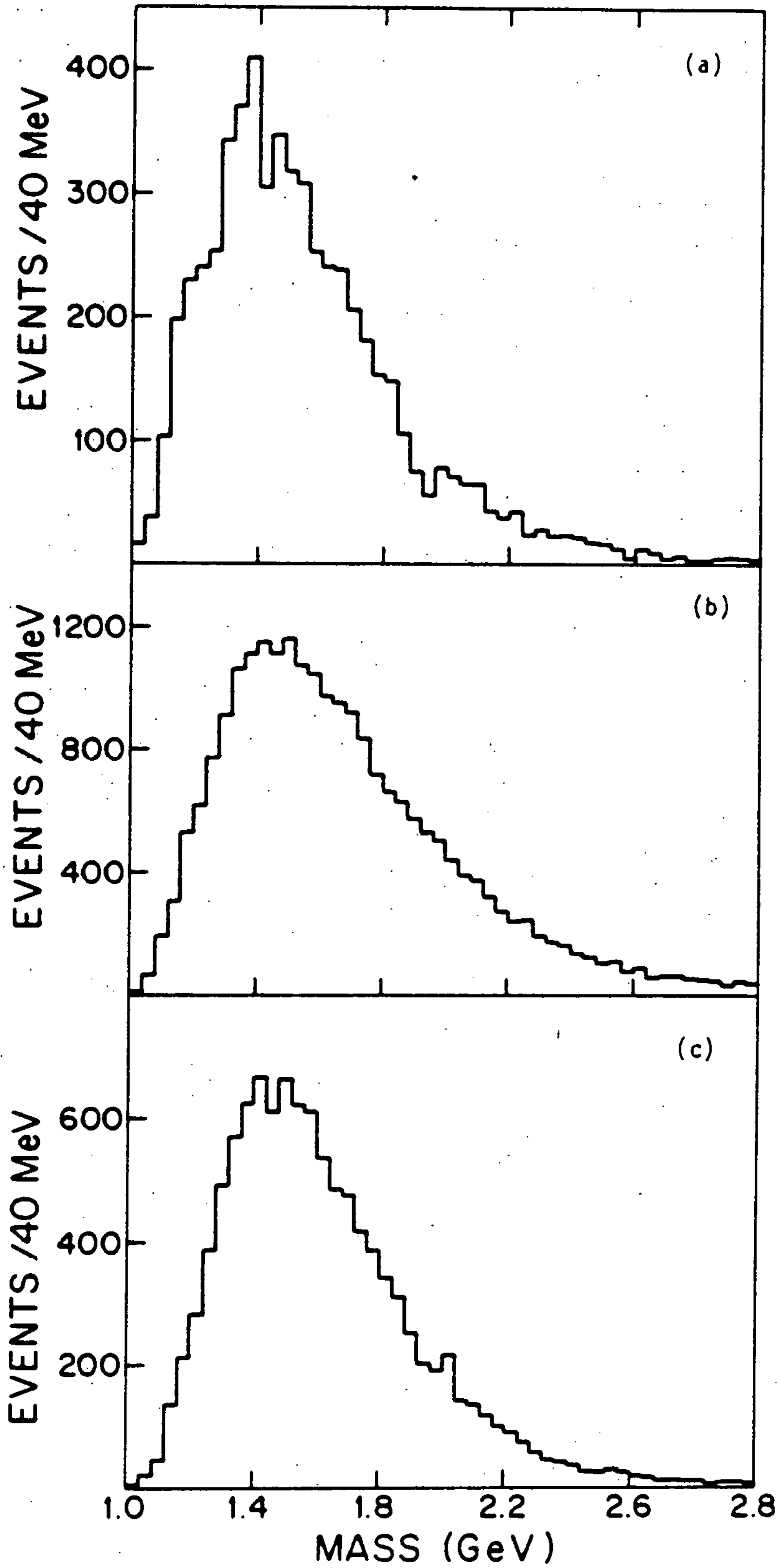

Figure VIII-2: (a) $K^{\pm}\pi^{\mp}$ invariant mass distribution for 12.4 and 15 GeV/c $\overline{P}N$ data; (b) $K^{+}\pi^{-}$ invariant mass distribution for $\pi^{-}N$ data; (c) $K^{-}\pi^{+}$ invariant mass distribution from $\pi^{-}N$ data.

a pion and a kaon originating from D decay should have roughly the same momentum. Therefore, events plotted in the $K\pi$ mass plots satisfied the restriction that:

$$\left| \frac{P_\pi - P_K}{P_\pi + P_K} \right| \leq .4 \cong 22\% \text{ of the D CMS polar angle.}$$

This cut eliminated approximately 10% of the events.

The invariant mass was calculated (with obvious notation) as:

$$M_{12}^2 = M_1^2 + M_2^2 + 2E_1E_2 - 2\vec{P}_1 \cdot \vec{P}_2$$

In Appendix 2 we show that $\delta M/M = 1\%$ for masses on the order of 2 GeV/c^2. The events are plotted at roughly twice the mass resolution of the spectrometer. No statistically significant structure is visible. Mass distributions for other two body combinations are tabulated in Appendix 4. The data taken with 8 GeV/c anti-protons and 10.5 GeV/c pions incoming beams will be described later.

To calculate upper limits for the cross section times branching ratio $\sigma\,(\bar{P}N \rightarrow D + X)\;B_{D\rightarrow K\pi}$ we use the usual criterion of requiring a 5 standard deviation effect in a mass bin equal to the mass resolution. For a given mass M_0, σB can be expressed as:

$$\left.\frac{d\sigma}{dM}\right|_{M=M_0 \pm \Delta M_0} B_{D\rightarrow K\pi} = \frac{N_{K\pi}}{\rho I\, \varepsilon\, N_A\, L_{eff}}$$

where $N_{K\pi}$ is the number of events in the mass interval $M_0 \pm \Delta M_0$, I is the number of incoming particles, ρ is the target density and N_A is Avogodro's number. The overall detection efficiency (ε) is the product of several factors:

$\varepsilon = \varepsilon_1 * \varepsilon_2 * \varepsilon_3 * \varepsilon_4 * \varepsilon_5$

ε_1= geometrical efficiency calculated from Monte Carlo simulations

ε_2= track reconstruction efficiency

ε_3= probability that a K or a π lies within the particle identification cuts (.6)

ε_4= fraction of all real events that fall inside a particular mass bin due to the finite resolution of the spectrometer (.6)

ε_5= correction for absorbtion of final $K\pi$ system in target (.8)

As the beam passes through the target the intensity is reduced due to absorbtion. We account for this by defining an effective target lengh (L_{eff}) such that:

$$L_{eff} = \lambda\,(1 - e^{-L/\lambda})$$

where λ is an absorbtion length in carbon and L is the actual length of the target. In Table VIII-1 we summarize the cross-section limits for the data taken at 12.4 and 15 GeV/c and in Appendix 5 we list the values of the ε's.

Using the muon telescope we could also measure J/ψ production via:

$$\pi^- N \to J/\psi + X$$
$$\qquad\qquad \left.\right|\!\!\to \mu^+ \mu^-$$

The muon trigger did not require an anti-proton signal and the data

TABLE VIII-1. CROSS SECTION LIMITS

Beam Momentum (GeV/c)			12.4	15	15
Process			$\bar{P}N \to D\,(\bar{D}) + X$	$\bar{P}N \to D\,(\bar{D}) + X$	$\pi^- N \to D\,(\bar{D}) + X$
Target			50 gm/cm^2 C.	50 gm/cm^2 C.	17 gm/cm^2 C
Sensitivity/event (cm^2/nucleon)					
	$M_D = 1.86$ GeV/c^2		$.126 \times 10^{-30}$ [a]		$.013 \times 10^{-30}$
	$M_D = 2.3$ GeV/c^2		$.042 \times 10^{-30}$		$.0045 \times 10^{-30}$
Events (5σ in 20 MeV)					
	$K^+\pi^- + \pi^- K^+$	(1.86)	33		
		(2.3)	20		
	$K^+\pi^-$	(1.86)	25		80
		(2.3)	14		50
	$K^-\pi^+$	(1.86)	20		61
		(2.3)	11		27
σB[b]	$\bar{P}N \to D(\bar{D}) + X$	(1.86)	4.2 μb		
		(2.3)	.8 μb		
	(π^-) $\bar{P}N \to \bar{D} + X$	(1.86)	3.0 μb		1.2 μb
		(2.3)	.6 μb		.22μb
	(π^-) $\bar{P}N \to D + X$	(1.86)	3.0 μb		.8 μb
		(2.3)	.5 μb		.12μb

---

[a] Data has been summed to improve statistics.

[b] Sensitivity includes efficiency for detecting final state kaon (.6) and absorption of final state particles in target (.8).

was collected during both the anti-proton and pion running. The di-muon mass spectra are shown in Figures VIII - 3, together with background spectra obtained from the like sign events. We observe one $\mu^+\mu^-$ event near mass 3.1 Gev/c^2. If we interpret this event as originating from the decay of a J/ψ, the cross section times branching ratio is:

$$\sigma * B_{J\to\mu^+\mu^-} = 5 \times 10^{-35} \text{ cm}^2$$

This limit assumes the J/ψ was produced in pion interactions . If we use the measured branching ratio of J/$\psi\to\mu^+\mu^-$ of 7% we obtain:

$$\sigma\ (\pi^- N \to J + X) = 7 \times 10^{-34} \text{ cm}^2$$

The data taken with an incoming beam momentum of 8.5 Gev/c represents our most sensitive search for charm production in anti-proton interactions. At this momentum, the acceptance of the spectrometer is optimized for D's of mass 1.86 Gev/c^2, as well as all of the process of equation V-1. Also the number of anti-protons per pion is highest at this beam momentum.

Two significant features are present in the K - π mass spectra taken at this energy (Figures VIII-4a,b). The first is a broad resonance near the peak of the π^-K^+ (π^+ K^-) mass spectrum. To estimate the production cross section for this resonance we fitted the mass distribution to the form:

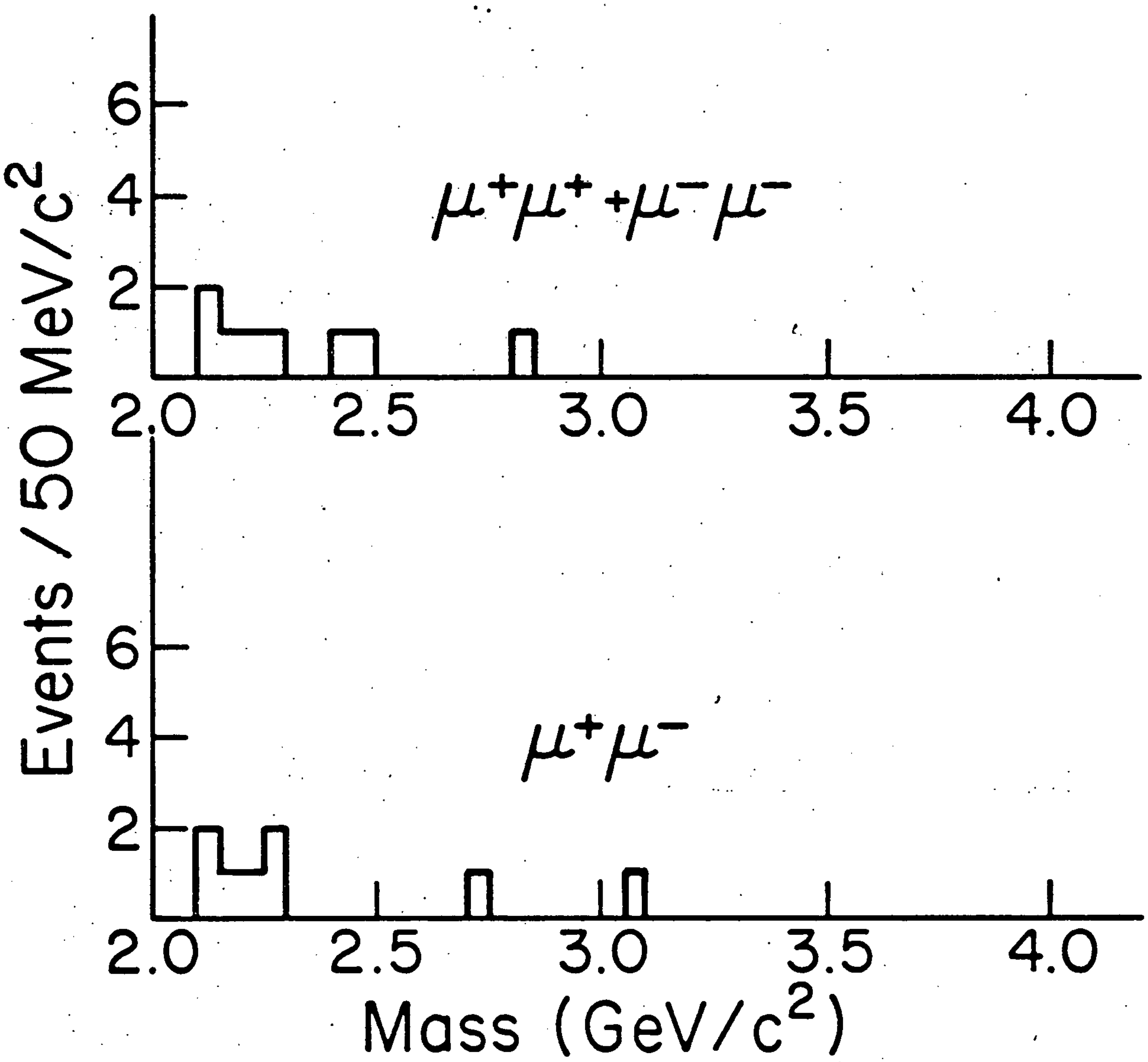

Figure VIII-3: Di-muom mass spectrum. Data corresponds to 3 x 10^{12} π^- incident on a 50 gm/cm^2 carbon target.

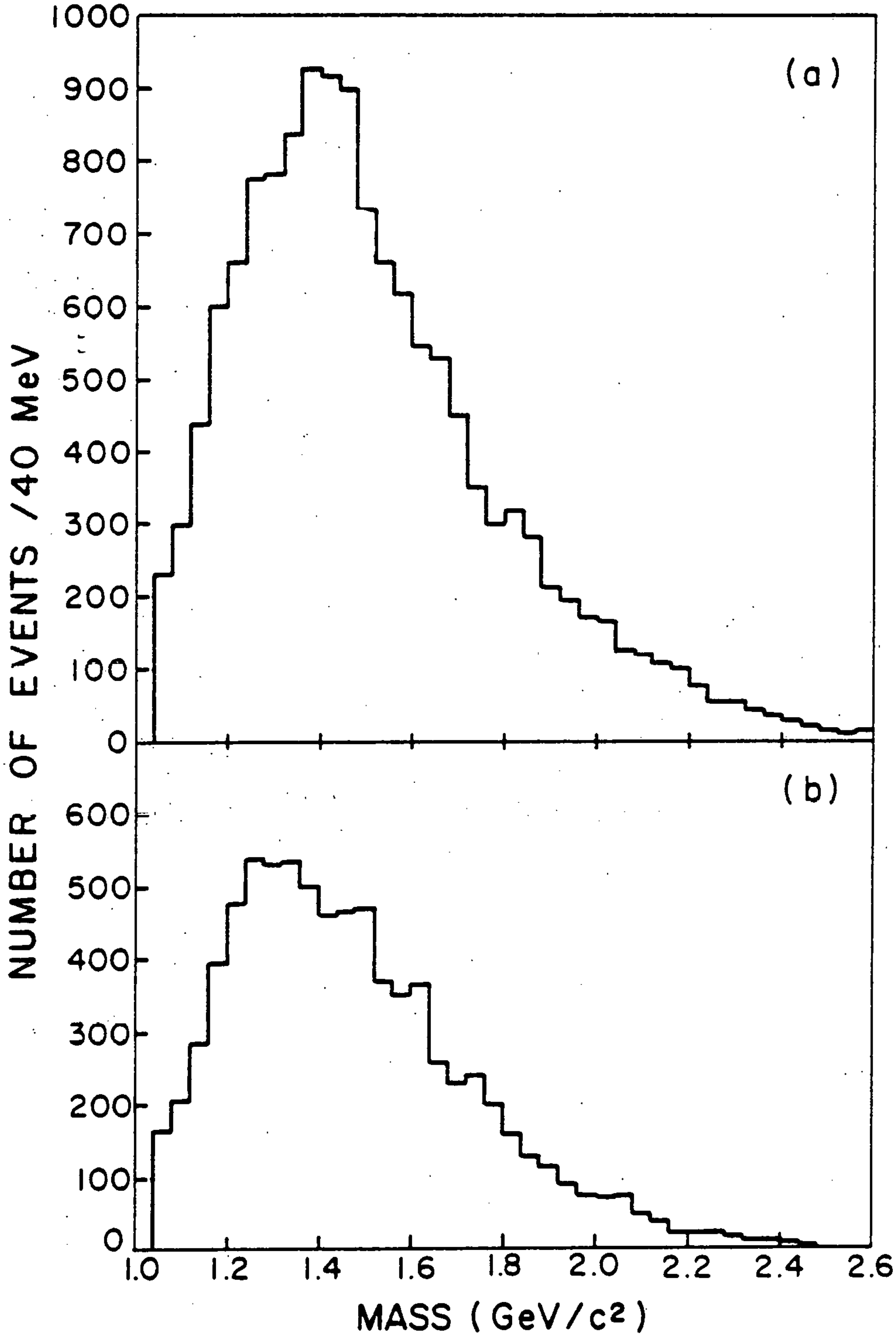

Figure VIII-4: Invariant mass distributions from 8.5 GeV/c $\overline{P}N$ data: (a) $K^{\mp}\pi^{\pm}$ invariant mass distribution (b) $K^{\mp}\pi^{\mp}$ invariant mass distribution.

$$\frac{dN}{dM} = \left(\sum_{n=0}^{5} C_n M^n\right) \left(e^{-bM} + \frac{A/2}{(M-M_0)^2 + \frac{\Gamma^2}{4}}\right)$$

The width and mass of the resonance determined in this way (Figure VIII-5) are $M_0 = 1.400 \pm 0.01$ Gev/c^2 and $\Gamma = .103 \pm .021$ Gev/c^2, consistent with the K* (1421). The number of events contained in the Breit-Wigner is 550 ± 200. The error in this number seems unacceptably high, especially when we compare the data with a background curve obtained from the like sign ($\pi^+ K^+$ and $\pi^- K^-$) data (Figure VIII-6). For this reason, we refitted that data fixing the width of the resonance at the nominal value $\Gamma = .108$ GeV/c^2. The mass and amplitude for the resonance obtained in this way are M_0 1.400 ± 0.010 Gev/c^2 and 550 ± 110 events, respectively.

This resonance provides a convenient calibration point for the mass scale. Using the accepted value for the mass of the K* (1421) we calculate that the systematic error in the mass scale is approximately 1%.

To compute the production cross section times branching ratio we used an estimate of the geometrical acceptance obtained from a Monte Carlo simulation of the apparatus. The Monte Carlo program assumed that the minimum mass recoiling against the K* was .493 Gev/c^2 and included the effects of target Fermi momentum. The momentum distribution of the K* (1421) perpendicular to the beam axis was picked according to the rule:

$$\frac{dN}{dP_\perp} \alpha\ P_\perp\ e^{-5T}$$

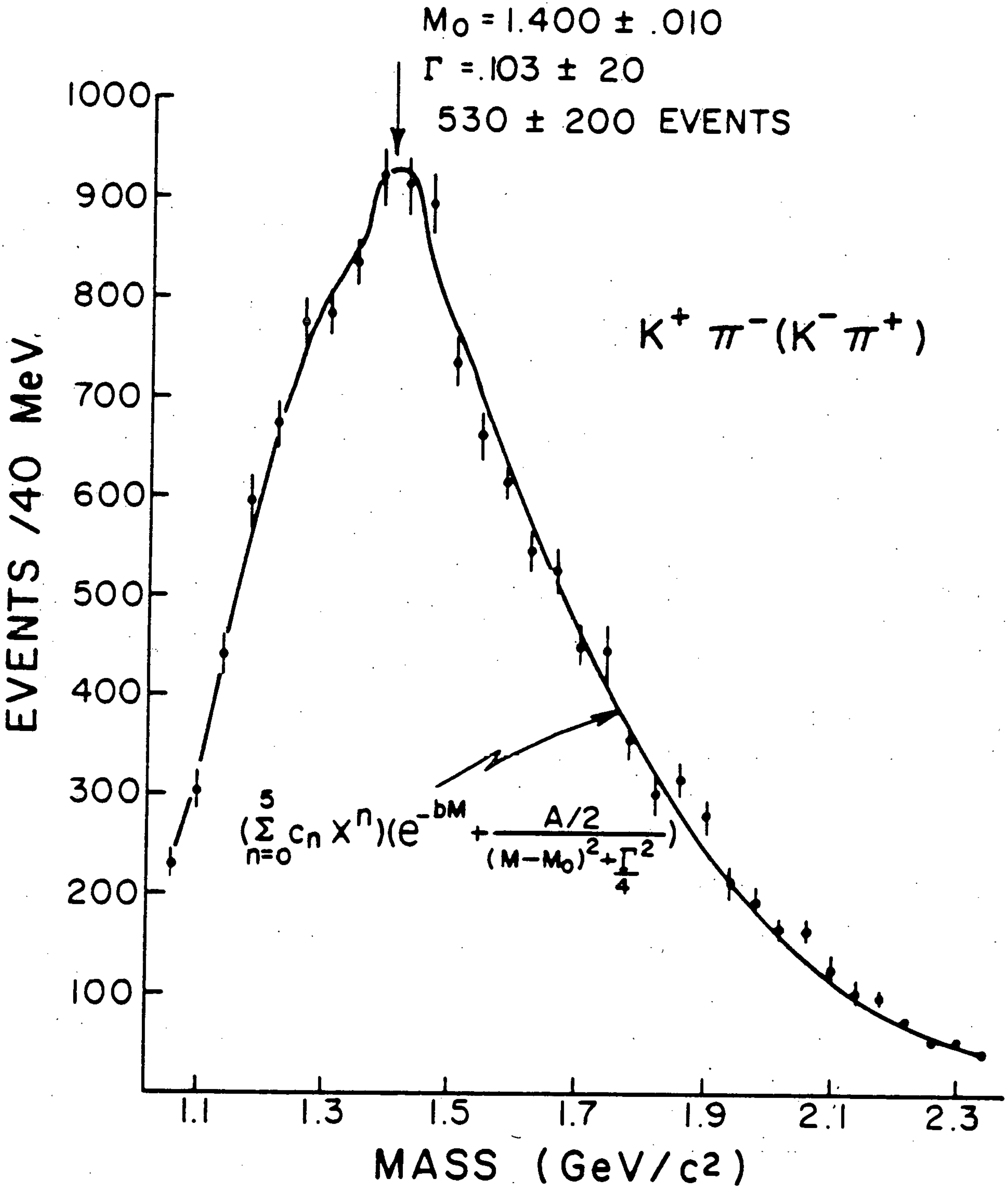

Figure VIII-5: Fit of $K^{\pm}\pi^{\mp}$ invariant mass distribution to functional form shown. Data was collected with an incoming beam of 8.5 GeV/c anti-protons.

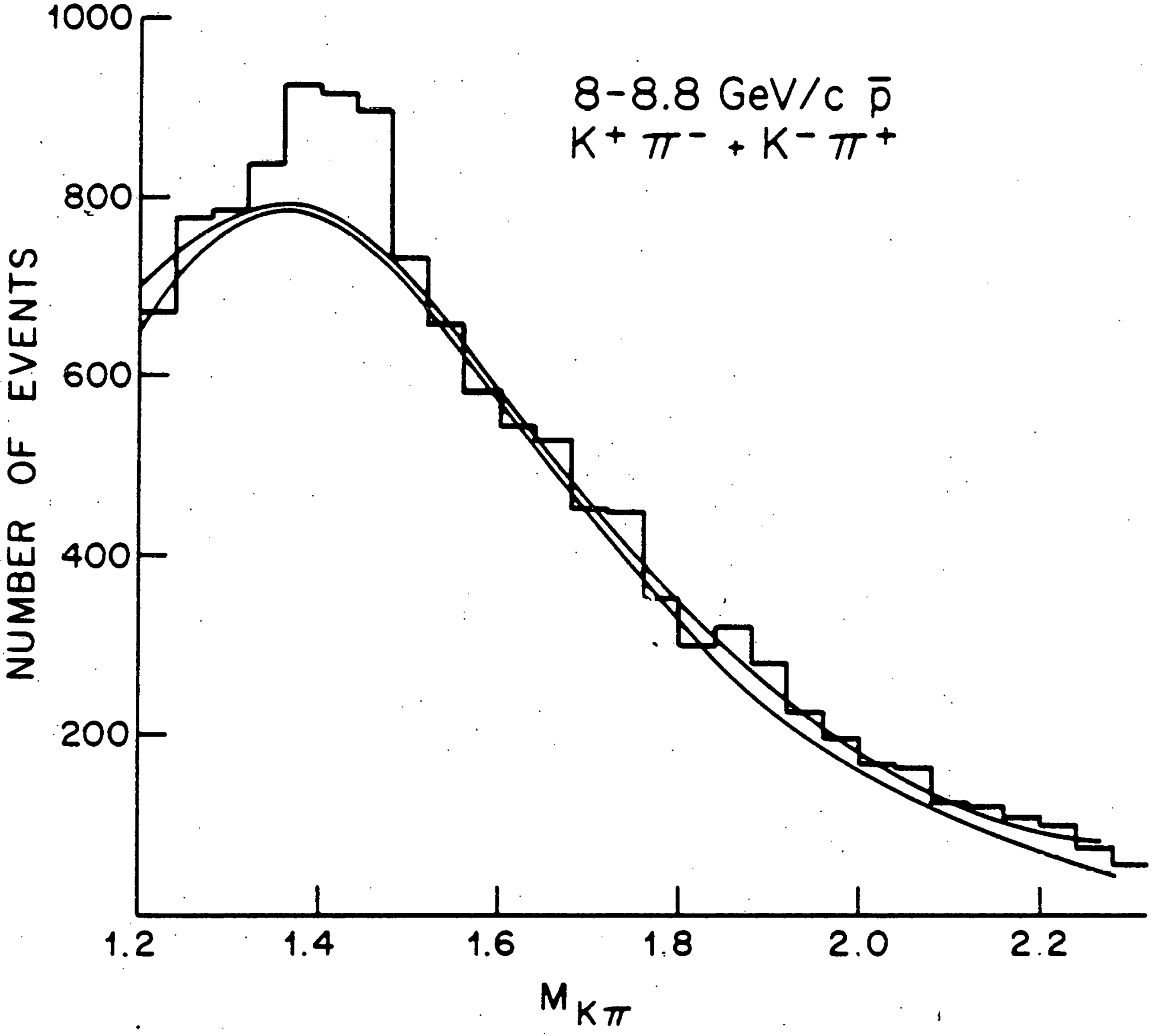

Figure VIII-6: $K^\pm \pi^\mp$ invariant mass distribution with background curve obtained from like-sign ($K^\pm \pi^\pm$) data. Data was collected with incoming 8.5 GeV/c anti-protons.

where $T = \sqrt{(3/2\ P^2 + 2.)} - 1.420$. The distribution of momentum along the beam was chosen independent of $x_F = P^*_{||} / P^*_{max}$. and the decay into π-K was assumed to be isotropic in the K* center of mass. The resulting efficiency was calculated to be 1.8×10^{-4}. When we include the reconstruction and K-π detection efficiencies, and account for the absorbtion of the Kπ system in the target, we compute:

$$\sigma_{K*}B_{K\pi} = \frac{N_{K\pi}}{\rho\, \varepsilon\, I\, N_A\, L_{eff}} = \frac{550 \qquad (cm^2)}{(2.3)*(8.6x10^{-6})*(9.4*10^{10})*(6x10^{23})*(12.5)}$$

$$= 4 \times 10^{-29} \pm .8 \times 10^{-29}\ cm^{+2}$$

where the error is statistical. Although there are no other measurements of inclusive K* production, this result is consistent with measurements of exclusive processes[32],eg.:

$$\sigma(\overline{P}N \to K^* + K_S)*B_{K^* \to K^+\pi^-} = 10 \pm 6\ \mu b \text{ at } P_{beam} = 1.18\ GeV/c$$

$$\sigma(\overline{P}N \to K^* + K_S)*B_{K^* \to K_S\pi^+\pi^-} = 25 \pm 10\ \mu b \text{ at } P_{beam} = 1.2\ GeV/c$$

The other feature of interest in the K-π mass plots is a small enhancement in the cross-section near 1.86 GeV/c^2 , the known mass of the D^0. To measure the statistical significance of this peak we fitted the background plus signal to the form:

$$\frac{dN}{dM} = A^* \exp(-b^*M) + B * \exp(-(M - M_0)^2/2 * \sigma^2)$$

where M_0, A, B, b, and σ were allowed to vary. The results of this procedure are shown in Figure VIII-7a,b.

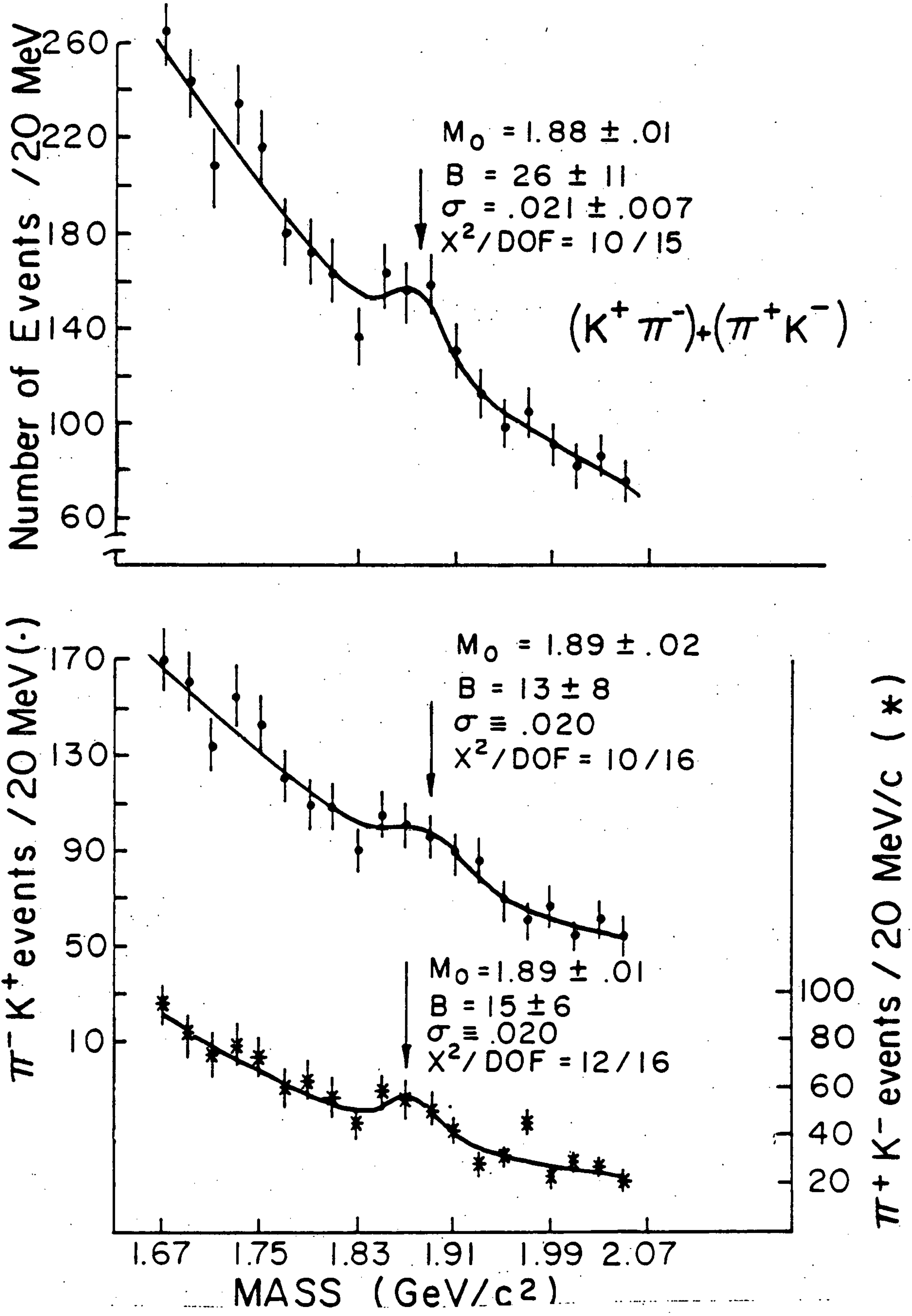

Figure VIII-7: Expanded view of region near 1.86 GeV/c^2 from $\bar{p}N$ data taken at 8.5 GeV/c: (a) $K^{\pm}\pi^{\mp}$ invariant mass distribution (b) $K^+\pi^-$ invariant mass distribution; (b) $K^-\pi^+$ invariant mass distribution. Variables are described in text.

The values for M_o and B obtained in this manner were $M_o = 1.88 \pm .01$ GeV/c^2 and B = 26 ± 11, corresponding to 65 ± 25 events. The calculated width is consistent with the mass resolution of the spectrometer. We calculate the cross section times branching ratio to be:

$$\sigma(\overline{P}N \rightarrow D^o\ (\overline{D}^o) + X)\ B_{K\pi} = 780 \pm 300 \text{ nb} \quad ,$$

where the error is statistical. These numbers, as well as the results for the individual channels $K^+\pi^-$ and $K^-\pi^+$ are summarized in Table VIII-2a. For purposes of comparison, in Table VIII-2b we list the cross-section limits equivalent to a five standard deviation effect in a 20 MeV mass bin.

These results are not conclusive evidence for the existence of charm. The effect is, however, of enough significance to warrant further investigation with an improved apparatus. In the meantime, other tests have been performed to improve the signal in the existing data.

We chose to replot the data weighted by the probability that we had correctly identified the decay products. We note that in Figure VII-2 that the ratio (Δ) distribution in the water counter is roughly Gaussian. Therefore, we defined the probability that a particular particle was a pion, kaon proton by:

$$P_i \propto e^{-(\Delta_M - \Delta_{ci})^2/2\sigma^2}$$

where Δ_M is the measured ratio, Δ_{ci} is the value calculated from equation VII-2 and $\sigma = 0.25$. A probability (P_π, P_K, P_P) was calculated for each assumed mass. The individual probabilities were normalized such that $P_\pi + P_K + P_P = 1$.

TABLE VIII-2: CROSS SECTION LIMITS

BEAM MOMENTUM	8.0 - 8.8 GeV/c
PROCESS	$\overline{P}N \to D\ (\overline{D}) + X$
TARGET	33 gm/cm^2 C
INCIDENT FLUX	9.4×10^{10}
SENSITIVITY/EVENT (cm^2/nucleon)	12×10^{-33}
EVENTS	
$K^+\pi^- + K^-\pi^+$	65 ± 25
$\pi^-\ K^+$	35 ± 20
$\pi^+\ K^-$	37 ± 15
σB	
$\overline{P}N \to D(\overline{D})+X$	780 ± 300 nb
$\overline{P}N \to \overline{D}+X$	420 ± 240 nb
$\overline{P}N \to D+X$	450 ± 180 nb

TABLE VIII-2b: CROSS SECTION LIMITS

BEAM MOMENTUM	8.0 - 8.8 GeV/c
PROCESS	$\overline{P}N \to D\ (\overline{D})\ +X$
TARGET	33 gm/cm^2 C
INCIDENT FLUX	9.4×10^{10}
SENSITIVITY/EVENT (cm^2/nucleon)	20×10^{-33}
EVENTS (5σ in 20 MeV)	
$K^+\pi^- + K^-\pi^+$	60
$\pi^- K^+$	48
$\pi^+ K^-$	30
σB	
$\overline{P}N \to D(\overline{D})+X$	1.2 μb
$\overline{P}N \to \overline{D}\ +X$	1.0 μb
$\overline{P}N \to D+X$	.6 μb

The ratio information is only useful when a sufficient number of photoelectrons have been collected in the water counter. Since the sumof the number of photoelectrons can also be described by a Gaussian, we multiplied the normalized probabilities described above by a factor F defined by:

$$F = e^{-(S_M - S_o)^2/2\sigma_S^2}$$

where S_o is the average number of photoelectrons collected from a single particle, σ_S is the width of the distribution and S_M is the measured sum. Hence, events with too many or two few photoelectrons were suppressed.

In situations where there was also a signal in the threshold counter the probabilities P_π, P_K, and P_p were calculated in exactly the same way, except that at the end of the calculation P_p and P_K were set equal to zero. This technique was used to avoid the introduction of a step in the pion momentum distribution.

Protons below the threshold for detection in the water counter had to be treated as a special case, because no ratio information was available. We calculated the probability that a particle was a proton on the basis of the number of photoelectrons collected in the outer ring of phototubes. We found that the probability was reasonably represented by the form:

$$P = A\, e^{-w^2/2\sigma(p)^2}$$

where w is the measured number of photoelectrons in the outer ring. The width of the distribution $\sigma(P)$ was estimated by examining the

SUMOUT curves (Figure VII-5) for several momentum regions. The behavior of $\sigma(P)$ as a function of momentum (P) is plotted in Figure VIII-8. The amplitude A was chosen so that both the proton and anti-proton distributions were continuous is the transition region.

The weighted momentum distributions and $K^{\pm} - \pi^{\mp}$ mass plots calculated in this way are shown in Figures VIII-9 and VIII-10a, b, respectively. No significant improvement in the signal at 1.86 Gev/c^2 is seen. Fitting the $K^- - \pi^-$ ($\pi^+ - K^-$) distribution as above and allowing A,b,B M_0 and σ to vary we find that:

$$M_0 = 1.898 \pm .001 \text{ Gev/c}^2$$

$$\sigma = .018 \pm .006 \text{ Gev/c}^2$$

$$B = 25 \pm 8$$

$$X^2/DOF = 19/16$$

These results are consistent with the values quoted earlier and we retain the previous limits.

We caution the reader that the absolute normalizations of the cross-sections could be in error by as much as a factor of 2. This uncertainty arises primarily from the estimate of the reconstruction efficiency, which was calculated by examining individual events by eye. Additionally, for the pion induced data, the incident flux was calculated by scaling the number of incoming anti-protons by a factor obtained from Figure IV-2. Although the π/P ratio was verified at each relevent energy, these measurements were conducted at a reduced intensity. Systematic effects which arise only during high-intensity running (eg.: inefficiency in the beam Cherenkov counter) contribute to the overall uncertainty.

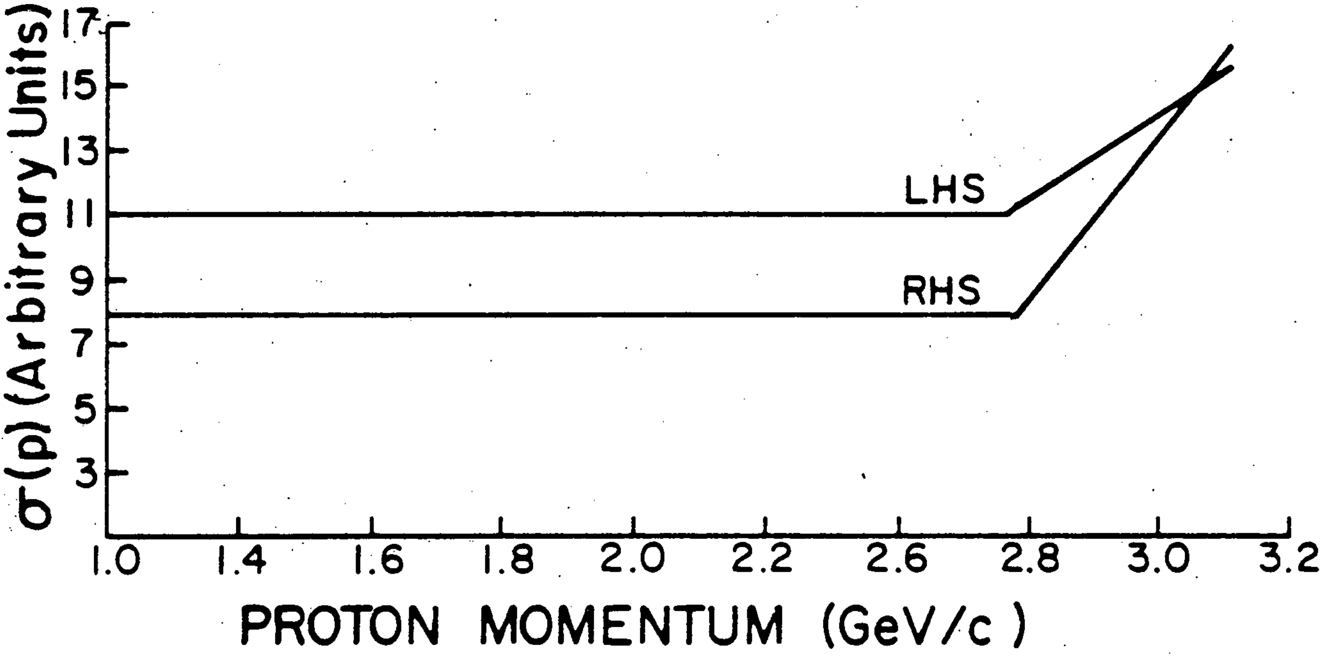

Figure VIII-8: Width of SUM OUT curves used in analysis of low momentum protons. The two curves refer to the right and left arms of the spectrometer.

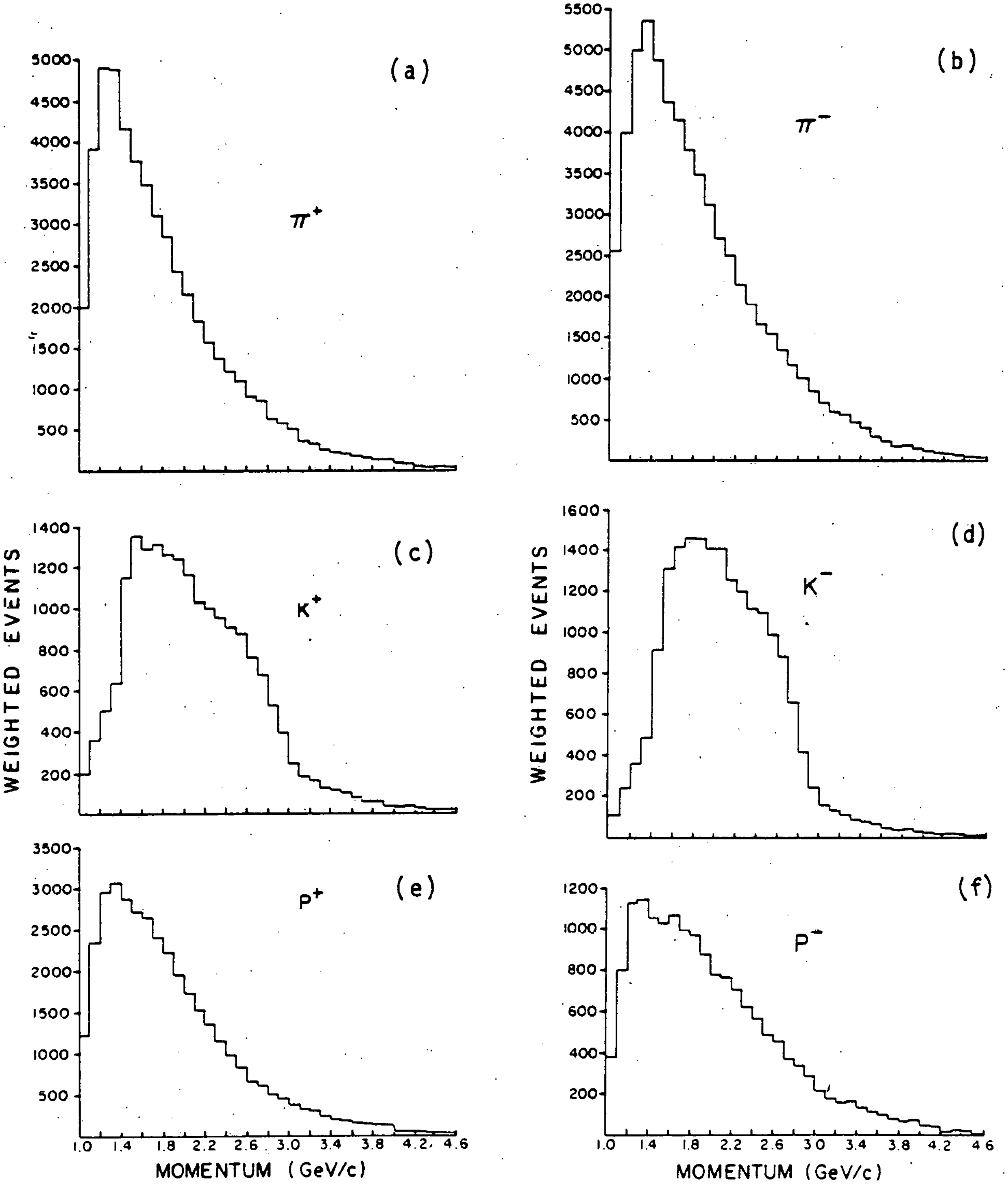

Figure VIII-9: Weighted momentum distributions: (a) π^+momentum distribution; (b) π^- momentum distribution; (c) K^+ momentum distribution; (d) K^- momentum distribution; (e) proton momentum distribution; (f) anti-proton momentum distribution.

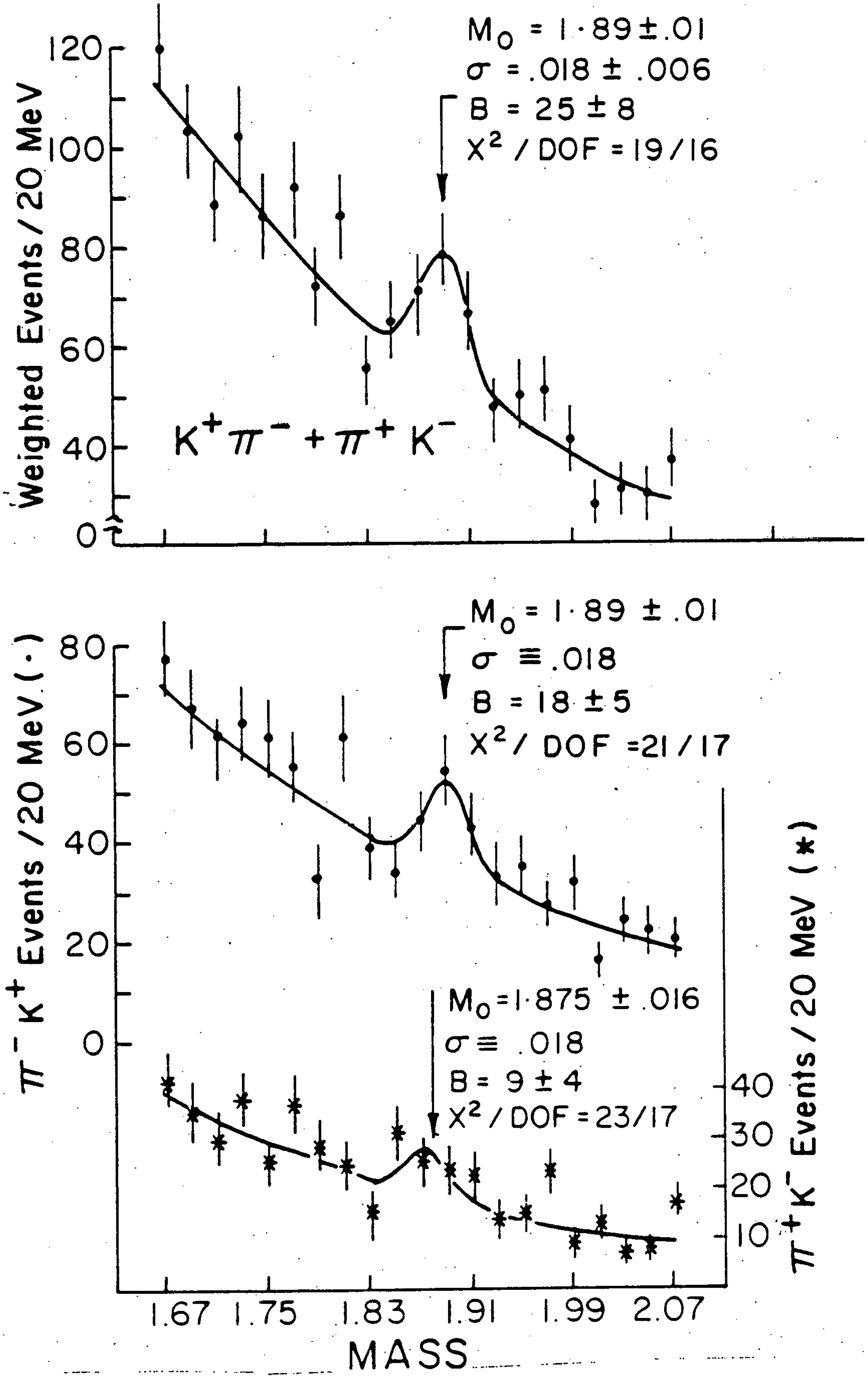

Figure VIII-10: Weighted invariant mass distributions; (a) $K^{\pm}\pi^{\mp}$ invariant mass distribution; (b) $K^+\pi^-$ and $K^-\pi^+$ invariant mass distributions. Data was collected with an incomming beam of 8.5 GeV/c anti-protons. Variables are described in text.

IX. CHARM PRODUCTION IN PION INTERACTIONS

As described in Chapter V the purpose of the third, forward arm of the spectrometer was to detect the cascade pion from the decay:

$$\begin{array}{l} D^{*-} \longrightarrow \bar{D}^{0} + \pi^{-} \\ \qquad\quad \bigsqcup\!\!\longrightarrow \; K^{+} + \pi^{-} \end{array} \tag{1}$$

All of the data taken with incoming 10.5 Gev/c pions was collected using the signals from the third arm to reduce the high double arm trigger rate. Part of the data taken at 8.5 Gev/c included tagging information from the third arm hodoscope. Knowing the production angle and momentum of the slow pion is was possible to reduce the background further in the off-line analysis by requiring that the measured Q value be consistent with the value observed at SPEAR.

Because the cascade pion emerges along the beam line it was impossible to measure the production angle before the third arm spectrometer magnet. Hence, the measurement of the production angle is correlated with the measurement of the momentum.

Not all counter combinations were permitted. Only those combinations which projected back through the center-line of the magnet to the hole in the shield plates of the spectrometer magnets were used in reconstruction.

In Figure IV-1 we plot the production angle of the cascade π in the horizontal plane versus the calculated momentum for all valid counter combinations. The error bars indicate the size of the error elipses about each point. We observe that the momentum and angular resolution is poor.

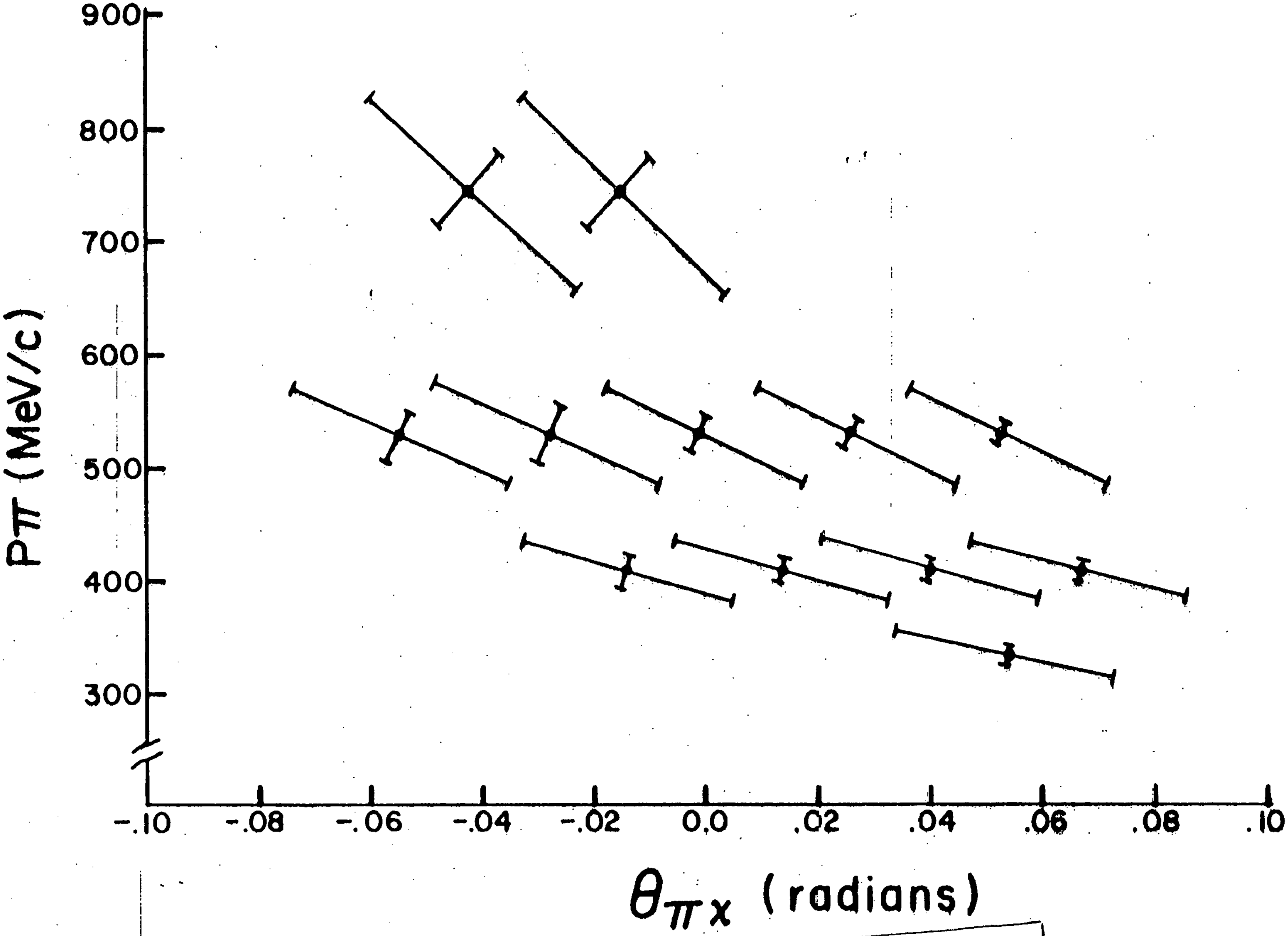

Figure IX-1: Momentum of cascade pion as a function of production angle in horizontal plane for all valid counter combinations. See text for explanation.

The front hodoscope of the third arm consisted of eight 18" x 18" scintillation counters, divided into an upper and lower tier. Each counter overlapped its neighbor by half a counter width, so that the horizontal spatial resolution was 9". The rear hodoscope consisted of six 12" x 60" scintillation counters placed side by side (Figure IX-2).

Each overlap region in the front hodoscope and each scintillation counter in the rear hodoscope was assigned a number, as shown in Figure IX-2. We found that the momentum of the slow pion and its production angle ($\theta_{\pi x}$) in the horizontal plane could be expressed as a linear function of these two numbers. Specifically:

$$\begin{aligned} P_\pi &= P_{MAG}/(C_1 + C_2\,(n_1 - n_2)) \\ \theta_{\pi x} &= C_5 + C_3 n_1 - C_4 n_2 \end{aligned} \tag{2}$$

Information about the production angle in the vertical plane was also available because the front hodoscope was divided vertically into an upper and lower half. Given $\theta_{\pi x}$ from equation (2) we compute $\theta_{\pi y}$ according to:

$$\theta_{\pi y} = \pm \frac{1}{2} \sqrt{(R/r)^2 - \theta_{\pi x}^{\,2}}$$

where the +(-) sign applies if the signal was in the upper (lower) hodoscope bank (see Figure IX-3).

Having computed P_π, $\theta_{\pi x}$ and $\theta_{\pi y}$ we calculate the mass of the $K\pi\pi$ system:

$$M^2_{D^{*-}} = M_D^{\,2} + 2E_\pi E_D - 2\vec{P}_\pi \cdot \vec{P}_D + M_\pi^2$$

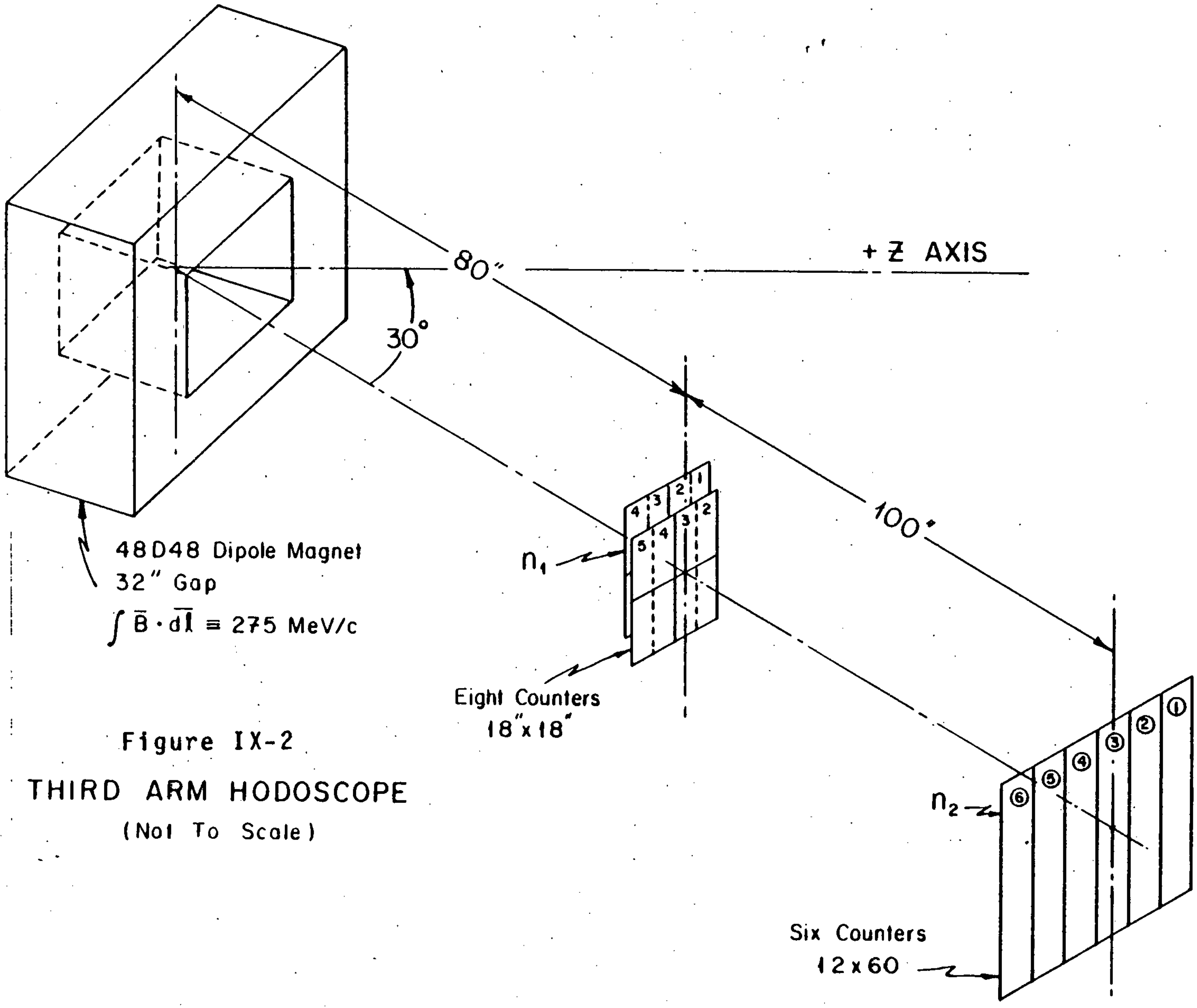

Figure IX-2

THIRD ARM HODOSCOPE

(Not To Scale)

Figure IX-3: Computation of $\theta_{\pi y}$ for cascade pion

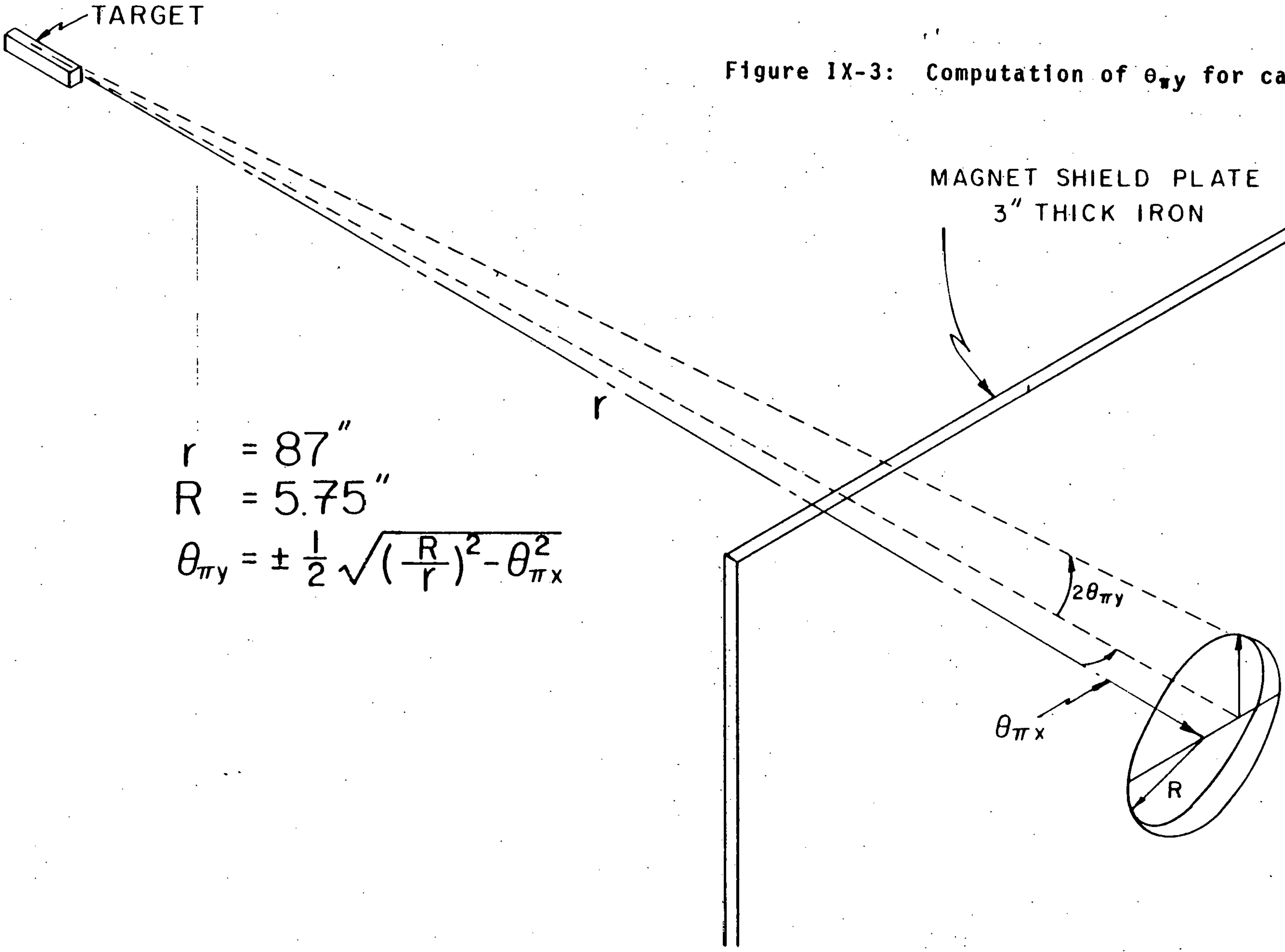

$$r = 87''$$

$$R = 5.75''$$

$$\theta_{\pi y} = \pm \frac{1}{2}\sqrt{\left(\frac{R}{r}\right)^2 - \theta_{\pi x}^2}$$

Since both the momentum of the Kπ system and the slow pion point roughly along the +z axis we can expand the fourth term in a Taylor series

$$\bar{P}_\pi \cdot \bar{P}_D = P_\pi P_D \cos\theta$$

$$= P_\pi P_D \left(1 - \frac{1}{2}(\theta_{\pi x} - \theta_{Dx})^2 - \frac{1}{2}(\theta_{\pi y} - \theta_{Dy})^2\right)$$
$$= P_\pi P_D \left(1 - \frac{1}{2}(\theta_x^2) - \frac{1}{2}(\theta_y{}^2)\right)$$

The Q value is defined as:

$$Q = M_{D*} - M_D - M_\pi$$

For small Q it is easy to show that

$$Q \cong \frac{E_\pi E_D - P_\pi P_D \cos\theta - M_\pi M_D}{M_\pi + M_D} \equiv Q_o \qquad (3)$$

One correction must be made to this expression. Expanding Q in a Taylor series in P_π about Q = 0 we find:

$$Q = Q_o + \frac{\partial Q}{\partial P_\pi}\delta P_\pi + \frac{\partial^2 Q}{\partial P_\pi{}^2}\frac{\delta P_\pi{}^2}{2}$$

Near Q = 0 the first and second terms are small but the third term is always positive (since Q is at a minimum) and can contribute significantly to the value of Q near zero. Hence, to the value of Q computed in equation (3) we add the second order term:

$$\frac{\partial Q_2}{2\,\partial P_\pi^2}\,\delta P_\pi^{\,2} = \frac{E_D M_\pi^2\,\delta P^2}{2\,E^3_\pi (M_D + M_\pi)} \equiv Q_2$$

$$Q \equiv Q_0 + Q_2$$

For each value of Q we assign an error δQ. The expression for δQ is complicated, since $P_\pi, \theta_{\pi x}$ and $\theta_{\pi y}$ are all related. It is fully calculated in Appendix 4. We do note that the measurement of Q is rather crude; δQ is on the order of $\pm$ 5 MeV.

Given the value of Q we retain only those events in the Kπ mass plot with Q value equal to (within errors) the value measured at SPEAR (5.6 MeV). The K-π mass distributions accumulated with 10.5 Gev/c incoming π^- are shown in Figures IX-4 , while the data collected with incident 8.5 Gev/c antiprotons is shown in Figures IX-6a,b. Computing the cross-section limits as before, we find that:

$$\sigma\,(\pi^- N \to D^{*-} + X)\, B_{D^{*-} \to \pi^- \bar{D}^0} * B_{\bar{D}^0 \to K^+\pi^-} \le 16 \pm 16 \text{ nb}$$

This result includes the efficiency for detecting the cascade π^- (.25) and the absorption of the pion in the target. If one assumes that 1/3 of all D^0's come from D* decay, this implies that

$$\sigma\,(\pi^- N \to D^0 + X)\, B_{D \to K\pi} \le 48 \pm 48 \text{ nb}$$

We saw no events near 1.86 Gev/c^2 in the anti-proton data taken with third arm tagging. Using the standard criteria of a 5 standard deviation effect (5 events) we compute:

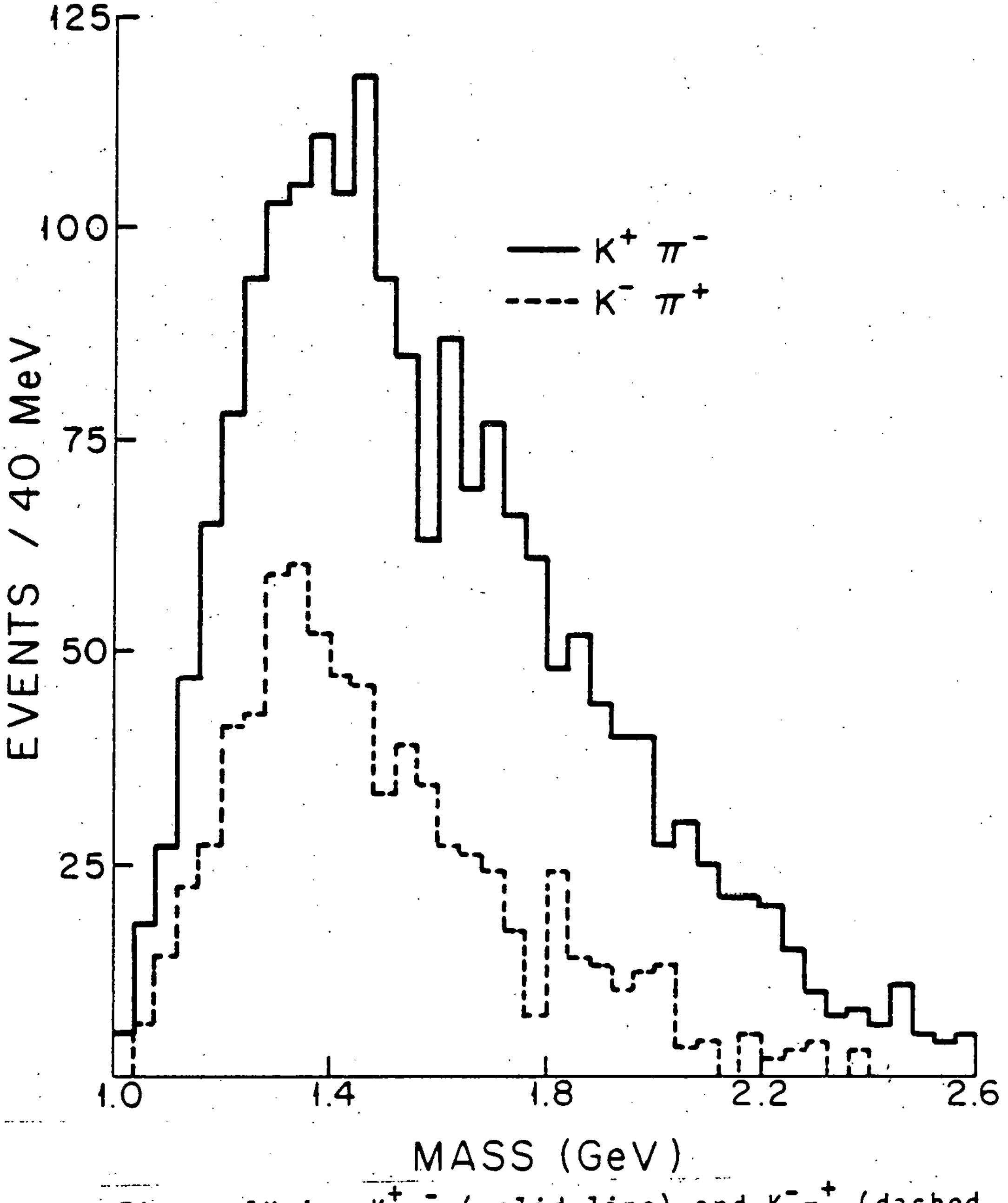

Figure IX-4: $K^+\pi^-$ (solid line) and $K^-\pi^+$ (dashed line) invariant mass distributions for data taken with incoming 10.5 GeV/c π^- with third spectrometer arm in trigger. Only those events with Q value consistent with the value measured at SPEAR have been retained

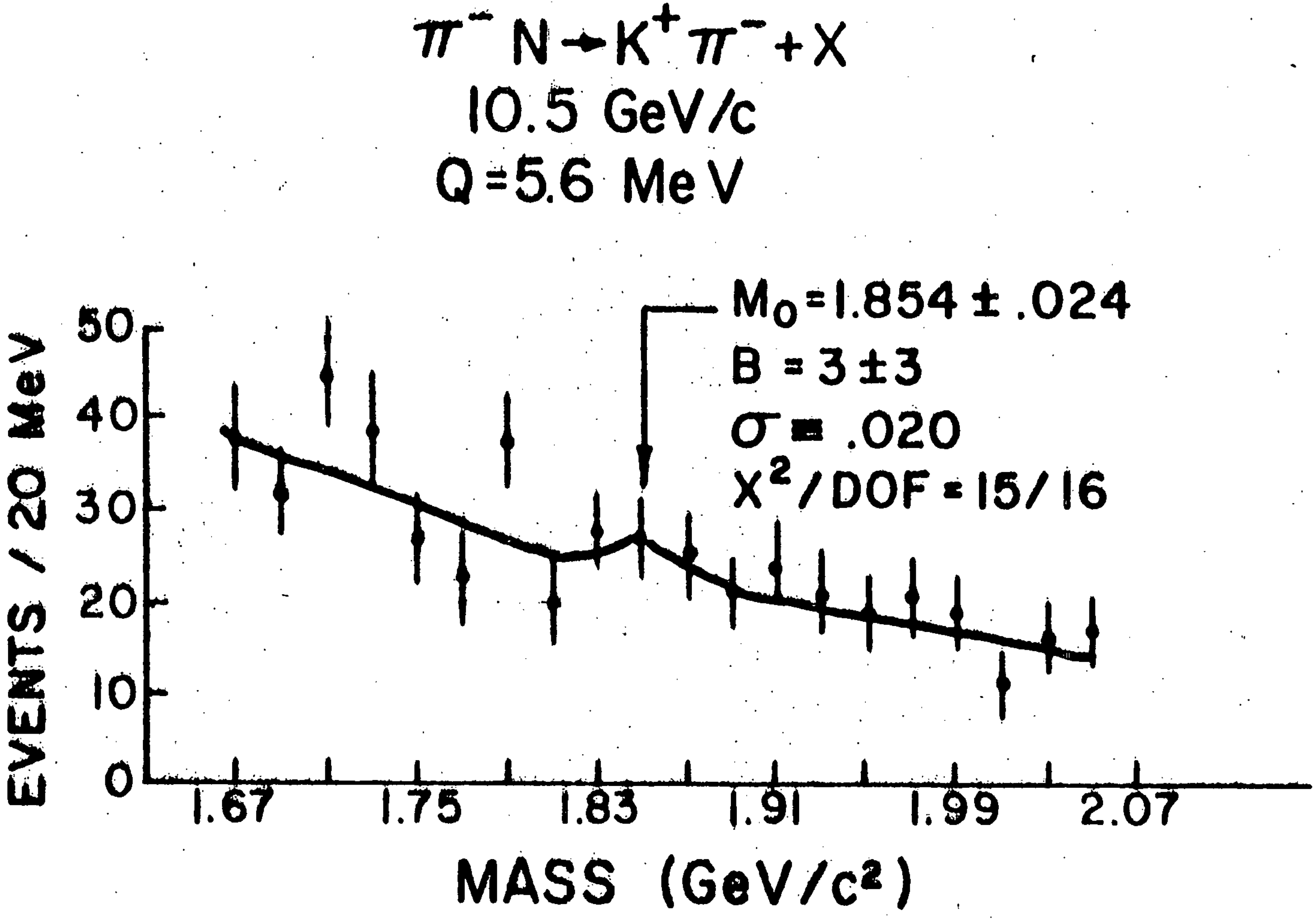

Figure IX-5: Expanded view of region near 1.86 GeV/c^2 in $K^+\pi^-$ invariant mass distributions taken with 10.5 GeV/c π^- and third spectrometer arm in trigger. Variables are as described in text. Only those events with a Q value consistent with the value measured at SPEAR (5.6 MeV) have been retained.

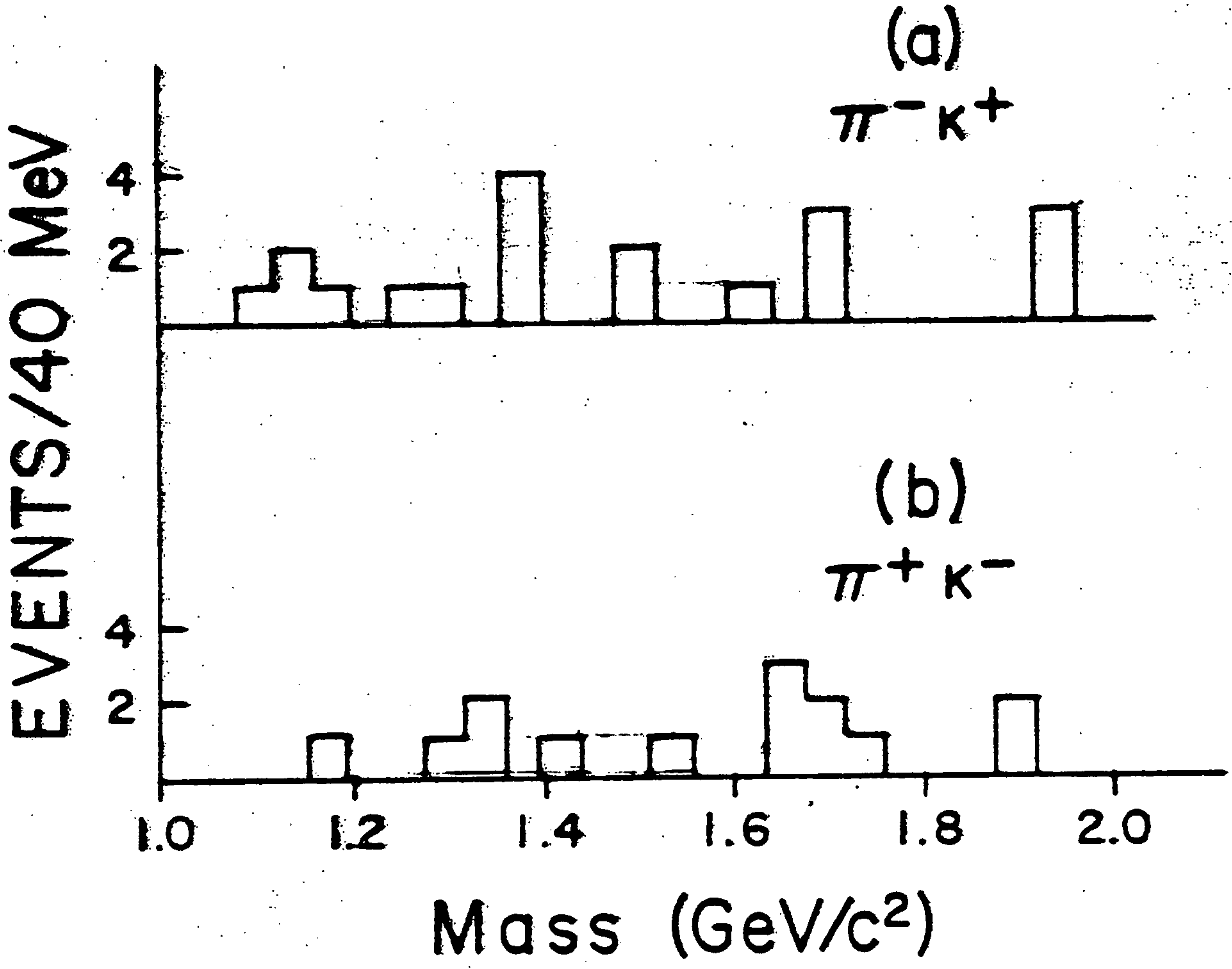

Figure IX-6: $K^+\pi^-$ and $K^-\pi^+$ invariant mass distributions for data taken with incomming 8.5 Ge/c anti-protons and third arm tagging. Only those events with Q value consistent with the value measured at SPEAR (5.6 MeV) have been retained.

$$\sigma\ (\bar{p}\ N \rightarrow D^{*-} + X)*B_{D^{*-} \rightarrow \pi^- D}\ *B_{\bar{D}^0 \rightarrow K^+ -} \leq .8\ \text{ub}$$

If we assume that there are $3\bar{D}^0$'s for every D^{*-} we have:

$$\sigma\ (\bar{P}N \rightarrow \bar{D}^0 + X)\ B_{D \rightarrow K\pi} \leq 2.4\ \text{ub}$$

The limit here is roughly the same as the one quoted in Chapter VIII for the data collected without the third arm. This is because only one third of the data taken at 8.5 GeV/c included the third arm tagging information.

Comparing the pion and proton data, we note that while a 3 standard deviation effect is present in the anti-proton data (Figure VIII-10), the data taken with incoming pions (which has a much better sensitivity) shows no enhancement. It is important to remember, however, that if the mass of the Λ^+_c differs by more than ± 300 MeV/c^2 from the assumed value (2.26 GeV/c^2) we would not expect to see a signal in the pion data because the acceptance for that case is smaller by an order of magnitude.

TABLE IX-1. CROSS SECTION LIMITS

BEAM MOMENTUM	8.0-8.8 GeV/c	10.5 GeV/c
PROCESS	$\overline{P}N \to D^{*-} + X$	$\pi^- N \to D^{*-} + X$
TARGET	33 gm/cm^2	33 gm/cm^2
INCIDENT FLUX	5×10^{10}	2.9×10^{12}
SENSITIVITY/EVENT (cm^2/neucleon)[a]	16×10^{-32}	2×10^{-33}
$\text{EVENTS}_{K^+ \pi^-}$	0 ± 5	8 ± 8
$\sigma(D^{*-}) * B_{D^{*-} \to \pi \overline{D}^o} * B_{\overline{D}^o \to K^+ \pi^-}$	≤ 800 nb	16 ± 16 nb

---

[a] Sensitivity includes efficiency of detecting final state K and a correction (.6) for absorption of the final state $K\pi\pi$ system in target.

TABLE XI-2 : CROSS SECTION LIMITS

BEAM MOMENTUM	10.5 GeV/c
PROCESS	$\pi^- N \rightarrow D^{*-} + X$
TARGET	33 gm/cm^2 C
INCIDENT FLUX	2.9×10^{12}
SENSITIVITY/EVENT (cm^2/nucleon)	3.3×10^{-33}
EVENTS (5σ in 20 MeV)	
$K^+ \pi^-$	22
σB	
$K^+ \pi^-$	75 nb

X. CONCLUSIONS

We have reported here the results of a search for charmed mesons produced in antiproton interactions near threshold. The limits quoted here for the process:

$$\bar{P}\,N \rightarrow D^o\,(\bar{D}^o) + X$$

$$D \rightarrow K\pi$$

$$\sigma B = 780 \pm 300 \text{ nb}$$

are comparable to the best limits for the equivalent process in proton interactions[31]:

$$pp \rightarrow D + X$$

$$D \rightarrow K\pi$$

$$\sigma B \cong 100 - 200 \text{ nb}$$

Furthermore, if we assume that each of the processes

$$\begin{aligned} \bar{p}N &\rightarrow D^o + \bar{D}^o \\ &\rightarrow D^o + \bar{D}^* \\ &\rightarrow D^* + \bar{D}^o \\ &\rightarrow D^* + \bar{D}^* \end{aligned}$$

contribute equally to the signal seen here, then the limit for any one of these processes is 190 ± 80 nb.

If we assume, for the moment, that this signal is real (and can be completely attributed to $\bar{p}N \rightarrow D\bar{D}$) we obtain for the total cross-section:

$$\sigma\ (\bar{p}N \rightarrow D\bar{D}) \cong 40\ \mu b$$

where we have assumed a branching ratio of $D \rightarrow K\pi$ of 2%. This cross section is higher by two orders of magnitude from the theoretical estimates of Chapter III. A new experiment with a factor of 10 better sensitivity should determine whether this signal is real.

The technique described here to observe the D^{*-} should be a propitious mechanism for studying charm production at all energies. As we noted earlier, evidence for the production of charmed baryons is still missing. It may be possible to observe charmed baryons via the cascade decay:

$$\begin{tikzcd}[column sep=small] \Lambda_c^{++} \arrow[r] & \pi^+ + \Lambda_c^+ \arrow[d, to path={|- (\tikztotarget)}] & \\ & & \Lambda\ \pi^+\ \pi^+\ \pi^- \end{tikzcd}$$

Yet even before the lowest lying charmed states have been filled in, there is increasing evidence that four quarks are not enough. Recent experiments at SLAC,[26] confirmed at SPEAR[27] and DORIS[28] indicated the existence of a new heavy lepton. If one wishes to retain the notions of quark-lepton symmetry which motivated the introduction of charm, we must admit another quark.

The departure of $R = \dfrac{\sigma\,(\nu\, p \rightarrow \mu^- + x)}{\sigma\,(\bar{\nu}\, p \rightarrow \mu^+ + x)}$ from the value (~3)[29] predicted by the four quark model is further evidence for more quarks. Here, however, the data is unclear and further results are required[30].

Whatever the case, it is clear that hadron spectroscopy is being pushed into the background to be replaced by the new quark spectroscopy.

REFERENCES

1. S. Glashow, J. Iliopoulos and L. Maiani, Phys. Rev. D2. 1285, (1970).

2. J. Aubert, et al., Phys. Rev. Lett., 33, 1404, (1974).

3. J.A. Augustin, et al., Phys. Rev. Lett., 33, 1406, (1974).

4. G. Goldhaber, et al., Phys. Rev. Lett., 37, 255, (1976).

5. I. Peruzzi, et al., Phys. Rev. Lett., 37, 569, (1976).

6. G.J. Feldmann, et al., Phys. Rev. Lett., 38, 1313, (1977).

7. B. Knapp, et al., Phys. Rev. Lett., 37, 882, (1976).

8. E. Cazzoli, et al., Phys. Rev. Lett., 34, 1125, (1975).

9. Z. Maki, Prog. Theo. Physics, 31, 141 (1964).

10. S. Glashow, "Charm is Not Enough", Talk presented at 5th International Conference on Experimental Meson Spectroscopy N.W. University (1977).

11. B. Richter, Review of Mod. Phys., 49, 251, (1977).

12. M. Gaillard, B. Lee, and J. Rosner, Rev. of Mod. Phys., 47 277, (1975).

13. J. Bransen, et al., Phys. Rev. Lett., 38, 1334, (1977).

14. See, for example, K. Stanfield, "Charm Searches in Hadron-Induced Interactions," Rapporteurs talk presented at Meeting of Particles and Fields at Brookhaven National Laboratory, October, 1977.

15. J. Gaillard and M. Bourquin, "Simple Phenomenological Description of Hadron Production," CERN preprint (1976), (Submitted to Nuclear Physics).

16. H. Lipkin, Physics Letters, 60B, 371, (1976).

17. D. Sivers, Nuclear Physics, 106B, 95, (1976).

18. P. Landshoff and A. Donnachie, Nuclear Physics, 112B, 233, (1976).

19. G. Feldman, SLAC, private communications.

20. V. Fitch, "A Broad Band Focusing Cherenkov Counter," Princeton University preprint, (1975).

21. U. Becker, Phys. Rev. Lett., 38, 140C, (1977).

22. Val Fitch

23. D. Cheng, et al., Nuc. Instr. and Meth., 117, 157 (1974).

24. P. Surko, Princeton University, private communication.

25. See, for example, G. Charapak, et al., Nucl. Instr. and Meth., 99, 279, (1972).

25a. David Newman, Ph.D. Thesis, (unpublished), Princeton University, (1975).

26. M. Perl, et al., Phys. Rev. Lett., 35, 1489, (1975).

27. H. Cavalli-Sforza, et al., Phys. Rev. Lett., 36, 558 (1976).

28. J. Burmester, et al., "Evidence for Heavy Leptons from Anomalous Muon Production in e^+e^- Annihilation," DESY preprint, (1976).

29. A. Benvenuti, et al., Phys. Rev. Lett., 37, 189, (1976).

30. B. Barish, et al., Phys. Rev. Lett., 35, 416 (1975).

31. J. Aubert, et al., Phys. Rev. Lett., 35, 416, (1975). The authors report cross-section limits only for masses $\gtrsim 2.3$ Gev/c^2 and assume a production mechanism with a $P_\perp$ dependence proportional to $e^{-5P_\perp}$, which is not appropriate to masses on the order of 2 Gev/c^2. The value quoted here is the result of Aubert, et al., for $M_D = 2.3$ Gev/c^2 multiplied by a factor of ~ 50 to account for the lower mass and flatter ($\sim e^{-1.5 P_\perp}$) dependence of D production. See Reference 14.

32. Particle data Group, $\overline{N}N$ and $\overline{N}D$ Interactions - A Compilation. (LBL-58), 1972.

Particle Data Group, NN and ND Interactions (above .5 Gev/c) - A Compilation. (UCRL-200000 NN), (1970).

33. A. De Rujula, et al., Phys. Rev. Lett., 37, 785C (1976).

APPENDIX I. THE WATER CHERENKOV COUNTER

For the ideal Cherenkov counter of the type used in this experiment the curve describing the phototube mask is given by:

$$R(\theta) = \frac{R_1 + R_2}{2} + \frac{R_2 - R_1}{\pi} \sin^{-1}\left(\frac{2M\theta}{\pi} - 1\right) \qquad (1)$$

where R_1 and R_2 are the maximum and minimum diameters of the pattern and 2M is the number of petals. The pattern in the Cherenkov counter used in this experiment was separated into individual petals for mechanical reasons. This does not effect the results calculated here.

The amount of light falling in the outer ring is proportional to that fraction of the circumference of the Cherenkov ring enclosed by the outer pattern. If we define r and ϕ' as in Figure A-1 then

$$r\phi' = KN_+ \qquad (2)$$

where K is a constant and N_+ is the number of photoelectrons in one petal of the outer ring. Similarly:

$$r\left(\frac{\pi}{M} - \phi'\right) = KN_- \qquad (3)$$

subtracting (2) from (3)

$$r\left(2\phi' - \frac{\pi}{M}\right) = K(N_+ - N_-)$$

or

$$\phi' = \frac{K(N_+ - N_-)}{2r} + \frac{\pi}{2M}$$

Substituting into equation (1)

$$r = \frac{R_1 + R_2}{2} + \frac{R_2 - R_1}{\pi} \sin^{-1} \left(\frac{2M\phi'}{\pi} - 1\right)$$

$$= \frac{R_1 + R_2}{2} + \frac{R_2 - R_1}{\pi} \sin^{-1} \left(\frac{2MK\,(N_+ - N_-)}{2\pi r}\right)$$

Now

$$2\pi r = KM\,(N_+ + N_-) = K(N_o + N_I)$$

and we have finally:

$$r = \frac{R_1 + R_2}{2} + \frac{R_2 - R_1}{2} \sin^{-1} \Delta = k_1 + k_2 \sin^{-1} \Delta \qquad (4)$$

where k_1 and k_2 are constants, and $\Delta = (N_0 - N_I)/(N_0 + N_I)$.

We can use this relation to calculate the relative error in the measurement of the Cherenkov radius:

$$\delta r = \frac{k_2\ \delta\ \Delta}{\sqrt{1 - \Delta^2}}$$

$$\delta\Delta = \frac{2N_{I+}\ \delta N_o - 2N_o\ \delta N_I}{(N_o + N_I)^2}$$

Recall that $k_2 = (R_2 - R_1)/\pi$. Hence we have

$$\frac{\delta r}{R_2 - R_1} = \frac{1}{\pi\ \sqrt{N}}$$

where $N = N_o + N_I$.

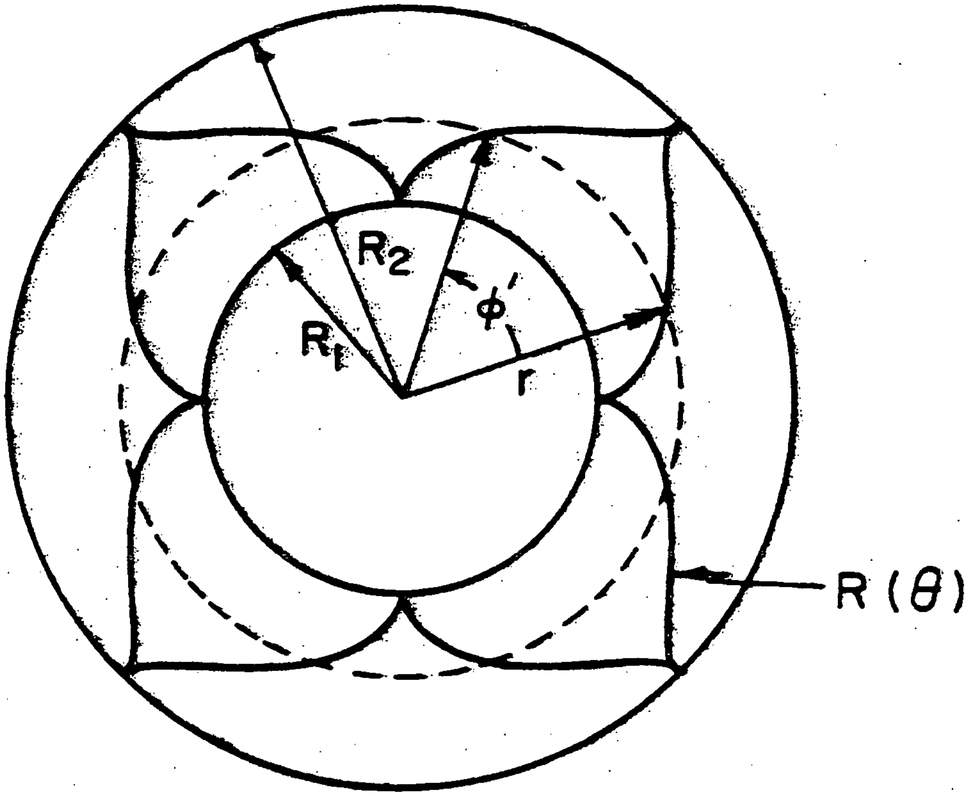

Figures A1 and A2: Definition of variables used in discussion of water Cherenkov counter.

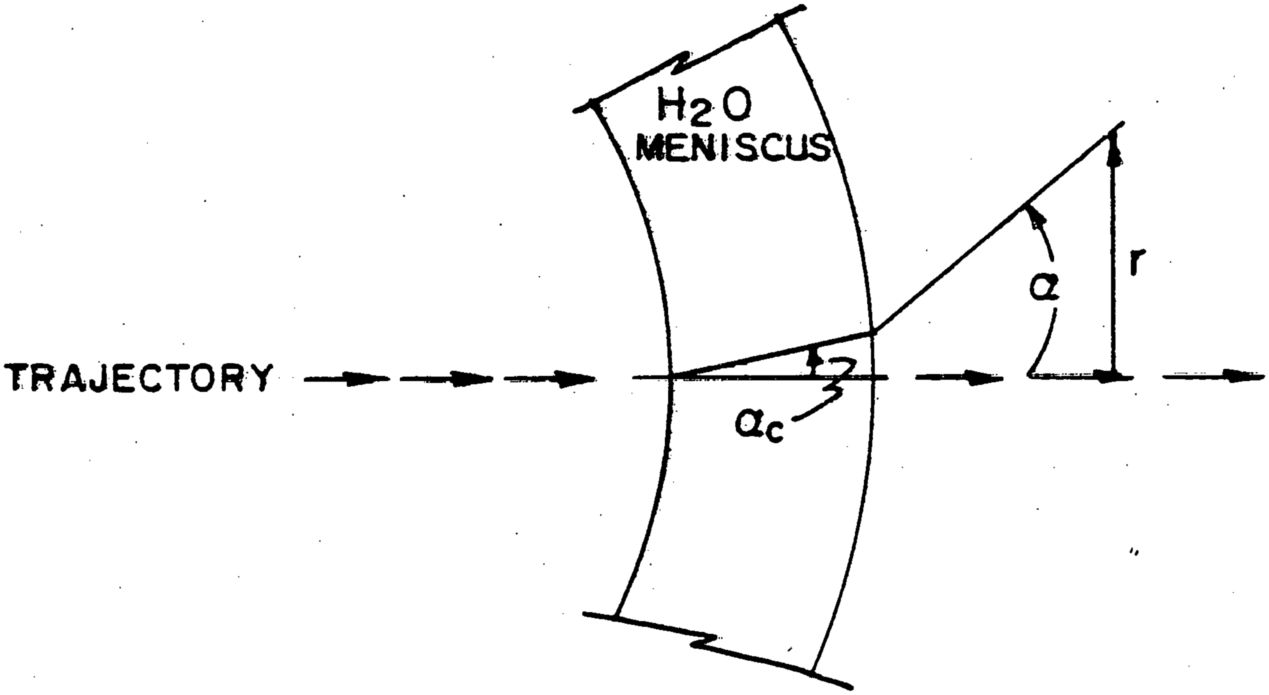

Equation (3) is also the starting point for deriving the relation between Δ and M/P, where M is the mass of the incident particle and P its momentum. Refering to Figure A-2 we have

$$r \cong d \tan\alpha \tag{4}$$

and

$$\sin\alpha = n \sin\alpha_c \tag{5}$$

where α_c is the Cherenkov angle, d is a constant and n is the index of refraction of water ($n = 1.33$). Now:

$$\cos \alpha_c = \frac{1}{n\beta} \cong \frac{1}{n} (1 + \frac{1}{2} M^2/p^2)$$

$$\sin^2\alpha_c = 1 - \cos^2\alpha_c = 1 - \frac{1}{n^2} (1 + \frac{M^2}{p^2})$$

from (4) and (5)

$$r = \frac{dn \sin\alpha_c}{\sqrt{1 - n^2 \sin^2\alpha_c}}$$

But $1 - n^2 \sin^2\alpha_c = 1 - n^2 (1 - \frac{1}{n^2} (1 + \frac{M^2}{p^2}))$

$$\cong .3 + M^2/p^2$$

We now use the approximation:

$$\sqrt{.3 + \frac{M^2}{p^2}} \cong \sqrt{.3} \quad (1 + \frac{M^2}{.6\ p^2}) \qquad \text{for} \quad M/p < \frac{1}{3}$$

also

$$\sin \alpha_c \cong .4 \left(1 - \frac{M^2}{.8n^2p^2}\right)$$

Hence

$$r = \frac{dn \sin\alpha_c}{\sqrt{1 - n^2 \sin^2\alpha_c}} \simeq C_1 + C_2 \; M^2/p^2$$

or since:

$$r = k_1 + k_2 \sin^{-1}\Delta$$

this implies

$$\Delta = \sin^{-1} (k'_1 + k'_2 \; M^2/p^2).$$

APPENDIX II: MASS RESOLUTION

We begin this calculation with the approximate expression for the invarient mass of the two body system observed in the spectrometer:

$$M^2 = M_1{}^2 + M^2{}_2 + 2\ P_1P_2\ (1 - \cos\theta) + \frac{P_2}{P_1}\ M_1{}^2 + \frac{P_1}{P_2} M_2{}^2$$

Differentiating we find:

$$2M\delta M = 2\ (1-\cos\theta)\ (\delta P_1 P_2 + \delta P_2 P_1) + \frac{\delta P_2 M_1{}^2}{P_1} - \delta P_1{}^2 M_1{}^2\ \frac{P_2}{P_1{}^2}$$

$$+ \frac{\delta P_1}{P_2}\ M_2{}^2 - \delta P_2 M_2{}^2\ \frac{P_1}{P_2{}^2} + 2\ P_1 P_2\ \sin\theta\ \delta\theta .$$

In general it is true that $M_2{}^2 << M_1{}^2$. Substituting this into the above expression we find:

$$2M\delta M = \delta P_1\ (2\ (1-\cos\theta)\ P_2 - \frac{P_2}{P_1} M_1{}^2) + \delta P_2\ (\ 2(1-\cos\theta)\ P_1 + \frac{M_1{}^2}{P_1}\ )$$

$$+2\ P_1 P_2\ \sin\theta\ \delta\theta$$

To find the rms error in M, these three terms must be added in quadrature:

$$2M\delta M = \Bigg[\delta P_1^{\,2} \{4\ (1-\cos\theta)^2\ P_2^{\,2} - 4\ (1-\cos\theta)\ \frac{P_2^{\,2}}{P_1^{\,2}}\ M_1^{\,2}\} + \delta P_2^{\,2} \{4\ (1-\cos\theta)^2 P_1^{\,2} + 4\ (1-\cos\theta)\ \frac{P_1^{\,2}}{P_2^{\,2}}\ M_2^{\,2}\} + 4\delta\theta^2\ P_1^{\,2}\ P_2^{\,2}\ \sin^2\theta \Bigg]^{1/2}$$

where terms on the order of $M_1^{\ 4}/P_1^{\,2}$ have been neglected. For our case it is safe to assume that $P_1 = P_2 \equiv P$ and $\delta P_1 = \delta P_2 \equiv \delta P$. Substituting this into the above expression and rearranging terms we find:

$$2M\delta M = \Big[8\delta P^2\ (1-\cos\theta)^2\ P^2 + P^4 4\sin^2\theta\delta\theta^2 \Big]^{1/2} .$$

The error in θ is most easily determined if we use polar coordinates with the origin at the target and $\theta = 0$ along the +z axis, ie.: $\vec{P}_1 = (P_1, \theta_1, \phi_1)$; $\vec{P}_2 = (P_2, \theta_2, \phi_2)$.

$$\cos\theta = \sin\theta_1\ \sin\theta_2\ \cos(\phi_1 - \phi_2) + \cos\theta_1\ \cos\theta_2$$

$$\cos\theta \cong \cos\ (\theta_1 + \theta_2)$$

$$\sin\theta^2\delta\theta^2 = \sin\ (\theta_1 + \theta_2)^2\ (\delta\theta_1^{\,2} + \delta\theta_2^{\,2}) = \sin^2\theta\ (\delta\theta^2_{\ 1} + \delta\theta_2)^2$$

where we have used $\cos\ (\phi_1 - \phi_2) \cong -1$. Since we have assumed that $P_1 = P_2$ it is also true that $\delta\theta_1 \cong \delta\theta_2$. Our expression for the error in the mass is then:

$$M\delta M = \Big[2\delta P^2\ (1-\cos\theta)^2\ \ P^2 + 2\ P^4\ \sin^2\theta\ \delta\theta^2 \Big] .$$

To calculate the error δP we use:

$$P = \frac{P_\perp}{\sin\alpha_1 - \sin\alpha_2} \quad \Rightarrow \quad \delta P = \frac{P^2}{P_\perp}\left(\cos^2\alpha_1\ \delta\alpha_1^{\ 2} + \cos^2\alpha_2\ \delta\alpha^2\right)$$

$$\cong \frac{P^2}{P_\perp}\ \left(\delta\alpha_1^{\ 2} + \delta\alpha_2^{\ 2}\right)$$

where $(\alpha_1 + \alpha_2)$ is the angle of deflection in the magnet. To estimate the errors in these angles we use the deviation between the measured and calculated positions in the drift chambers divided by their separation:

$$\delta\alpha \cong \frac{.030''}{39''} = .8 \times 10^{-3} \cong \delta\alpha_1 \cong \delta\alpha_2$$

Since the $P_\perp$ of the magnet is roughly 0.45 Mev/c, we have:

$$\delta P^2 = .7 \times 10^{-5}\ P^4$$

The opening angle of the spectrometer is 36°; hence $\sin\theta = 0.2$. Also, the rms multiple scattering angle in the target is given by:

$$\delta\theta = \frac{.015}{P}\ \sqrt{\frac{L}{L_{rad}}}$$

Since the decay products exist at roughly 18°, they traverse approximately 4.1 cm of target material (carbon; $L_{rad} = 44$ gm/cm^2). Calculating from the previous equation we find:

$$\delta\theta = \frac{.015}{P}\ (.45) = \frac{6.8 \times 10^{-3}}{P}$$

Substituting all of these values into the equation for δM we obtain:

$$M\delta M = \left[5.6 \times 10^{-7} P^6 + 4.6 \times 10^{-5} P^2\right]^{1/2}$$

or for $M = 1.86$ Gev/c^2 and $P = 2.86$ Gev/c we have:

$$\frac{\delta M}{M} = \frac{27 \times 10^{-3}}{3.5} \cong 1\% \quad .$$

APPENDIX III: MASS DISTRIBUTIONS

On the following pages we list the two-body invariant mass distributions for the data collected during this experiment. Other than the usual particle idendification cuts, no restrictions have been placed on the data. In several cases charge-conjugate final states have been added together. The first and last non-zero numbers in the mass distributions can contain 'overflow' events (events with too high or too low a mass) and care should be exercised when using these numbers.

••••••••••••••••••••••••••••• MASS DISTRIBUTIONS FOR 8.5 GEV/C PBAR-N DATA •••••••••••••••••••••••••••••

MASS GEV	PI+PI-	PI-PI- PI+PI+	PI+ K-	PI- K+	PI+ K+	PI- K-	PI+ P-	PI- P+	PI+ P+	PI- P-
.820	2883	1599	0	0	0	0	0	0	0	0
.860	1332	756	0	0	0	0	0	0	0	0
.900	1573	1044	0	0	0	0	0	0	0	0
.940	1955	1206	0	0	0	0	0	0	0	0
.980	2165	1383	0	0	0	0	0	0	0	0
1.020	2324	1456	98	227	138	61	0	0	0	0
1.060	2363	1606	84	158	112	61	0	0	0	0
1.100	2324	1538	102	224	147	75	0	0	0	0
1.140	2385	1527	171	309	189	113	0	0	0	0
1.180	2377	1442	222	415	241	174	0	0	0	0
1.220	2361	1319	274	438	294	204	0	0	0	0
1.260	2168	1212	388	496	346	219	0	0	0	0
1.300	2005	1168	317	513	301	247	0	0	0	0
1.340	1740	1095	352	534	317	253	6	51	31	2
1.380	1455	975	374	599	266	265	28	155	136	21
1.420	1357	841	383	590	262	230	46	299	212	32
1.460	1213	764	373	534	277	226	61	438	280	48
1.500	1097	656	288	495	243	261	119	776	520	86
1.540	890	566	257	460	221	186	203	1105	789	143
1.580	873	473	228	446	199	192	218	1409	927	176
1.620	769	418	213	387	202	199	254	1591	988	184
1.660	642	333	202	374	132	142	294	1699	964	210
1.700	608	296	171	324	130	124	286	1542	935	224
1.740	519	262	161	329	124	133	268	1471	919	205
1.780	422	254	136	244	100	124	234	1404	769	213
1.820	367	184	108	219	87	88	228	1342	743	195
1.860	347	181	126	224	64	79	207	1274	633	172
1.900	268	158	103	200	61	72	206	1173	521	149
1.940	243	108	69	166	62	47	186	1010	494	138
1.980	228	95	74	144	27	58	158	959	420	155
2.020	185	65	61	121	37	47	160	831	418	116
2.060	159	71	56	123	43	30	118	731	323	104
2.100	168	72	41	94	18	35	117	741	308	92
2.140	155	52	39	95	17	31	117	635	229	79
2.180	116	35	44	78	13	25	102	575	172	73
2.220	121	37	33	73	17	18	76	460	144	48
2.260	111	29	30	54	15	24	90	423	134	41
2.300	84	24	19	45	10	18	40	358	89	40
2.340	78	22	15	44	10	11	54	302	86	42
2.380	62	18	14	34	14	9	42	285	72	32
2.420	56	26	11	33	7	8	30	226	49	28
2.460	48	20	12	26	6	13	44	171	48	27
2.500	29	13	7	19	5	10	20	143	34	22
2.540	27	17	7	20	7	6	21	118	23	14
2.580	16	17	2	15	5	7	17	106	16	15
2.620	19	18	11	11	7	4	22	77	17	18
2.660	13	18	5	9	8	6	9	85	13	16
2.700	12	9	3	4	6	5	12	58	23	11
2.740	12	11	3	9	8	3	9	41	14	8
2.780	208	226	2	4	4	5	9	32	15	4
2.820	0	0	3	5	1	3	7	29	19	7
.860	0	0	4	4	1	0	8	27	13	13
.900	0	0	3	1	6	5	6	23	11	10
.940	0	0	1	1	5	4	8	13	9	5
.980	0	0	47	76	62	67	3	15	9	6
.020	0	0	0	0	0	0	4	10	13	8
.060	0	0	0	0	0	0	2	17	11	7
.100	0	0	0	0	0	0	5	10	14	5
.140	0	0	0	0	0	0	5	6	6	12
.180	0	0	0	0	0	0	92	207	173	128

********** MASS DISTRIBUTIONS FOR 8.5 GEV/C PBAR-N DATA **********

MASS GEV	K+ K-	K- K- K+ K+	K+ P-	K+ P+ K- P-	P+ P-	P- P- P+ P+
1.025	0	0	0	0	0	0
1.075	0	0	0	0	0	0
1.125	1	1	0	0	0	0
1.175	6	5	0	0	0	0
1.225	4	8	0	0	0	0
1.275	11	9	0	0	0	0
1.325	31	23	0	0	0	0
1.375	47	33	0	0	0	0
1.425	75	46	0	0	0	0
1.475	90	59	0	0	0	0
1.525	115	57	0	1	0	0
1.575	108	64	5	26	0	0
1.625	128	63	12	54	0	0
1.675	121	66	33	95	0	0
1.725	115	76	49	186	0	0
1.775	109	66	89	212	0	0
1.825	124	37	83	259	0	0
1.875	78	52	104	261	0	0
1.925	67	36	112	314	0	0
1.975	75	27	111	298	0	0
2.025	59	26	94	269	152	306
2.075	42	17	97	258	266	464
2.125	40	11	94	213	308	544
2.175	35	19	82	168	402	460
2.225	31	14	77	144	407	392
2.275	37	7	66	95	370	289
2.325	25	6	41	81	354	260
2.375	20	5	49	66	262	181
2.425	17	6	35	49	258	155
2.475	10	4	26	34	231	108
2.525	10	2	22	35	167	84
2.575	8	0	26	20	171	60
2.625	7	2	15	15	126	45
2.675	4	2	25	15	94	28
2.725	4	1	13	13	66	34
2.775	0	3	11	11	60	19
2.825	2	3	4	14	43	14
2.875	2	1	5	11	52	17
2.925	1	0	2	5	39	13
2.975	1	1	8	6	24	8
3.025	1	2	3	5	16	9
3.075	0	3	2	5	11	6
3.125	2	0	2	4	11	6
3.175	0	0	1	8	8	8
3.225	1	1	2	7	11	1
3.275	3	0	3	3	12	5
3.325	2	0	2	1	7	7
3.375	0	0	4	2	9	3
3.425	0	0	2	3	6	3
3.475	13	12	0	1	3	1
3.525	0	0	2	2	5	3
3.575	0	0	0	3	2	0
3.625	0	0	1	3	5	6
3.675	0	0	4	8	6	3
3.725	0	0	0	3	5	4
3.775	0	0	0	1	4	7
3.825	0	0	2	7	6	2
3.875	0	0	0	0	3	2
3.925	0	0	1	3	5	3
3.975	0	0	20	37	2	2
4.025	0	0	0	0	1	3
4.075	0	0	0	0	4	2
4.125	0	0	0	0	4	6
4.175	0	0	0	0	2	1
4.225	0	0	0	0	3	1
4.275	0	0	0	0	0	3
4.325	0	0	0	0	3	2
4.375	0	0	0	0	5	2
4.425	0	0	0	0	4	3
4.475	0	0	0	0	52	31

********************** MASS DISTRIBUTIONS FOR 12.4 GEV/C PBAR-N DATA **********************************

S V	PI+PI-	PI+PI+	PI+ K-	PI- K+	PI+ K+	PI- K-	PI+ P-	PI- F+	PI+ P+	PI- P-
0	288	150	0	0	0	0	0	0	0	0
0	269	179	0	0	0	0	0	0	0	0
0	436	803	0	0	0	0	0	0	0	0
0	571	373	0	0	0	0	0	0	0	0
0	461	500	0	0	0	0	0	0	0	0
0	649	504	7	8	4	2	0	0	0	0
0	711	549	6	22	13	6	0	0	0	0
0	713	542	42	33	14	20	0	0	0	0
0	741	546	37	107	65	40	0	0	0	0
0	687	478	64	107	72	43	0	0	0	0
0	689	473	65	99	76	58	0	0	0	0
0	631	485	70	106	96	75	0	0	0	0
0	564	430	103	126	105	79	0	0	0	0
0	489	406	122	134	110	71	0	0	0	0
0	451	324	156	142	114	74	0	0	0	0
0	404	270	84	129	103	70	2	0	0	0
0	325	250	115	127	125	66	8	12	13	0
0	300	193	92	143	113	75	18	60	36	15
0	265	208	120	121	94	70	44	89	57	18
0	252	187	80	95	81	74	43	149	123	37
0	200	148	87	72	65	59	41	144	119	32
0	160	133	93	95	61	48	54	176	120	60
0	159	106	77	70	53	55	68	145	126	32
0	127	93	71	59	45	31	60	146	124	31
0	75	72	61	46	43	33	54	125	136	29
0	74	75	48	64	50	32	65	134	114	45
0	73	62	36	36	32	32	51	122	110	31
0	79	41	16	36	26	12	73	133	92	33
0	57	47	16	18	25	28	72	93	90	31
0	53	40	23	37	12	25	38	97	79	17
0	42	33	27	26	19	20	41	87	68	15
0	38	28	24	24	14	15	36	95	66	32
0	38	19	19	24	17	5	37	55	47	21
0	22	24	10	18	5	15	18	45	38	17
0	37	22	13	14	15	8	7	50	36	16
0	9	8	15	19	2	4	18	44	32	16
0	15	16	3	16	8	16	17	37	27	9
0	17	17	8	11	0	4	16	31	21	8
0	17	7	9	12	11	2	25	7	17	5
0	14	4	6	4	2	3	17	11	8	16
0	6	7	9	7	9	6	18	13	15	4
0	10	12	8	4	1	1	14	7	7	4
0	4	5	5	8	0	4	14	7	7	3
0	7	6	4	7	6	7	12	6	9	3
0	5	4	0	2	4	1	12	4	3	3
0	0	9	2	4	4	0	11	3	15	1
0	9	10	3	4	6	1	6	2	3	1
0	3	1	1	1	3	6	0	7	1	4
0	6	1	5	2	2	0	6	4	4	5
0	0	0	1	0	0	5	5	6	1	3
0	0	0	0	1	0	5	5	3	5	2
0	0	0	2	1	2	0	3	3	4	2
0	0	0	0	4	1	0	3	1	4	1
0	0	0	2	1	0	1	0	3	5	0
0	0	0	0	0	0	0	1	2	0	3
0	0	0	0	0	0	0	2	2	7	0
0	0	0	0	0	0	0	0	1	1	2
0	0	0	0	0	0	0	5	2	3	0
0	0	0	0	0	0	0	6	3	0	3
0	0	0	0	0	0	0	1	0	0	0
0	0	0	0	0	0	0	4	0	2	0
0	0	0	0	0	0	0	0	3	2	0

```
*************** MASS DISTRIBUTIONS FOR 12.4 GEV/C PBAR-N DATA ***************

  MASS              K-  K-             K+  P+     MASS                P-  P-
   GEV    K+  K-    K+  K+    K+  P-   K-  P-      GEV     P+  P-     P+  P+
=======  =======  =======  =======  =======   ======   =======   =======

 1.220       2        0        0        0
 1.260       0        0        0        0
 1.300       0        2        0        0
 1.340       7        2        0        0
 1.380       8       13        0        0
 1.420       6       13        0        0
 1.460      29        7        0        0
 1.500      16       11        0        0
 1.540      19       10        0        0
 1.580      13       10        0        0
 1.620      12       15        0        0
 1.660      17       20        6        3
 1.700      18       12        1        5
 1.740      25       15       20        4
 1.780      19       11       27       21
 1.820      20        6       19       13
 1.860      20       16       36       27
 1.900      13       10       43       28
 1.940      12        9       40       22
 1.980       7       15       36       23
 2.020       3        5       31       21
 2.060       8        4       30       13
 2.100      22        5       21       28
 2.140       9       10       19       13
 2.180      21        8       27       26
 2.220       3        3       14       14     2.025        4        5
 2.260       7        1       26       16     2.075       21       11
 2.300       9        3       15       17     2.125       24       15
 2.340       6        7       19        5     2.175       30       19
 2.380       6        2       24        2     2.225       30       25
 2.420       8        5       19        6     2.275       25       13
 2.460       5        1       12       11     2.325       11       17
 2.500       4        2        9        3     2.375       26       10
 2.540       8        0       16       10     2.425       16       13
 2.580       2        2        8        8     2.475       15       11
 2.620       2        3       13       10     2.525        7        9
 2.660       2        0        9        4     2.575        8        6
 2.700       8        0       10        4     2.625       10        7
 2.740       2        3        3        0     2.675       15        3
 2.780       2        1        6        0     2.725        9        9
 2.820       0        1        6        5     2.775        6        2
 2.860       4        0        3        2     2.875        0        1
 2.900       2        0       12        0     2.875        6        4
 2.940       0        1       11        4     2.925        5        0
 2.980       0        3        2        5     2.975        3        0
 3.020       0        0        0        8     3.025        5        0
 3.060       0        0        1        0     3.075        1        2
 3.100       0        0        2        2     3.125       11        3
 3.140       0        1        1        1     3.175        2        2
 3.180       0        0        4        0     3.375        2        2
 3.220       0        0        2        0     3.275        0        2
 3.260       0        0        3        0     3.325        0        0
 3.330       0        0        2        2     3.375        4        0
 3.340       0        0        0        0     3.425        0        0
 3.380       0        0        2        0     3.475        2        2
 3.420       0        0        0        0     3.525        0        0
 3.460       0        0        2        0     3.575        0        2
 3.500       0        0        0        2     3.625        4        1
                                              3.675        0        0
                                              3.725        1        0
                                              3.775        0        0
                                              3.825        0        0
                                              3.875        0        0
                                              3.925        0        1
                                              3.975        1        0
                                              4.025        0        0
```

```
*****************************  MASS DISTRIBUTIONS FOR 15 GEV/C PBAR-N DATA   *****************************

  MASS               PI-PI-
   GEV    PI+PI-     PI+PI+    PI+ K-    PI- K+    PI+ K+    PI- K-    PI+ P-    PI- P+    PI+ P+    PI- P-
=======  ========   ========  ========  ========  ========  ========  ========  ========  ========  ========

   .820      98        62         0         0         0         0         0         0         0         0
   .860     124        95         0         0         0         0         0         0         0         0
   .900     199       164         0         0         0         0         0         0         0         0
   .940     242       179         0         0         0         0         0         0         0         0
   .980     298       225         0         0         0         0         0         0         0         0
  1.020     317       229         2         4         0         0         0         0         0         0
  1.060     320       274         2         8         6         4         0         0         0         0
  1.100     340       260        11        17        18         3         0         0         0         0
  1.140     321       308        14        40        26        11         0         0         0         0
  1.180     327       278        24        36        28        19         0         0         0         0
  1.220     319       241        39        37        39        15         0         0         0         0
  1.260     299       243        35        43        43        35         0         0         0         0
  1.300     282       215        45        69        43        37         0         0         0         0
  1.340     255       167        47        66        46        27         0         0         0         0
  1.380     207       158        43        66        50        27         0         0         0         0
  1.420     178       133        39        52        47        21         0         0         0         0
  1.460     165       132        44        62        49        28         1         7         4         2
  1.500     144       116        38        44        38        34         9        29        28         2
  1.540     109       105        29        37        31        24        15        76        66         8
  1.580     113       100        28        49        35        26        22        92        82        11
  1.620      90        86        23        48        27        24        34       115       103        15
  1.660      77        62        20        30        31        21        29       114       113        23
  1.700      78        65        20        39        24        16        28       107       116        17
  1.740      65        50        18        33        21        14        28       116        86        15
  1.780      64        39        19        27        26        14        33       100       102        12
  1.820      48        39        16        21         7        14        18       109        95        18
  1.860      45        26        14        20        14        13        23        86        71        13
  1.900      37        31        16         9        14         6        17        80        79        16
  1.940      38        24         9        12         9         9        12        71        51        14
  1.980      41        23         8        11         7         3        19        77        51        12
  2.020      20        11         6        12         9        12        11        59        40         9
  2.060      22        10         4        13         2         3        12        47        49         7
  2.100      19        14         6        16         3         5        12        44        39        10
  2.140      19        10         6         8         2         1        13        45        23         9
  2.180      14         5         5         5         5         3         8        28        23         5
  2.220       9         7         2         7         3         4         6        40        13         8
  2.260       9         6         0         5         1         1         3        26        16         6
  2.300      13         6         6         4         3         2         5        21        19         5
  2.340       8         2         1         1         3         1         4        20        13         3
  2.380       8         2         4         7         4         0         6        16        12         2
  2.420       8         2         3         3         1         0         3        10         7         4
  2.460       3         4         2         3         2         0         4        12         3         3
  2.500       4         3         1         2         1         0         6        10         4         3
  2.540       3         4         0         1         0         1         3        12         8         2
  2.580       5         3         0         2         0         0         2         7        10         0
  2.620       2         4         0         2         2         0         3         3         3         2
  2.660       1         2         1         1         0         0         1         5         5         0
  2.700       4         1         2         0         1         1         3         5         3         3
  2.740       3         2         0         1         0         0         2         6         0         1
  2.780      41        37         0         1         1         1         0         4         1         2
  2.820       0         0         1         0         0         0         0         5         3         3
  2.860       0         0         0         1         1         1         2         2         0         0
  2.900       0         0         0         1         0         1         0         0         1         0
  2.940       0         0         0         1         2         0         0         1         2         0
  2.980       0         0         4        11         8         7         0         0         0         1
  3.020       0         0         0         0         0         0         0         0         1         0
  3.060       0         0         0         0         0         0         1         1         0         2
  3.100       0         0         0         0         0         0         0         2         0         0
  3.140       0         0         0         0         0         0         0         1         0         1
  3.180       0         0         0         0         0         0        10        17        11        12
```

7

```
**********  MASS DISTRIBUTIONS FOR 15 GEV/C PBAR-N DATA     **********

   MASS                  K- K-              K+ P+              P- P-
    GEV       K+ K-      K+ K+     K+ P-    K- P-    P+ P-     P+ P+
  =======   ========   ========  ======== ======== ========  ========


   1.025         0          0         0        0        0         0
   1.075         0          0         0        0        0         0
   1.125         0          0         0        0        0         0
   1.175         0          0         0        0        0         0
   1.225         0          0         0        0        0         0
   1.275         1          1         0        0        0         0
   1.325         4          6         0        0        0         0
   1.375         6          3         0        0        0         0
   1.425         1          4         0        0        0         0
   1.475         9          4         0        0        0         0
   1.525        11          5         0        0        0         0
   1.575        11          7         0        0        0         0
   1.625         9          9         0        0        0         0
   1.675        13          8         5        3        0         0
   1.725        12         10         6       20        0         0
   1.775        11         10         5       19        0         0
   1.825         4          2         6       25        0         0
   1.875        11          3         8       24        0         0
   1.925         7          9         7       30        0         0
   1.975         7          7         4       37        0         0
   2.025         5          2         8       26        6         8
   2.075         4          2         4       27       12        24
   2.125         3          3         5       19       22        37
   2.175         2          1         7       20       16        27
   2.225         2          0         4       18       17        24
   2.275         2          2         5       15       14        24
   2.325         1          1         2       11       22        19
   2.375         0          1         2       12       10        13
   2.425         1          0         3        2       14        10
   2.475         1          1         3        5        7        10
   2.525         0          0         1        4        6         6
   2.575         2          0         1        1        4         6
   2.625         0          0         2        2        5         3
   2.675         0          1         0        1        9         5
   2.725         1          0         1        3        3         1
   2.775         0          0         1        1        3         1
   2.825         0          0         2        2        3         5
   2.875         0          0         0        0        2         4
   2.925         0          0         1        1        3         1
   2.975         1          1         0        0        0         0
   3.025         0          0         0        2        3         2
   3.075         0          0         0        0        3         0
   3.125         0          0         1        1        0         1
   3.175         0          0         0        0        0         1
   3.225         0          0         1        1        0         0
   3.275         0          0         0        0        2         0
   3.325         0          0         0        0        1         0
   3.375         0          0         0        0        0         1
   3.425         0          0         0        0        0         0
   3.475         0          3         0        0        0         1
   3.525         0          0         1        0        0         0
   3.575         0          0         0        0        1         0
   3.625         0          0         0        0        0         0
   3.675         0          0         0        0        0         0
   3.725         0          0         0        2        1         0
   3.775         0          0         0        0        0         0
   3.825         0          0         0        1        0         0
   3.875         0          0         0        1        1         0
   3.925         0          0         0        0        0         0
   3.975         0          0         1        3        0         1
   4.025         0          0         0        0        0         0
   4.075         0          0         0        0        0         0
   4.125         0          0         0        0        0         0
   4.175         0          0         0        0        0         0
   4.225         0          0         0        0        0         0
   4.275         0          0         0        0        0         0
   4.325         0          0         0        0        1         0
   4.375         0          0         0        0        0         0
   4.425         0          0         0        0        0         0
   4.475         0          0         0        0        1         1
```

```
******************************  MASS DISTRIBUTION FOR 10.5 GEV/C PI-N DATA      ******************************

  MASS               PI-PI-
   GEV     PI+PI-    PI+PI+    PI+ K-    PI- K+    PI+ K+    PI- K-    PI+ P-    PI- P+    PI+ P+    PI- P-
=======  ========  ========  ========  ========  ========  ========  ========  ========  ========  ========


   .820       630       331         0         0         0         0         0         0         0         0
   .860       693       448         0         0         0         0         0         0         0         0
   .900       979       664         0         0         0         0         0         0         0         0
   .940      1275       854         0         0         0         0         0         0         0         0
   .980      1488       991         0         0         0         0         0         0         0         0
  1.020      1639      1097         6        33        15         3         0         0         0         0
  1.060      1674      1172        22        84        38        16         0         0         0         0
  1.100      1771      1213        31       151       102        29         0         0         0         0
  1.140      1773      1227        66       215       142        54         0         0         0         0
  1.180      1694      1197       114       299       175        70         0         0         0         0
  1.220      1698      1086       125       386       231       121         0         0         0         0
  1.260      1610      1064       187       421       272       118         0         0         0         0
  1.300      1440       939       212       437       331       159         0         0         0         0
  1.340      1325       911       193       453       284       164         0         0         0         0
  1.380      1147       822       241       498       314       172         0         0         0         0
  1.420      1051       769       198       458       285       163         2         6         1         0
  1.460       958       677       189       474       330       133        13        95        51         1
  1.500       847       594       181       402       234       162        39       474       286        29
  1.540       797       505       151       407       291       143        58       836       528        60
  1.580       641       413       168       362       222       120        83      1197       745        74
  1.620       568       414       127       377       205        99        59      1375       859        72
  1.660       523       345        99       346       197        92        95      1353       922        69
  1.700       435       342        95       292       157        69        90      1421       857        86
  1.740       444       249       103       260       155        76        93      1370       818        59
  1.780       350       229        77       266       156        84        98      1257       760        60
  1.820       303       238        67       213       112        46        86      1255       698        55
  1.860       293       207        76       204       111        44        56      1043       693        64
  1.900       242       171        55       168       114        47        50      1056       601        78
  1.940       206       146        45       150        73        50        56       887       563        47
  1.980       203       111        53       159        87        46        60       799       469        50
  2.020       166       115        37        99        61        31        43       741       413        33
  2.060       140        91        40       116        56        24        39       606       372        30
  2.100       118        76        26       105        50        15        41       583       301        30
  2.140        90        65        26        87        36        25        26       494       297        21
  2.180        96        50        10        72        42        15        25       462       234        21
  2.220        77        56        18        69        31        11        19       372       192        22
  2.260        75        57        18        56        21        15        21       310       165        19
  2.300        66        47        13        43        29        11        21       305       163        16
  2.340        53        39        13        47        29        14        19       268       122        12
  2.380        60        26         6        42        13        17        11       213        97        12
  2.420        46        19         6        36        13         6        10       204        90        11
  2.460        38        22         4        34        12         9        15       130        76        14
  2.500        43        23         8        32        15         5         9       119        74        15
  2.540        22        19         6        27        10         4        14       106        52        12
  2.580        31        19         4        19        12         5         6       109        43        10
  2.620        29        10         6        14         9         4        11        91        29        11
  2.660        21         7         1        13         8         2         8        68        25        10
  2.700        20        12         6        17         4         2        14        58        20         7
  2.740        25         6         3        18         4         1         7        39        26         9
  2.780       288       215         0        10         3         2         6        47        18        13
  2.820         0         0         2         8         5         1         2        33        20         5
  2.860         0         0         1        11         3         5         8        25        13         7
  2.900         0         0         4         9         3         2         5        40        24         6
  2.940         0         0         2        12         4         3         7        29        12         3
  2.980         0         0        52       100        77        61         3        23        13         3
  3.020         0         0         0         0         0         0         2        17         6         6
  3.060         0         0         0         0         0         0         2        15        11        10
  3.100         0         0         0         0         0         0         3        15        14         4
  3.140         0         0         0         0         0         0         2        19         8         4
  3.180         0         0         0         0         0         0        79       231       174       106
```

*********** MASS DISTRIBUTION FOR 10.5 GEV/C PI-N DATA **********

MASS GEV	K+ K-	K- K- K+ K+	K+ P-	K+ P+ K- P-	P+ P-	P- P- P+ P+
1.025	0	0	0	0	0	0
1.075	0	0	0	0	0	0
1.125	0	0	0	0	0	0
1.175	0	0	0	0	0	0
1.225	0	1	0	0	0	0
1.275	3	3	0	0	0	0
1.325	9	10	0	0	0	0
1.375	26	29	0	0	0	0
1.425	37	38	0	0	0	0
1.475	48	49	0	0	0	0
1.525	73	55	0	0	0	0
1.575	100	61	0	0	0	0
1.625	82	70	0	2	0	0
1.675	83	63	3	44	0	0
1.725	76	56	26	118	0	0
1.775	64	42	29	162	0	0
1.825	76	49	31	227	0	0
1.875	52	49	53	235	0	0
1.925	47	36	33	274	0	0
1.975	47	33	33	274	0	0
2.025	39	32	28	280	23	80
2.075	40	24	28	234	110	268
2.125	31	15	37	214	136	383
2.175	26	13	24	176	143	336
2.225	23	13	17	155	120	313
2.275	14	9	19	110	104	238
2.325	15	18	12	97	101	227
2.375	12	8	14	92	92	153
2.425	7	11	18	55	55	130
2.475	7	7	16	54	58	107
2.525	4	4	11	43	38	77
2.575	4	3	15	39	27	83
2.625	7	6	9	29	42	59
2.675	4	1	13	27	21	42
2.725	3	4	5	17	24	32
2.775	1	4	4	16	20	22
2.825	2	1	4	17	15	23
2.875	0	1	3	12	16	16
2.925	2	1	0	16	6	15
2.975	0	1	2	5	9	12
3.025	2	2	1	12	4	6
3.075	3	3	2	8	9	11
3.125	1	1	1	8	7	9
3.175	2	0	0	7	5	3
3.225	3	0	2	4	3	4
3.275	1	0	1	1	6	7
3.325	1	0	2	5	1	4
3.375	0	1	1	7	3	6
3.425	0	1	0	5	4	6
3.475	7	15	2	1	1	7
3.525	0	0	0	1	6	4
3.575	0	0	0	4	3	4
3.625	0	0	0	4	3	1
3.675	0	0	1	5	1	3
3.725	0	0	0	6	2	3
3.775	0	0	1	5	2	4
3.825	0	0	2	3	1	5
3.875	0	0	0	2	2	4
3.925	0	0	1	3	1	3
3.975	0	0	11	36	2	1
4.025	0	0	0	0	5	0
4.075	0	0	0	0	2	1
4.125	0	0	0	0	1	4
4.175	0	0	0	0	1	3
4.225	0	0	0	0	0	3
4.275	0	0	0	0	0	2
4.325	0	0	0	0	1	3
4.375	0	0	0	0	2	2
4.425	0	0	0	0	1	2
4.475	0	0	0	0	26	28

****************************** MASS DISTRIBUTIONS FOR 15 GEV/C PI-N DATA ******************************

MASS GEV	PI+PI-	PI-PI- PI+PI+	PI+ K-	PI- K+	PI+ K+	PI- K-	PI+ P-	PI- P+	PI+ P+	PI- P-
.820	719	200	0	0	0	0	0	0	0	0
.860	976	433	0	0	0	0	0	0	0	0
.900	1643	937	0	0	0	0	0	0	0	0
.940	2301	1538	0	0	0	0	0	0	0	0
.980	2965	2158	0	0	0	0	0	0	0	0
1.020	3559	2502	4	10	3	1	0	0	0	0
1.060	3943	2960	22	64	21	5	0	0	0	0
1.100	4388	3407	47	191	65	47	0	0	0	0
1.140	4699	3512	136	306	161	105	0	0	0	0
1.180	4921	3624	212	529	257	175	0	0	0	0
1.220	4824	3676	282	617	332	247	0	0	0	0
1.260	4780	3639	388	775	442	351	0	0	0	0
1.300	4522	3524	493	912	517	456	0	0	0	0
1.340	4224	3293	572	1062	593	502	0	0	0	0
1.380	3874	3061	626	1109	650	574	0	0	0	0
1.420	3670	2922	669	1148	651	621	0	0	0	0
1.460	3417	2663	612	1110	672	654	1	80	13	3
1.500	2939	2485	666	1160	672	542	26	407	148	9
1.540	2851	2260	618	1073	689	565	63	984	455	53
1.580	2540	2046	613	1044	615	580	98	1558	850	70
1.620	2322	1780	538	976	614	515	105	2008	1054	103
1.660	2065	1633	485	970	603	522	121	2400	1347	138
1.700	1760	1425	476	920	548	405	150	2614	1466	114
1.740	1568	1277	418	835	518	397	138	2609	1588	110
1.780	1455	1167	387	718	499	354	151	2609	1556	140
1.820	1272	1003	342	663	421	322	156	2451	1555	144
1.860	1143	917	310	629	405	299	155	2401	1539	150
1.900	974	791	252	576	417	256	134	2180	1395	168
1.940	889	649	202	532	295	260	131	2145	1316	121
1.980	765	597	192	504	329	214	124	2092	1285	128
2.020	707	545	217	439	248	166	127	1801	1196	112
2.060	606	470	141	389	207	146	124	1682	1019	99
2.100	521	423	135	371	199	130	101	1538	948	81
2.140	505	380	118	319	169	130	86	1338	901	78
2.180	400	305	100	271	156	85	81	1206	756	80
2.220	343	271	90	239	156	81	71	1090	684	84
2.260	302	245	73	247	116	74	73	963	567	58
2.300	274	219	57	189	117	67	54	851	525	58
2.340	234	178	45	171	91	46	61	733	402	52
2.380	203	173	42	160	93	46	49	673	377	51
2.420	189	166	36	135	87	50	55	566	342	43
2.460	153	110	27	122	65	37	28	503	302	26
2.500	137	107	25	103	73	35	40	507	243	30
2.540	124	108	31	110	64	27	26	397	221	23
2.580	89	88	24	77	41	14	27	344	200	35
2.620	87	75	19	88	46	10	20	297	171	18
2.660	95	69	17	55	39	15	29	256	128	19
2.700	96	50	10	59	30	9	23	230	122	15
2.740	77	48	13	58	39	15	15	201	116	16
2.780	670	567	9	50	21	12	16	154	93	11
2.820	0	0	10	48	22	7	16	165	70	6
2.860	0	0	5	42	24	10	8	124	69	14
2.900	0	0	8	29	15	2	8	115	59	16
2.940	0	0	8	43	17	5	12	105	70	13
2.980	0	0	80	308	157	84	11	96	50	7
3.020	0	0	0	0	0	0	9	72	37	10
3.060	0	0	0	0	0	0	5	68	44	8
3.100	0	0	0	0	0	0	4	59	33	10
3.140	0	0	0	0	0	0	3	40	32	3
3.180	0	0	0	0	0	0	99	464	275	114

********** MASS DISTRIBUTIONS FOR 15 GEV/C PI-N DATA **********

MASS GEV	K+ K-	K- K- K+ K+	K+ P-	K+ P+ K- P-	P+ P-	P- P- P+ P+
1.025	0	0	0	0	0	0
1.075	0	0	0	0	0	0
1.125	0	0	0	0	0	0
1.175	0	0	0	0	0	0
1.225	0	0	0	0	0	0
1.275	5	1	0	0	0	0
1.325	22	6	0	0	0	0
1.375	45	24	0	0	0	0
1.425	61	57	0	0	0	0
1.475	90	71	0	0	0	0
1.525	155	104	0	0	0	0
1.575	183	108	0	0	0	0
1.625	204	142	2	0	0	0
1.675	226	156	11	13	0	0
1.725	221	159	18	75	0	0
1.775	215	182	42	194	0	0
1.825	245	145	39	285	0	0
1.875	207	166	45	353	0	0
1.925	187	133	52	403	0	0
1.975	158	152	59	477	0	0
2.025	154	134	66	444	20	24
2.075	119	97	49	496	76	139
2.125	109	86	57	497	132	296
2.175	98	65	60	411	162	380
2.225	85	58	58	404	148	407
2.275	58	50	50	349	158	387
2.325	45	38	45	317	156	356
2.375	48	38	49	246	123	361
2.425	42	28	42	239	132	294
2.475	33	27	31	174	114	274
2.525	32	27	32	169	117	264
2.575	19	30	24	129	87	236
2.625	32	18	29	120	101	193
2.675	13	14	27	92	77	144
2.725	12	20	23	91	63	146
2.775	9	13	13	79	51	98
2.825	7	6	14	62	57	92
2.875	10	11	15	45	40	70
2.925	5	5	12	54	42	70
2.975	9	3	9	40	32	58
3.025	2	6	7	38	32	48
3.075	4	6	6	27	23	38
3.125	5	4	4	18	19	36
3.175	4	5	5	15	19	35
3.225	5	4	0	8	11	20
3.275	1	1	5	15	7	18
3.325	5	1	2	15	14	15
3.375	3	1	3	11	5	8
3.425	1	2	2	12	3	10
3.475	19	14	8	8	4	4
3.525	0	0	1	5	4	12
3.575	0	0	3	4	7	8
3.625	0	0	3	4	3	9
3.675	0	0	2	2	6	8
3.725	0	0	3	4	3	7
3.775	0	0	0	3	3	1
3.825	0	0	1	3	4	2
3.875	0	0	2	3	3	3
3.925	0	0	2	2	4	4
3.975	0	0	14	41	2	4
4.025	0	0	0	0	2	0
4.075	0	0	0	0	2	1
4.125	0	0	0	0	0	3
4.175	0	0	0	0	0	1
4.225	0	0	0	0	1	3
4.275	0	0	0	0	1	2
4.325	0	0	0	0	3	1
4.375	0	0	0	0	1	1
4.425	0	0	0	0	2	0
4.475	0	0	0	0	17	21

APPENDIX IV: MEASUREMENT RESOLUTION OF Q

The Q value for the decay $D^* \rightarrow \bar{D}^0 + \pi^-$ is given by:

$$Q = \frac{E_\pi E_D - P_\pi P_D \left(1 - \frac{\theta^2}{2}\right) - M_\pi M_D}{M_\pi + M_D} + \frac{E_D M_\pi^{\ 2}\, \delta P_\pi^{\ 2}}{E_\pi 2(M_D + M_\pi)}$$

$$= \qquad Q_o \qquad + \qquad Q_2 \qquad (1)$$

where P_π and θ are given by

$$P_\pi = P_\pi / (C_2 + C_1 (n_1 - n_2)); \quad \theta^2 = (\theta_{\pi x} - \theta_{Dx})^2 + (\theta_{\pi y} - \theta_{Dy})^2 \qquad (2)$$

and $\theta_{\pi x} = C_3 n_1 - C_4 n_2 + C_5$. Differentiating this expression we find

$$(M_\pi + M_D)\ \delta Q = \left(\frac{P_\pi}{E_\pi}\ \delta P_\pi E_D - \delta P_\pi P_D \left(1 - \frac{\theta^2}{2}\right)\right.$$

$$\left. + P_\pi P_D (\theta_x \delta\theta_x + \theta_y \delta\theta_y)\right) + Q_2$$

Using equation (2) we can calculate the errors in P and $\theta_{\pi x}$:

$$\delta P_\pi = (C_1 \delta n_2 - C_1 \delta n_1) \frac{P_\pi^{\ 2}}{P_\perp}; \quad \delta\theta_{\pi x} = \delta n_1 C_3 - \delta n_2 C_4$$

where for δn_1 and δn_2 we will eventually substitute $\frac{1}{\sqrt{12}}$. Now, as described in Chapter IX, $\theta_{\pi y}$ is given by:

$$\theta_{\pi y} = \pm \frac{1}{2} \sqrt{C_6 - \theta_{\pi x}^{\ 2}}$$

There are two errors associated with this quantity. The first comes from the measurement error in $\theta_{\pi x}$. This is given by:

$$\delta\theta'_{y\pi} = - \frac{\theta_{\pi x}\ \delta\theta_{\pi x}}{4\ \theta_{\pi y}}$$

Additionally, there is also the measurement error in $\theta_{\pi y}$ given by

$$\delta\theta''_{y\pi} = \frac{2\theta_{\pi y}}{\sqrt{12}}$$

We collect separately the terms proportional to δn_1 and δn_2

$$\begin{aligned}(M_\pi + M_D)\ \delta Q = {} & \delta n_2 \left(T \frac{P_\pi^{\ 2}}{P_\perp} - P_\pi P_D\ \theta_X\ C_4 + P_\pi P_D \theta_y \frac{\theta_{\pi x}}{\theta_{\pi y}}\ C_4\right) \\ & \delta n_1 \left(-T \frac{P_\pi^{\ 2}}{P_\perp}\ C_2 + P_\pi P_D \theta_x C_3 - P_\pi P_D\ \theta_y \frac{\theta_{\pi x}}{\theta_{\pi y}}\ C_3\right) \\ & + \frac{2P_\pi P_D}{\sqrt{12}}\ \theta_{\pi y}\theta_y + Q_2\end{aligned}$$

where T is equal to $\left\{\frac{P_\pi}{E_\pi}\ E_D - P_D\left(1 - \frac{\theta^2}{2}\right)\right\}$.

The error in Q is given by the sum of these terms added in quadrature:

$$\begin{aligned}(M_\pi + M_D)\ \delta Q = \Bigg[& \frac{1}{12}\ \left\{T \frac{P_\pi^{\ 2}}{P_\perp}\ C_2 - P_\pi P_D \theta_x C_4 + P_\pi P_D \theta_y \frac{\theta_{\pi x}}{4\theta_{\pi y}}\ C_4\right\}^2 \\ & + \frac{1}{12}\ \left\{-T \frac{P_\pi^{\ 2}}{P_\perp}\ C_2 + P_\pi P_D \theta_x C_3 - P_\pi P_D \theta_y \frac{\theta_{\pi x}}{4\theta_{\pi y}}\ C_3\right\}^2 , \\ & + \frac{P_\pi^2 P_D^2 \theta^2_{\ \pi y} \theta^2_{\ y}}{3} + Q_2^{\ 2}\Bigg]^{1/2}\end{aligned}$$

To estimate the size of Q we substitute the following values:

$$\theta_{\pi x} = \theta_{Dx} = 0$$

$$P_{\pi} = .4 \text{ GeV/c}$$

$$P_{D} = 6 \text{ GeV/c}$$

Using these numbers we find:

$$\delta Q \simeq 2\text{MeV}.$$

APPENDIX 5: RECONSTRUCTION EFFICIENCIES

MOMENTUM AND BEAM PARTICLE	ε_1 MONTE CARLO	ε_2 TRACK FINDING	ε_3 K DETECTION	ε_4 BINNING[a]	ε_5 $K\pi$ ABSORBTION
15 GeV/c $\overline{P}$					
M_D=2.3 GeV/c^2	$.9 \times 10^{-3}$	.15	.6	.6	.8
M_D=1.86 GeV/c^2	$.4 \times 10^{-3}$				
12.4 GeV/c $\overline{P}$					
M_D=2.3 GeV/c^2	2.0×10^{-3}	.15	.6	.6	.8
M_D=1.86 GeV/c^2	0.6×10^{-3}				
8.5 GeV/c $\overline{P}$					
M_D=1.86 GeV/c^2	1.0×10^{-3}	.10	.6	.6	.8
D^{*-}	$.25 \times 10^{-3}$	.08			.6 ($K\pi\pi$)
K*(1420)	1.8×10^{-4}	.10			
15 GeV/c π^-					
M_D=2.3 GeV/c^2	1.5×10^{-3}	.2	.6	.6	.8
M_D=1.86 GeV/c^2	$.5 \times 10^{-3}$				
10.5 GeV/c π^-	$.3 \times 10^{-3}$	.13	.6	.6	.6 ($K\pi\pi$)

---

[a] applies only to limits quoted for 5σ effect in 20 MeV.